UNIVERSITY OF CINCINNATI

August 15 , 20 01

I, Don Chandana Abeysinghe **,**

hereby submit this as part of the requirements for the degree of:

Doctor of Philosophy

in:

Physics

It is entitled:

Novel MEMS Pressure and Temperature Sensors

Fabricated on Optical Fibers

Approved by:

Prof. Howard E. Jackson

Prof. Joseph T. Boyd

Prof. Leigh Smith

Prof. Rohana Wijewardhana

Novel MEMS Pressure and Temperature Sensors Fabricated on Optical Fibers

A dissertation submitted to the

Division of Research and Advanced Studies
of the University of Cincinnati

in partial fulfillment of the
requirements for the degree of

DOCTORATE OF PHILOSOPHY (Ph.D.)

in the Department of Physics
of the College of Arts and Sciences

2001

by

Don Chandana Abeysinghe

B.S., Physics, University of Colombo, Sri Lanka, 1991
M.S., Physics, University of Cincinnati, 1996

Committee Chair: Professor Howard E. Jackson

Abstract

This thesis presents the design, fabrication, and testing of novel MEMS pressure and temperature sensors fabricated on optical fiber end faces. A simple micromachining process compatible with MEMS was developed in fabricating sensors directly on optical fibers. The pressure sensor configuration involves anodic bonding of a piece of an extremely thin silicon wafer onto the fiber end face over a cavity etched in the central portion of the fiber end face. Final device diameter is thus the same as that of the optical fiber. The temperature sensor is based on anodically bonding a thin piece of silicon onto the fiber end face.

The pressure sensors were fabricated on 400 μm diameter fibers while temperature sensors were fabricated on both 200 and 400 μm diameter fibers. Pressure measurements were made over the 14 to 80 psi range while temperature measurements were made over the 23 to 300 ^{0}C range. Pressure sensor sensitivities of 0.1 mV/psi and 0.2 mV/psi were obtained. The pressure sensors were designed with cavity diameter d=150 μm, and cavity depth h=0.640 μm. Diaphragm thickness for the two sensors were t=7.1, and t=3.4 μm. Higher sensitivity was achieved by design of a sensor with the thinner diaphragm. A sensor array fabrication effort demonstrated that our micromachining process could be extended to simultaneous processing of an array of fibers. The temperature sensor was fabricated by bonding 3.1 μm thick silicon onto the fiber end face. An oxidant-resistant encapsulation scheme for the temperature sensor was proposed, namely aluminum coated silicon nitride (Al/Si_3N_4). The uncoated side of silicon was bonded to a fiber end face using the anodic bonding method. The measured values of $\kappa_\phi=\lambda_m^{-1}d\lambda_m/dT$ for capped and uncapped sensors were $\kappa_\phi=(7.5\pm0.6)\times10^{-5}/^0$C, and $\kappa_\phi=(7.2\pm0.1)\times10^{-5}/^0$C respectively. The measured κ_ϕ value for the uncapped sensor is equal to that which was

determined using the published material properties for crystalline silicon (κ_ϕ $7.9\times10^{-5}/^{0}C$) within measurement uncertainty.

The micromachining process developed for micromachining fiber end faces along with the bonding of silicon to fiber end faces can be extended to fabrication of other MEMS based micro-optic devices where fiber optic interrogation is advantageous.

Acknowledgments

First of all, I want to thank my co-advisers Professors Joseph T. Boyd, and Howard E. Jackson for their invaluable guidance, and generous support throughout my thesis project. Their formative influence on my way of thinking about research will continue well beyond the completion of this thesis. I am indebted to Dr. Boyd for introducing me to an exciting thesis project in the area of Optical MEMS and supervising me in such a manner that enabled me to progress and learn in a timely manner. I feel fortunate in associating such a kind and good person. This thesis would not exist without Dr. Jackson, who accepted me as a doctoral student, at a very difficult time of my life, and who believed in my declaration of dedication. His professionalism, guidance, energy, humor, thoroughness, dedication and inspiration will always serve to me as an example of the perfect supervisor-cheers Dr. Jackson.

I am so thankful to Professors Rohana Wijewardhana and Leigh Smith for serving in my thesis committee. Dr. Wijewardhana will always be remembered a teacher as well as a person who extended many personal and educational advice on many occasions. Dr. Smith has been so kind in taking time to share his expertise on optics with me numerous occasions.

Dr. Frank Pinski, the head of department of Physics, is registered in my mind as a very special person for helping me at a very important situation in my life. Without his guidance and personal involvement I would not have been able finish my doctoral degree at this point of time.

A special acknowledgement is extended to Dr. Samhita Dasgupta, former senior research scientist at Taitech Inc. for her involvement in my thesis project and for making arrangements for me to do part of my experiments at the Wright-Patterson Air Force Base (WPAFB) in Dayton, Ohio.

Special gratitude is devoted to Prof. Chong Ahn of Electrical and Computer Engineering & Computer Science (ECECS), who once accepted me as a student to the MEMS group at the University of Cincinnati.

There are too many people to mention individually, but some names stand out. I want to extend special thanks to John Marcus, the instrumentation specialist at the department of Physics, and P. Venkatharaman for extending me help at many important occasions, and being such good friends. Many thanks to faculty and staff in the department of Physics especially Dr. Michael Sokoloff, Peg Frantz (former graduate secretary in Physics), Melody Whitlock, Dr. Richard Gass, Donna Deutenberg, Lynne McEneny, Bob Schrott, Mark Ankenbauer, Mark Sabatelli, and David Will. I thank my lab mates, Anish Saran, Robert Jones, Christopher Baker, and Vince Stenger for sharing their time, expertise, and humor with me. A big thank you to William Terry of Taitech Inc. for all the help with sensor characterization and packaging.

The road to my graduate degree has been long and winding, so I would also like to thank all my teachers and friends from the early days.

It would have been simply impossible to start, continue and complete it without the support of my parents who, wholeheartedly, made the resources of the family available to me and to whom this work is dedicated; the knowledge that they will always be there to pick up the pieces is what allowed me to repeatedly risk getting shattered. Words cannot truly express my deepest gratitude and appreciation to my mother, who always gave me her love, blessings, and emotional support all the time. I am forever indebted to my mother and amazed at her generosity. I am also indebted to my sister, Vajira, and brother, Kosala, for emotional support and for looking after my mother back home at my absence.

At last but not least, I express my admiration, and heartfelt gratitude to my wife for coming along with me to the US, and for all the support and love.

Table of Content

List of Figures

2.8 The dependence of $\left|dR_F/d\Phi\right|_{MAX}$, Fabry-Perot interferometer s maximum phase sensitivity, on R, the reflectivity

2.9 The three-film sensor structure. The materials 0 through 3 are the SiO_2 optical fiber, the silicon, the Si_3N_4, and the aluminum films, respectively

2.10 Calculated $R_{123}(\lambda)$using these refractive index values, for L_2=0, 106, and 318 nm

3.1 Fabrication steps in order (left to right), cleaved/polished fiber, photoresist coated fiber, blue light coupled fiber, patterned fiber, cavity on fiber, silicon bonded fiber, pressure sensor on fiber.

3.2 The fiber end faces of the cleaved fibers are not uniformly flat across the fiber end face

3.3 Fiber Polishing on polishing paper

3.4 AFM topography measurements of the cavity bottom. Surface roughness numbers are of the same order as those of the initial end face and are low enough to treat the cavity bottom as optical polished.

3.5 AFM line profile of an 80-_m-diameter cavity. The line profile of a cavity was used in determining the cavity depth; this method was employed in determining the etch rate for borosilicate glass fibers.

3.6 Schematics of two photoresist exposure techniques. Both of these techniques used blue Argon ion laser light (λ = 457.9 nm) for exposing photoresist. The first technique (left) involves coupling of light into the opposite fiber end using a low magnification microscope objective (5X) so that the focused laser beam diameter is comparable to the core diameter. The second technique (right) simply directs laser light onto the photoresist-coated fiber end face using a high magnification objective (50X). In this case, the fiber is positioned away from the beam focal point by an amount that corresponds to the required beam diameter

3.7 Experimental set up for photoresist coated fiber consisted of a red light lamp coupled to the microscope, CCD camera mounted to the microscope, and a TV monitor. The position where the laser beam would be focused was marked (as a + in the middle of the screen) on the TV screen. The fiber was aligned so that its center coincided with this point.

3.8 A picture showing a patterned Corning MM fiber (100/140 _m) where a circular area of PR is removed. The removed area has a diameter of 100 _m equal to that of the core of the fiber.

3.9 A picture of a patterned borosilicate glass fiber the second exposure technique where blue light is simply directed onto the photoresist-coated fiber end face using a high magnification objective (50X). A circular area of PR is removed. The removed area has a diameter of 92 _m.

3.10 Measured etch depths for a patterned fiber end face (borosilicate glass) with a cavity of 100 _m diameter at different etching times. The rate was calculated to be 120 nm/min. The etching solution was NH_4F: HF≡12:1.

3.11 A 10-_m single crystal silicon membrane manufactured at the Virginia Semiconductors Inc. The picture exhibits the flexibility of these ultra-thin silicon (membranes) wafers.

3.12 The set-up for anodic bonding. Charges are transported to the electrodes as a dc-field is applied. The cathode is contacted to the glass wafer. The metallic wafer at the bonding interface serves as the anode.

3.13 The experimental set up for bonding of silicon to fiber.

3.14 Ultra-thin silicon anodically bonded to a fiber end face. (a) thin silicon is undesirably bonded to the bottom of the cavity from the voltage shock method, while (b) silicon is not bonded to the bottom as a result from the temperature ramp method . Both cases are for

400 _m diameter fibers, 7 _m thick silicon, and at anodic bonding conditions of temperature 400 ^{0}C and voltage 1000V.

3.14 Ultra-thin silicon anodically bonded to a fiber end face. (a) thin silicon is undesirably bonded to the bottom of the cavity from the voltage shock method, while (b) silicon is not bonded to the bottom as a result from the temperature ramp method . Both cases are for 400 _m diameter fibers, 7 _m thick silicon, and at anodic bonding conditions of temperature 400 ^{0}C and voltage 1000V.

3.15 Anodic bonding set-up of multi-layered silicon onto the fiber end face (not to scale). Bonding was carried out at a temperature of 400 ^{0}C and at a voltage of 1000 V. The voltage was applied between the metal-coated fiber and the uncoated side of silicon

3.16 Thickness and refractive index measurements of silicon nitride on silicon using spectral ellipsometer

4.1 The ambiguity problem: If sensor output is at *A* and falls, has the measurand increased or decreased? Existence of zero problem: If the measurand could lie between 200 and 600, and at turn-on the sensor output is 0.4, what is the measurand? Link independence problem: If the DC signal from the output fiber is 0.4 and the measurand lies between 0.3 and 0.5 but the fiber transmissivity could have changed since calibration, what is the measurand?

4.2 F-P pressure sensor head

4.3 Typical implementation of F-P type sensor.

4.4 Pressure sensor employing a F-P head and a spectrometer to determine cavity separation. [8].

4.5 Packaged pressure sensor.

4.6 Packaged pressure sensor array.

4.7 Pressure sensor measurement system.

4.8 Plot of sensor output in volts versus pressure in psi. Each pressure point is an average of 100 readings. The best fit to the data gives a sensitivity of about 0.11 mV/psi with ± 0.01 mV/psi departure from linearity.

4.9 Calculated sensor responses with respect to pressure for two cases of diaphragm thicknesses t=3.4 μm, and t=7.1 μm. The cavity depth h=0.640 μm and cavity diameter a= 180 μm for both cases.

4.10 Plot of sensor output in volts versus pressure in psi for two sensors with thicknesses t=3.4 μm, and t=7.1 μm. Each pressure point is an average of 100 readings. The best fit to the data is also shown.

4.11 The response of individual pressure sensors in the array

4.12 The response of individual pressure sensors in the array

4.13 Measurement system for the temperature sensor

4.14 Experimental $R_S(\lambda)$ for a thin-film temperature sensor whose silicon thickness is 3.1 μm. Increasing pixel number corresponds to decreasing wavelength.

4.15 Calculated $R_S(\lambda)$ spectrum in the vicinity of 850 nm for a lossless silicon Fabry-Perot whose thickness is 3.1 μm.

4.16 Experimental $R_S(\lambda)$ obtained at different temperatures, the shift in minima at λ_m=832 nm was recorded.

4.17 Measured λ_m versus temperature data for the encapsulated temperature sensor fitted to a linear function.

4.18 Measured λ_m versus temperature data for the encapsulated temperature sensor more accurately fits to a quadratic function than a linear function.

List of Tables

1 Introduction

The technology and applications of optical fibers have progressed very rapidly in recent years. Optical fibers have been an interest in recent research and development, especially as an interrogating component of Microelectromechanical Systems (MEMS) based devices and structures. Optically interrogated pressure sensors have been demonstrated in various configurations using MEMS technology [1-6]. This technology is effective for pressure sensing because the small and precise size of sensing elements results in considerable flexibility in choosing pressure response ranges, bandwidth, and sensitivity. The use of MEMS technology is also advantageous because of the potential for economical manufacturing. Optical interrogation of these sensing elements presents an opportunity to extend use of these sensors to harsh environments in which electronics cannot operate. More specifically, optical interrogation is advantageous since it is superior to electrical interrogation in harsh environments (high temperature, vibration, EM interference, dust, etc.).

This thesis research primarily concentrates on MEMS-technology based pressure and temperature sensors fabricated on optical fibers. Therefore, emphasis is given to a review of MEMS-technology based sensors. A review of fiber optic pressure and temperature sensors is presented through some carefully selected examples.

Traditional sensor configurations consist of a michromachined MEMS sensor structure and an appropriately aligned and fixed optical fiber for optical interrogation (Figure 1(a)). Packaging of these sensors usually involves using adhesives that may limit the temperature of operation of the sensors.

In this thesis we present a novel MEMS pressure sensor fabricated directly on an optical fiber end face. This configuration eliminates the need for adhesives in packaging and as a result,

the maximum temperature of operation of the sensor will be approximately that of the optical fiber. A unique feature of this proposed sensor is that processing is done on a commercial optical fiber as opposed to a wafer. The sensor configuration involves anodic bonding [7] of a piece of an extremely thin silicon wafer onto the fiber end face over a cavity etched in the central portion of the fiber end face (Figure 1(b)). Final device diameter is thus the same as that of the optical fiber.

We expect that sensors such as the one described in this thesis will have significant impact in the advancement of the state-of-the-art in pressure measurement and sensor fabrication techniques beyond that currently available. Due to their small size and the optical interrogation method, multiplexed arrays of such sensors could readily be developed that would provide pressure maps with high spatial resolution. Such arrays could play an important role in future space-based systems and in commercial applications such as automobile and medical applications.

The thesis organization that follows the above reviews succinctly discusses the core work of this thesis. Three main topics that will be included in this section are novel micromachined pressure sensor fabricated on an optical fiber, linear pressure sensor array, and thin-film Fabry-Perot temperature sensor. In each case, the expected specifications/results of the above sensors, and the approach for realizing them will be discussed.

1.1 Fiber Optic Sensors

Modern optical fiber sensors owe their development to two of the most important scientific advances made in the 1960s the laser in 1960 and the modern low-loss optical fiber in 1966. Both equally had origins in work in the previous decades to the microwave predecessor of the laser, the maser, and the short-length low transparency fibers used in early endoscopes for medical and industrial applications. Thus, the early 1970s saw some of the first experiments on low-loss optical fibers being used, not for telecommunications as had been the prime motivation for their development but for sensor purposes. This pioneering work quickly led to the growth of a number of research groups, which had a strong focus on the exploitation of this new technology in sensing and measurement. The field has continued to progress and has developed considerably, since that time.

Optical fibers can be more than mere signal carriers. Light that is launched into and confined to the fiber core propagates along the length of the fiber unperturbed unless acted upon by an external influence. Any disturbance of the fiber alters the characteristics of the guided light; such alterations can be monitored, and related to the magnitude of the disturbing influence. The characteristics of the light that may be monitored in sensing applications include:

(1) Amplitude

(2) Polarization

(3) Phase

(4) Modal distribution

(5) Wavelength

(6) Time-of-flight

The usefulness of the fiber optic sensor depends upon the magnitude of this change and our ability to measure and quantify the same reliably and accurately.

Photonic sensors, signal processors and communication technologies have emerged as viable alternatives to electronics. In telemetry and remote sensing applications it is possible to use a segment of the fiber as a sensor gauge while a long length of the same or another fiber can convey the sensed information to a remote station. Deployment of distributed and array sensors covering extensive structures and geographical locations are also feasible. Many signal-processing devices (splitter, combiner, multiplexer, filter, delay line etc.) can also be made of fiber elements thus enabling the realization of an all-fiber measuring system. Fiber optic sensors and systems have proven their advantages and capabilities in various applications and environments; they can be listed as follows:

(1) They are made from a very durable material (i.e. silica) that is corrosion resistant and can withstand high tensile loading (can withstand up to 5% elongation)

(2) They can measure temperature from —200 ¡C to 800 ¡C for silica, 2000 ¡C for sapphire fibers, with better than 0.1¡C resolution [8].

(3) They are capable of having an extremely wide dynamic range (DC to MHz), with a uniform response characteristic.

(4) They can be applied to complex surfaces and difficult to reach areas (i.e. around the circumference of a round object, around sharp corners or across welds).

(5) Point or distributed sensing lengths are possible (<1 mm to kms);

(6) They offer immunity to electromagnetic interference (EMI) (can operate in electrically noisy environments and have no EMI noise pick-up over very long leads) and are intrinsically safe (suitable for use in hazardous areas because there is no electrical spark potential).

(7) Electrical isolation (they are non-conductive).

(8) They provide high spatial resolution (i.e., 0.1 mm easily achieved).

(9) They are higher sensitivity sensors (they generally utilize the phase change of laser light instead of the intensity change).

(10) Multi-point and multi-parameter monitoring, thus reducing system cost and complexity.

(11) Mechanically rugged.

The major disadvantages associated with using fiber optic sensors are:

(1) May need to isolate sensor from unwanted parameters.

(2) Availability of optical sources.

(3) Cost and availability of suitable instrumentation.

(4) Long term stability needs to be examined.

(5) Low general awareness of fiber optic sensor technology.

Comparing the advantages and disadvantages, it is clear that the advantages far outweigh the disadvantages. Many of the disadvantages can usually also be overcome depending on the specific application.

The simplest sub-division of optical sensors is into so-called *intrinsic* devices, where the interaction occurs actually within an element of the optical fiber itself and *extrinsic* devices were the optical fiber is used to couple light, usually to and from the region where the light beam is influenced by the measurand. This is external to the fiber, but may be attached to it in some suitable way, by fusion-splicing, gluing or mechanical connection, which may often be decoupled.

The familiar requirement of a sensor system is the measurement of a particular measurand at a particular location, this usually being achieved with a *point* sensor. This is the way in which most sensors operate, such as those used, for example, in the monitoring of temperature, acceleration, pressure or many chemical parameters. A schematic of the three major sensor

schemes-point, distributed and quasi-distributed is illustrated in Figure 2. Fig. 2(a) shows, for example, a *point* sensor. Many different types of such sensors exist; as examples, they range from liquid level monitors with a prism tip, through chemically-sensitive dip-in probes for species monitoring and to resonant structures mounted at the end of the fiber for pressure or acceleration measurement. Alternatively, sensor devices may be designed so that they can discriminate in the spatial mode, and in this way, the measurand can be determined along the *length* of the fiber itself, in a process normally termed *distributed* sensing, illustrated in Fig.2 (b). This principle has been employed widely in the measurement of temperature using non-linear effects in fibers, such as Brillouin or Raman scattering or in some types of strain sensing. A style of sensor that is somewhat in between these two types of sensors is termed *quasi-distribute*d, as shown schematically in Fig. 2 (c), where the measurand information is obtained at particular and predetermined points along the length of a fiber network. Here, the fiber has been sensitized or special materials have been introduced into the fiber loop to allow the measurement to be taken and this technique has been applied to temperature and chemical sensing, e.g., using different fiber types. Over the years of fiber sensor development, the issue of how successful the technology has been is frequently raised. The real successes of optical fiber sensor technology have been in such areas as hydrophone underwater acoustic sensing, temperature, pressure, and strain monitoring, and the fiber optic gyroscope (FOG) and some limited achievements have occurred in the chemical bio-medical sensor market. The limitations have usually, but not exclusively, been those of cost rather than technology, and significant strides forward in conventional sensing have occurred in parallel with the developments in fiber optics, emphasizing the best use of the latter in niche areas, usually at low volumes of sensor production. Firms, some of which have come and gone, but names such as Luxtron, Asea, York

Sensors, Photonetics, Metricor, Acuifiber and Babcock, have produced commercial devices and Wilcox will have been familiar to fiber optic sensor users over the years. Patent activity has expanded during that period and this has been surveyed in some detail by Zhang and Grattan [9], giving an indication of developments in new technologies and systems, which are parallel to those of the more familiar learned journal, and conference reports. A number of useful reviews of the subject have been produced over the years, such as that by Kersey [10]. Since 1983, the International Optical Fiber Sensors Conference OFS series has been a good indicator of trends and developments; material from the first 12 of these meetings, covering the period almost to the end of the twentieth century, has now been collected on CD-ROM for ease of search and cross-reference [11] for those interested to chart progress.

The breadth of developments in optical fiber sensor technology has been reflected in a number of textbooks and many review papers e.g., Refs. [10,12,13], so only a small sample of what is an enormous range of activity can be given in a review of this type. The focus is, however, on key developments in the area of optical fiber techniques concentrating in particular upon physical measurands, taking illustrations from important examples of developments. Important types such as interferometric sensors, distributed fiber sensors, grating-based systems both Bragg and long period, luminescent fiber sensors, plastic fiber sensors and, together with their industrial applications, will be representative of many of the major sensor types involved and the trends in the subject. Sensors themselves can be classified in a range of ways, and a fuller classification scheme for all optical fiber sensors have been given by Ning and Grattan [14]. This aspect is not expanded upon in this chapter but the essentials of that classification are used. This relies upon the fact that optical fiber sensors have in common the fact they contain *optical fiber*, one or more of a range of optical *sources* and a *modulation scheme* by which the

measurand introduces a change in the optical signal which can be sensed at the detector and through the signal processing scheme employed. The sensor systems discussed below will be seen to conform to this pattern, providing a useful means of systems analysis and identification.

Fabry-Perot cavity-based sensors, the sensor type we have considered in this thesis, have been widely used for their versatility. This kind of sensor detects changes in optical path length induced by either a change in the refractive index or a change in physical length of the cavity. Micromachining techniques make Fabry-Perot sensors more attractive by reducing the size and the cost of the sensing element. Another advantage of the miniature Fabry-Perot sensor is that low coherence light sources, such as light emitting diodes (LEDs), can be used to generate the interferometric signal, since the optical length of the miniature cavity is of the same order as the wavelength of the light, and shorter than the coherence length of a typical LED.

1.2 Microelectromechanical Systems (MEMS) Technology

MEM sensors based on piezoelectric materials, organic polymers and silicon have undergone tremendous development as smart sensors [14]. Fiber optics based sensors are also emerging as a viable and competitive technology. While many types of stand alone sensors are available, only some of them can be considered for integration with smart structures. Among these, fiber optic sensors are in the forefront in their choice for incorporation into materials and structures made of carbon and glass fiber reinforced polymer composites.

In this study we have incorporated MEMS processing techniques such as photolithography, wet-etching, and silicon-to-glass bonding for micromachining optical fiber end faces. Three novel components of this work include photolithographic patterning of optical fiber end faces, creating a microstructure such as a circular cavity on the fiber end face, and bonding silicon onto

fiber end faces. In other words, we have done micromachining on an optical fiber as opposed to a wafer, as is the case typically.

The advantages of using the silicon micromachining technology can be summarized as follows:

¥ In addition to its well-known excellent electrical properties, silicon has very good mechanical properties. Silicon is stronger than steel (a yield strength of 7 GPa compared to 4.2 GPa) but as light as aluminum (a density of about 2.3 g/cm^3).

¥ Many of the fabrication techniques and materials can be taken from the well-established IC-industry with more than 30 years of experience.

¥ Silicon processing is based on deposition of very thin (sub micrometer) films, which is desirable for miniaturization. Moreover, definition and reproduction of the device shapes are achieved using photolithography techniques, which fundamentally have very high precision.

¥ Batch fabrication means that many devices can be made in parallel and that the price per device can be very low.

¥ The possibility of integration of electronics on the sensor chip as well as creation of multiple sensors on a single chip is a great advantage.

One of the objectives of incorporating MEMS technology into this work is to make use of the above advantages coupled to the advantages of optical fibers to result in robust, cost effective, and miniaturized sensors.

1.3 Review of Micromachined Fiber Optic Pressure Sensors

This section reviews the work on micromachined fiber optic pressure sensors. A few selected examples are presented. Most of the fiber optic sensors are actually so called because

an optical fiber is used for interrogating the sensor, which is a separate entity. In contrast, sensor fabricated on an optical fiber, the main topic of this thesis, is one that contains the sensor within the fiber. As a result, labor intensive fiber alignment and packaging is not required. The selected examples have different sensor configurations and are fabricated using micro fabrication technology. Most of them are based on a Fabry-Perot interferometer; therefore, we restrict this section to Fabry-Perot based michromachined fiber optic pressure sensors.

The Fabry-Perot optical pressure sensor has recently been introduced as an alternative to conventional piezoresistive and capacitive pressure sensors to eliminate signal degradation in harsh environments. In addition piezoresistive pressure sensors show non-linear sensitivity at elevated temperature, and capacitive pressure sensors produce fairly small output capacitance. While a micromachined Fabry-Perot pressure sensor enjoys advantages over counterparts, its commercialization is still in early stage of maturity.

Among the very few reported sensor configurations that fall under the category of Fabry-Perot based michromachined fiber optic pressure sensors, Jie Zhou and others from the University of Cincinnati have developed a simple sensor configuration (Figure 3) with fiber optic interrogation [1] for use in harsh environment applications. They have patterned a circular cavity and etched on a double side polished glass wafer to a predetermined depth and bonded a silicon wafer onto the glass over the cavity. The diaphragm was obtained by etching the unbonded side of silicon while the other side of the silicon/glass assembly is protected. The sensor configuration with reported dimensions is shown in Figure 3. The sensor was designed to operate over the pressure range 0-30 psi at λ=850 nm. Sensor sensitivity to static pressure was reported to be 1.77 mV/psi (Figure 4). Its dynamic pressure tests have shown flat response up to 30 kHz (in the frequency domain) showing adequate unsteady pressure measurement capability

for high-speed propulsion applications. This sensor, though, has the disadvantage that it requires adhesives for fixing and alignment of fiber onto the sensor, thus limiting the high temperature operation.

Optical metrology is promising, but not extensively commercialized for sensor applications. Fabry-Perot based sensors have been broadly studied due to their capabilities for signal "amplification" (i.e., resonance) and tunability [16,17]. Fabry-Perot based devices such as pressure sensors and tunable filters have been built conventionally by using a hybrid two-wafer assembly technique that requires a fusion bonding process [18-20]. The fusion bonding process can limit the flexibility and the accuracy of the device structure dimensions, and restricts the compatibility with conventional VLSI fabrication technology. The surface micromachining method has recently emerged as a way to overcome the drawbacks of the hybrid assembly technique [21,22]. J. Han and Dean P. Neikirk have fabricated a surface micromachined Fabry-Perot pressure transducer [23]. Their approach allows better device performance compared to hybrid fusion bonding through precise control of the cavity gap spacing, and higher manufacturing yield by enhancing the simplicity of fabrication and the compactness of the device [24]. Because they have addressed number of issues common to Fabry-Perot micromchined pressure sensors, we give a detail account of Han and Neikirk work.

Figure 5 and Figure 6 (left) schematically illustrate the configuration and fabrication procedure for a planar bottom diaphragm pressure sensor [25] respectively. The 0.7 um-thick air gap was created on silicon substrate when the sacrificial polysilicon embedded between two diaphragms is removed.

Each diaphragm consists of a multiple film stack of two silicon nitride layers cladding a silicon dioxide layer. These dielectric films were deposited using low-pressure chemical vapor

deposition (LPCVD). The thickness of each layer was chosen in such a way that the Fabry-Perot micro cavity was mechanically stable, i.e., it should not buckle or crack, and must have optimal characteristics of the optical response. One drawback of the planar bottom diaphragm pressure sensor was degradation of output signal intensity as a function of pressure caused by variation in the amount of deflection over the optically sampled area. Under the configuration of a Fabry-Perot pressure sensor with a deflecting bottom diaphragm, there are no means to reduce the parasitic output signal degradation effect because the entire area of the bottom diaphragm is within the optically sampled area. This limitation of a Fabry-Perot pressure sensor with a deflecting bottom diaphragm deteriorates device performance and impedes further improvement.

The Fabry-Perot pressure sensor having a top diaphragm as the deflecting diaphragm reduces the limitations mentioned above. Figure 6 (right) illustrates the fabrication process flow of a planar top diaphragm pressure sensor. The first step of fabrication is to deposit the sacrificial dielectric layers: a 300 thick silicon nitride and 5000 thick silicon dioxide stack. These are deposited using LPCVD. The 5000 silicon dioxide is the main sacrificial layer. The thin 300 silicon nitride is the barrier layer to protect the main sacrificial layer from over etching damage of the KOH wet anisotropic silicon substrate etching step.

The bottom diaphragm dielectric stack is then deposited directly on top of the sacrificial dielectric layers. The bottom diaphragm consists of two 750 thick silicon nitride layers cladding a 4500 thick silicon dioxide layer, all deposited using LPCVD. Next, the dielectric layers on the backside of the double-side polished wafer are patterned and plasma etched. Using patterned back side layers as a mask, the silicon substrate is anisotropically etched with 40% KOH solution at 80 ^{0}C to form the square dielectric bottom diaphragm on the front side of the wafer.

The next step is to form etch windows in the bottom diaphragm using plasma etching from the front side of the wafer. A 0.7 μm-thick LPCVD sacrificial polysilicon layer is next deposited to set the gap between the diaphragms of the final Fabry-Perot microcavity. This is followed by over coating the patterned polysilicon with another dielectric stack. This dielectric stack, two 1500 thick silicon nitride layers cladding a 10500 thick silicon dioxide layer, forms the top diaphragm and is freed after etching the polysilicon.

Measured reflected intensity as a function of pressure for a planar top and planar bottom diaphragm Fabry-Perot pressure sensor is shown Figure 7. The improvement in device performance of the deflecting top diaphragm device compared to the bottom deflecting diaphragm device can be explained as follows: for the planar bottom diaphragm device the entire area of the deflecting, edge-clamped bottom diaphragm is included within the optically sampled area, while for the top diaphragm device the optically sampled area is only a small portion of the entire area of the deflecting top diaphragm. By making the ratio of the area of the top diaphragm to the area of the bottom diaphragm as large as possible while having a detectable output optical response, the parasitic signal averaging effect is minimized in the planar top diaphragm pressure sensor. This can make the top diaphragm device more desirable despite its increased process complexity. Another way to enhance the flatness of the deflecting diaphragm is to add a corrugation structure to the planar diaphragm. However, this approach causes static deflection of a diaphragm without applied pressure, called the zero pressure-offset effect

1.4 Micromachined Pressure Sensor Arrays

One of the main objectives of the pressure sensor array fabrication in this study is to demonstrate that the fabrication process for single pressure sensor can be extended to array fabrication as well.

Increasingly, the successful development of advanced aerodynamic devices requires knowledge of unsteady flow phenomenon. Understanding the role of unsteady flow phenomenon on the performance of an airfoil requires spatially- and temporally- resolved measurements of fluid dynamic properties at the surface. Such interactions are especially of interest to the gas turbine engine community in regard to the role of unsteady pressure oscillations in fan blade fatigue. For example, unsteady pressure fluctuations on the surface of a compressor or turbine blade can lead to vibration and eventual failure due to fatigue. Understanding how time-varying loads on the surface couples into the vibrational modes of the blade structure requires time-resolved measurements of the surface pressure distribution for which pressure sensor arrays are required.

Our literature survey on micromachined pressure sensor arrays revealed that there has not been much research done on the development of micromachined fiber optic pressure sensor arrays. M.F. Miller et al. has one of the most comprehensive works in this line for aerodynamic applications [26]. According to them, the Propulsion Instrumentation Working Group (PIWG), which is a consortium of gas turbine engine companies along with NASA and the Air Force, has developed a set of criteria for pressure mapping instrumentation. These requirements seek to address the measurement needs for high-cycle fatigue testing of fan blades. Table 1 lists the sensor requirements established as exit criterion for the year 2001. This set of performance goals will be used as a guiding-line for our sensor arrays.

The focus of Miller and others work has been to develop micromachined optical pressure sensor arrays that meet these criteria. The modeling results have demonstrated the potential for the micromachined optical pressure sensors to meet or exceed all of the design goals presented in Table 1. A schematic of the basic sensor design is shown in Figure 8. It consists of a square

membrane suspended above an evacuated cavity. For devices fabricated in silicon, this structure is formed using a combination of etching and bonding of silicon-on-insulator (SOI) wafers. The polished wafer surfaces corresponding to the underside of the membrane and the bottom of the etched cavity form the reflective surfaces of the Fabry-Perot etalon. The upper surface of the membrane has an anti -reflection coating to reduce the Fresnel losses at this surface and to prevent interferences within the membrane. An applied pressure differential deflects the upper membrane, changing the optical path length of the etalon cavity and modulating its reflectivity. This reflectivity change can be sensed remotely by illuminating the sensor and collecting the reflected beam onto a photodetector. An entire array of sensors can be simultaneously illuminated and imaged using a camera to obtain an instantaneous map of the pressure distribution on a surface.

The basic sensor element consisted of a 1 mm square, 55 m thick pressure sensor membrane constructed from single-crystal silicon. Further, although the sensor schematic shown in Figure 8 has an etalon cavity that is angled, the sensor cavities were formed using deep reactive ion etching (DRIE). This process produces near vertical sidewalls, increasing the aperture of the sensors and decreasing the number of scattering sites.

In static cell tests, a minimum resolvable pressure of –0.15 psi, corresponding to –0.4% of full scale of 2.5 atm, has been achieved. High-quality images of a 4 x 4 array of sensors were also presented (Figure 9). The center-to-center spacing of the sensors is 1.5 mm. These images were acquired in the static cell at pressures ranging from vacuum to over 8 atm. The reflectivity of the each sensor increases with pressure except at the highest pressure where the membrane deflection exceeds $\lambda/4$ (390 nm), making the next order fringe visible. The average reflectivity is found to display a monotonic variation over a wider pressure range. Time response of the

sensor has shown a rise time of 2.6 s, as determined from the 5% and 95% points of the sensor response. This yields an effective sensor bandwidth of 67 kHz, which exceeds the requirements in Table 1. Extension of this work involves the development of large-area arrays.

Some of the sensor parameters in this table can be discussed in relation to our pressure sensor fabricated on an optical fiber. Because of smaller cavity diameter, this sensor is more suitable for larger pressure ranges of 1-6 atm (~14.0-90.0 psi). In order to obtain a spatial resolution of less than 1 mm requires significant miniaturization of individual sensors; the fiber diameters of the fibers used in this work are 200 μm and 400 μm, and as a result, the above spatial requirement can be easily achieved. Temperature range, dynamic range, and dynamic resolution depend on design of the silicon diaphragm. The frequency response of 400 μm diameter fiber sensor was calculated to be 60 MHz; the high resonance is due to small cavity diameter [27].

1.5 Review of Fiber Optic Temperature Sensors

Their compact size, immunity to EMI/RFI, resistance to corrosive environments, high accuracy, and reliability make fiber optic sensors the best choice for temperature measurements. Fiber-optic transducers are the best and most economical way to make measurements in microwave and RF environments. For example, in temperature measurements, thermocouples and RTDs absorbs microwave and RF energy. This may cause misreading and local self-heating or scorching problems. Temperature monitoring in hazardous environments such as high temperature, and high voltage, and high precision temperature measurement (catheter based) in medical applications are among other applications.

Fiber-linked optical temperature sensors can be categorized on the basis of their method of signal generation, as follows:

(a) Optically emissive, thermally powered [28],

(b) Optically emissive, optically powered [29,30],

(c) Intensity modulating (non-emissive) [31,32].

In this study we have looked at a thin-film Fabry-Perot temperature sensor that fall under the category of intensity modulating (non-emissive). Therefore, the foregoing discussion will be on non-emissive Fabry-Perot type temperature sensors only. A fiber-linked Fabry-Perot interferometer can provide a wavelength-encoded temperature measurement from a very compact and rugged sensor. Typically, the Fabry-Perot temperature sensor is a thin platelet of a material that has a temperature-dependent refractive index [31,32].

1.5.1 Intensity Modulating (Non-Emissive) Sensors

A semiconductor material with a temperature-dependent bandgap E_g can provide a temperature-indicating spectral edge. Sufficiently thick samples of many semiconductors have transmissivities which approximate that of an ideal long-wavelength-pass (LWP) filter, where the cut-on wavelength is $\lambda_g=hc/E_g$. Of course λ_g, must lie within the spectral range of the source, so that GaAs is an obvious sensor material for use with an AlGaAs LED.

When designing an intensity-modulating sensor, a greater flexibility is obtained if the sensor is based on a temperature-dependent change in refractive index rather than absorption. In this case, an interferometer is used to convert the refractive index changes to changes in the sensor s transmissivity. This interferometer can be tuned for a particular temperature range simply by adjusting the length of the temperature-sensitive component. In a two-beam

interferometer, a splitter divides the optical input into two beams. These beams then travel distances L_1 and L_2, through media having refractive indices of n_1 and n_2, before they are recombined. The transmissivity of a two-beam interferometer is given by

$$H_S(\lambda, T) = \frac{1}{2} A_1 \left[1 + A_2 \cos\left[\frac{2\pi}{\lambda} \Lambda_{OPD}(T) \right] \right], \qquad (1.1)$$

where A_1 and A_2 are intensities for the ideal case of zero losses and 50:50 beam-splitters, and where Λ_{OPD} is the interferometer s optical path difference, or OPD, which is given by $\Lambda_{OPD} = n_1 L_1 - n_2 L_2$ [37].

In general, n_1, n_2, L_1, and L_2 will vary as functions of temperature. The sensor should be designed so that Λ_{OPD} is a sensitive and repeatable monotonic function of temperature. The range of temperature is limited to a phase change of 2π or $\Lambda_{OPD} = \lambda_0$, where λ_0 is either the wavelength at which the phase is measured or the initial position of the (tracked) minimum.

A larger range can be provided by measuring the free spectral range, $\Delta\lambda_{FSR}$, which is the wavelength change corresponding to a phase change of 2π, i.e. the period of $H_S(\lambda)$. However, for interferometers of large order, i.e. $\Lambda_{OPD} >> \lambda$, this approach requires a very high resolution. For sufficiently large fringe orders, the free spectral range is given by

$$\Delta\lambda_{FSR} = \frac{\lambda^2}{\Lambda_{OPD}}. \qquad (1.2)$$

The wavelength resolution required to measure a given OPD change is therefore given by

$$\delta \left[\Delta\lambda_{FSR} \right] = \frac{\lambda^2}{\Lambda^2_{OPD}} \delta\Lambda_{OPD}. \qquad (1.3)$$

Figure 1.10 shows a temperature sensor, which is based on an integrated-optic Mach-Zehnder interferometer [33]. Single-mode waveguides and two Y-junction splitter-combiners are fabricated in a lithium-niobate substrate by titanium diffusion. This interferometer s OPD is equal to n_{EFF}_L, where _L=L_1-L_2 and the waveguide s effective index is given by $n_{EFF}=c/v_p$, where v_p is the phase velocity of the guided light. Here both arms are exposed to the sensed temperature, which gives

$$\frac{d\Lambda_{OPD}}{dT} = \Delta L\left[\frac{dn_{EFF}}{dT} + n_{EFF}\kappa_L\right], \qquad (1.4)$$

where the thermal expansion coefficient is κ_L=L^{-1}dL/dT. The effective index n_{EFF} lies between the substrate s refractive index and the slightly higher index of the titanium-doped core. By substituting the material properties of lithium niobate into Equation (1.4), the OPD s temperature sensitivity is determined to be (_L)$^{-1}$d_$_{OPD}$/dT~7.5_10^{-5}/^{0}C. For _L=0.06 mm and _=630 nm, a 2,, phase change will be produced by a temperature change of 140 ^{0}C.

The smallest interferometric sensors are the Fabry-Perot type. Figure 1.11 shows a solid Fabry-Perot interferometer, or etalon, which has a thickness of L and refractive index of n_1. The etalon is surrounded by a material of index n_0, where $n_1>n_0$. The surfaces of this ideal interferometer are perfectly flat and parallel, and the materials are lossless, while the incident light is assumed to be collimated. The reflectivity of the etalon s surfaces is $R=(n_1-n_0)^2/(n_1+n_0)^2$. The interferometer is operated reflectively, as this provides for a more compact single-ended probe.

A commercial Fabry-Perot temperature sensor, available from Photonetrics, is fabricated using a ~1 μm thick slice of single-crystal silicon [34]. The fragile piece of silicon is protected by electrostatically bonding it between two thicker pieces of Pyrex glass. The glass-encased silicon etalon is bonded to a glass capillary, inside of which is affixed an optical fiber. No

collimating lens is required since the silicon is quite thin; also its refractive index is very high, 3.7 at 830 nm, which greatly reduces the internal divergence. Figure 1.12 shows the spectrum of the LED source and the sensor s output spectra at 25 and 125 ^{0}C. The reflectance minima shift to longer wavelengths with increasing temperature, primarily due to the refractive index change, which is about 0.01 %/^{0}C. An optical edge filter splits the sensor s output spectrum into its components above and below 840 nm. The ratio of these intensities is used to determine the temperature over the range of —40 to 300^{0}C. The use of adhesives for affixing the optical fiber onto the silicon etalon limits the temperature of operation of this sensor.

There have been many more fiber optic temperature sensors reported than listed above, but all of them have a disadvantage that they undergo a labor-intensive fabrication process. In 1988, Shultheis and co-workers at ASEA described a silicon Fabry-Perot temperature sensor that was fabricated using a batch-compatible process, the silicon film being deposited directly onto the end of the fiber by electron-beam evaporation [35]. The amorphous silicon film was annealed for one hour at 400 ^{0}C and then coated with a protective layer of polymide. This sensor was tested between room temperature and 400 ^{0}C. In 1989, Glenn Beheim described a sensor similar to Shultheis s, but with two encapsulating layers: SiO_2 and FeCrAl alloy. The FeCrAl layer was suppose to protect silicon from oxidation and the SiO_2 layer was supposed to prevent mixing metal with silicon. After this sensor was annealed at 310 ^{0}C, it was subjected to 230 ^{0}C for 300 hrs, which was found to produce an output drift of 11 ^{0}C.

Glenn Beheim later in 1997 [36] designed and fabricated a thin-film Fabry-Perot temperature sensor with sufficient stability for use in aircraft-engine control systems (to provide a lifetime of 5000 engine-operating hours without recalibration). This sensor was shown to be capable of providing a ±2 ^{0}C accuracy over the range of —55 to 275^{0}C, throughout a 5000 hr

operating life. A silicon Fabry-Perot sensor was fabricated less expensively by depositing the silicon directly onto the end of an optical fiber [37]. A ~2 μm-thick silicon film, which is amorphous and was magnetron sputter-deposited, is crystallized using a laser annealing process. Then, two encapsulating layers are deposited, first, a 90 nm-thick layer of Si_3N_4, which is followed by ~1 μm of aluminum.

The thickness of the silicon film for Beheim s sensor was to fall within the range of 0.8 μm to 4.3 μm. Greater sensitivity is obtained at the high end of this range; however, nonuniformity has been found to impose an upper thickness limit of about 2 μm. In our study we use the anodic bonding method to chemically bond ultra-thin crystalline silicon onto fiber end faces; this enables bonding thicker crystalline silicon. As a result, higher sensitivities can be expected. Further, the use of crystalline silicon will improve the stability of the sensor with proper encapsulation.

1.6 Thesis Organization

We describe the fabrication, and testing of a novel optically interrogated, microelectromechanical system (MEMS) pressure sensor in which the entire MEMS structure is fabricated directly on an optical fiber. A new micromachining process for use on a flat fiber end face that includes photolithographic patterning, wet etching of a cavity, and anodic bonding of a silicon diaphragm will be utilized. Two different exposure techniques utilizing Argon-ion laser line of 457.9 nm were used in patterning photoresist. We will employ both 200 and 400 m diameter multimode optical fibers. Circular cavities with different sizes of diameters (90-150 m) were etched to a designed depth of 0.64 m on the fiber end faces. A pressure sensor

fabricated on an optical fiber will be tested to static pressure range 0-80 psi. The sensor response will be compared with theory.

A linear pressure sensor array will consist of six 400- m-diameter fibers mounted on an aluminum fixture in a line over nearly 2cm length with each fiber sensor separated by nearly 0.3 cm. All six sensors were designed to have the following sensor parameters:

Cavity depth = 0.640 _m

Cavity diameter = 180 _m

Silicon diaphragm thickness = 3.4 _m

Fibers mounted linearly on a fixture will then undergo michromachining processes similar to that in the single pressure sensor case. One of the objectives of this effort is to demonstrate that the above process can easily be adapted for multiple fibers. Another objective is to process all 6 fibers in the array for identical sensors and then to test for identical responses. This approach will be useful in determining the accuracy in fabricating a series of identical sensors. The sensor array will also be tested in the pressure range 0-80 psi.

Anodic bonding will be used in bonding 3.1- m-thick (crystalline) silicon onto an optical fiber tip. An encapsulation scheme consisting of aluminum on silicon nitride will be designed for the sensor to prevent oxidation of silicon. Both 200 m and 400 m diameter fibers will be used. The sensor response in the temperature range 25-300 ^{0}C will be observed and compared with theory. The use of thin crystalline silicon is expected to show improved stability, and also increases the potential for use at higher temperatures. Further, a better control over silicon thickness in this method assures accuracy in production of sensors to the designed temperature range.

1.7 Concluding Remarks

This chapter has reviewed a number of most significant developments in optical fiber sensor technology, and has highlighted the micromachined Fabry-Perot type sensors where progress in developing new devices has been seen. The field is currently driven strongly by the need of the many applications areas and this is as it should be sensors for physical quantities such as temperature, strain, pressure, and displacement remain particularly important, as do sensors for chemical and biochemical applications.

Incorporating a viable technology such as MEMS can further enhance the inherent advantages of fiber optic sensors. Miniaturization of sensors (< 1mm) will lead to realization of dense sensor arrays that will change the state-of-the-art of pressure mapping.

To date fiber sensors have not fulfilled their promise for widespread commercialized use due to a combination of technical, and practical limitations. We have been able to highlight here a few design issues relating to micromachined Fabry-Perot sensors such as optically active area versus diaphragm diameter, and use of conventional hybrid two-wafer method on precise control of cavity gap.

1.8 Reference

[1] Jie Zhou, Samhita Dasgupta, Hiroshi Kobayashi, J. Mitch Wolff, Howard E. Jackson, and Joeseph T. Boyd, Optically Interrogated MEMS Pressure Sensors for Propulsion Applications , Optical Engineering, April 2000.

[2] Youngmin Kim and Dean P. Neikirk, Micromachined Fabry-Perot Cavity Pressure Transducer , IEEE Photonics Technology Letters, Vol. 12, pp. 1471-1473, 1995.

[3] Robert A. Pinnock, Optical pressure and Temperature Sensors for Aerospace Applications , Sensor Review, Vol. 18, Issue: 1, pp. 32-38, 1998.

[4] D. Angelidis and P. Parsons, Optical Micromachined Pressure Sensor for Aerospace Applications , Optical Engineering, Vol. 31, pp.1638-1641, 1992.

[5] Michael H. Beggans, Dentcho I. Ivanov, Steven G. Fu, T.G. Jr. Digges, K.R. Farmer, Optical Pressure Sensor Head Fabrication using Ultra-Thin Silicon Wafer Anodic Bonding , Proceedings of SPIE - The International Society for Optical Engineering. Vol. 3680, n II, pp. 773-782, 1999.

[6] Alexis Mendez, Ted F. Morse, Keith A. Ramsey, Micromachined Fabry-Perot Interferometer with Corrugated Silicon Diaphragm for Fiber Optic Sensing Applications , Proceedings of SPIE-The International Society for Optical Engineering, Vol 1793, pp 170-182, 1993.

[7] Y. Kanda, K. Matsuda, C. Murayama, and J. Sugaya, The Mechanism of Field Assisted Silicon-Glass Bonding , Sensors & Actuators, Vol. A21, pp. 939-943, 1990.

[8] Giallorenzi et.al., "Optical Fiber Sensor Technology", IEEE J. Quantum Electronics QE-18, pp 626-665, 1982.

[9] Z.Y. Zhang, K.T.V. Grattan, Survey of US patent activity in optical fiber sensors , European Workshop on Optical Fiber Sensors, SPIE 3483, pp. 218—222, 1998.

[10] A.D. Kersey, A review of recent developments in fiber optic sensor technology , Opt. Fiber Technology ***2,*** pp.291—317, 1996.

[11] OFS CD, Collected papers of the International Conferences on Optical Fiber Sensors, SPIE, Washington, USA, pp.1983—1997, 1999.

[12] E. Udd, Fiber Optic Sensors, Wiley, USA, 1992.

[13] K.T.V. Grattan, B.T. Meggitt, in: Optical Fiber Sensor Technology Vols. 1—5 Kluwer Academic Publishing, London, 1998—2000.

[14] Y.N. Ning, K.T.V. Grattan, in: K.T.V. Grattan, B.T. Meggitt Eds. , Optical Fiber Sensor Technology: Devices and Technology Vol. 2 Chapman & Hall, London, 1998.

[15] Nadim Maluf, An Introduction to Microelectromechanical Systems Engineering, Artech House Mems Library， December 1999.

[16] J. P. Dakin, C. A. Wade, and P. B. Withers, "An Optical Fiber Pressure Sensor," SPIE Fiber Optics ’87: Fifth International Conference on Fiber Optics and Optoelectronics, vol. 734, pp. 194-201, 1987.

[17] J.Farah, "Interferometric Fiber Optic Displacement Sensor," 1995, USA, Patent # 5420688.

[18] B. Halg, "A silicon pressure sensor with a low-cost contactless interferometric optical readout," Sensors and Actuators A, vol. 30, pp. 225-229, 1992.

[19] J. H. Jerman, D. J. Clift, and S. R. Mallinson, "A Miniature Fabry-Perot Interferometer with a Corrugated Silicon Diaphragm Support," Tech. Digest IEEE Solid-State Sensor and Actuator Workshop, pp. 140-144, 1990.

[20] M. A. Chan, S. D. Collins, and R. L. Smith, "A Micromachined Pressure Sensor with Fiber-optic Interferometric Readout," Sensors and Actuator, vol. 43, pp. 196-201, 1994.

[21] P. M. Sarro, A. W. Herwaarden, and W. Vlist, "A Silicon-silicon nitride Membrane Fabrication Process for Smart Thermal Sensors," Sensors and Actuators A, vol. 41-42, pp. 666-671, 1994.

[22] K. Aratani, P. J. French, P. M. Sarro, D. Poenar, R. F. Wolffenbuttel, and S. Middlehoek, "Surface Micromachined Tunable Interferometer Array," Sensors and Actuators, vol. A 43, pp. 17-23, 1994.

[23] J. Han and D. P. Neikirk, "Deflection behavior of Fabry-Perot pressure sensors having planar and corrugated membrane," SPIE's Micromachining and Microfabrication '96 Symposium: Micromachined Devices and Components II, R. Roop and K. Chau, Proc. SPIE 2882, Austin, Texas, USA, 14-15 October, 1996, pp. 79-90.

[24] Y. Kim and D. P. Neikirk, "Design for Manufacture of Micro Fabry-Perot Cavity-based Sensors," Sensors and Actuators A, vol. SNA050/1-2, pp. 141-146, 1995.

[25] Y. Kim and D. P. Neikirk, "Micromachined Fabry-Perot Cavity Pressure Transducer with Optical Fiber Interconnects," Micromached Devices and Components, R. Roop and K. Chau ed., Austin, Texas, USA, 242-249, pp. 23-24 October 1995.

[26] M.F. Miller, M.G. Allen, R.L. Bayt, and K.S. Breuer, Design and Testing of micromachined Fabry-Perot Pressure Sensors for Aerodynamic Applications , 38 th AIAA Aerospace Sciences Meeting & Exhibit, 10-13 January, Reno, Nevada.

[27] Mario Di Giovanni, Flat and Corrugated Diaphragm Design Handbook (Mercel Dekker, NewYork), 1992.

[28] R.R. Dils, High Teperature Fiber Thermometry , J. Appl. Phys. 54, pp. 1198, 1983.

[29] A. Ohte, K. Akiyama, and I. Ohno, Optically-Powered Transducer with Optical-Fiber Data Link , Fiber Optic and Laser Sensors II, E.L. Moore and O.G. Ramer, eds., Proc. SPIE 478, pp. 33-38, 1985.

[30] K.T.M. Gratten, A.W. Palmer, C.A. Wilson, A Miniaturized Microcomputer-based Neodymium Decat-Time Temperature Sensor , J. Phys. E: Sci. Instrum. 20,pp. 1201 1985.

[31]G. Beheim, Fiber-Optic Thermometer Using semiconductor-etalon sensor , Electron. Lett. 22, pp. 238-239, 1985.

[32] J.C. Hartl, E. W. Saaski, and G. L. Mitchell, Fiber Optic Temperature Sensor Using Spectral Modulation , Fiber Optic and Laser Sensors V, R. P. DePaula and E. Udd, eds., Proc. SPIE 838, pp. 257-261, 1987.

[33] L.M. Johnson, F.J. Leonberger, and G.W. Pratt, Jr., Integrated Optical Temperature Sensor , Appl. Phys. Lett . 41, pp.134, 1982.

[34] J.C. Hartl, E.W. Saaski, and G. L. Mitchell, Fiber Optic Temperature Sensor Using Spectral Modulation , Fiber Optic and Laser Sensors V, R.P. DePaula and E. Udd, eds., Proc. SPIE 838, pp. 257-261, 1987.

[35] L. Shultheis, H. Amstutz, and M. Kaufmann, Fiber-Optic Temperature Sensing with Ultra-thin Silicon Etalons , Opt. Lett. 13, pp.782, 1988.

[36] Glenn Beheim, fiberOptic Temperature Sensor Using a Thin-Film Fabry-Perot Interferometer , Ph.D. Thesis & NASA Technical Memorandum 107459, May 1997.

[37] Glenn Beheim, Fiber-Optic Temperature Sensor Using a Thin-film Fabry-Perot Interferometer , Ph.D. thesis, Case Western Reserve University, Cleveland, Ohio, May 1996.

Pressure Range	1 to 6 atm
Temperature Range	<500 ^{0}K
Spatial Resolution	<1 mm
Dynamic Range	25 % of static P
Dynamic Resolution	1 to 2% of static P
Frequency Response	>6 kHz
G-loading limit	62,000 G

Table 1.1 Michromachined Pressure Sensor Array Performance Goals

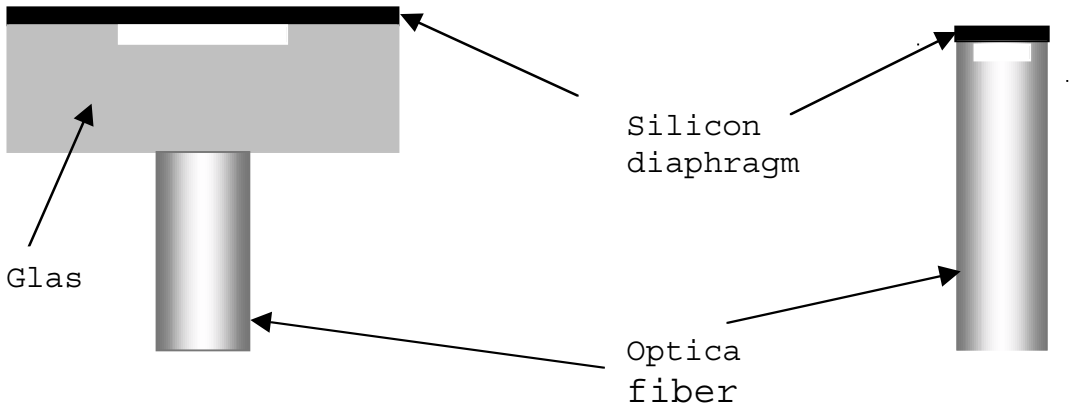

(a) (b)

Figure 1.1 Illustration of two configurations of fiber optically interrogated MEMS pressure sensors. Figure 1(a) shows the usual configuration, which consists of a glass plate with a shallow cylindrical cavity etched into one surface with the cavity covered by a thin silicon diaphragm that has been anodically bonded to the patterned glass wafer [1]. Figure 1(b) shows the configuration where the cavity is formed on the end of the optical fiber and a silicon diaphragm is bonded anodically.

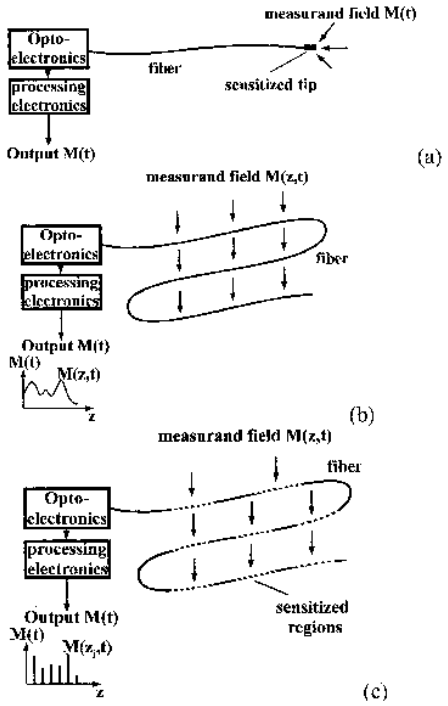

Figure 1.2 (a) Point, (b) intrinsic distributed, and (c) quasi-distributed sensing.

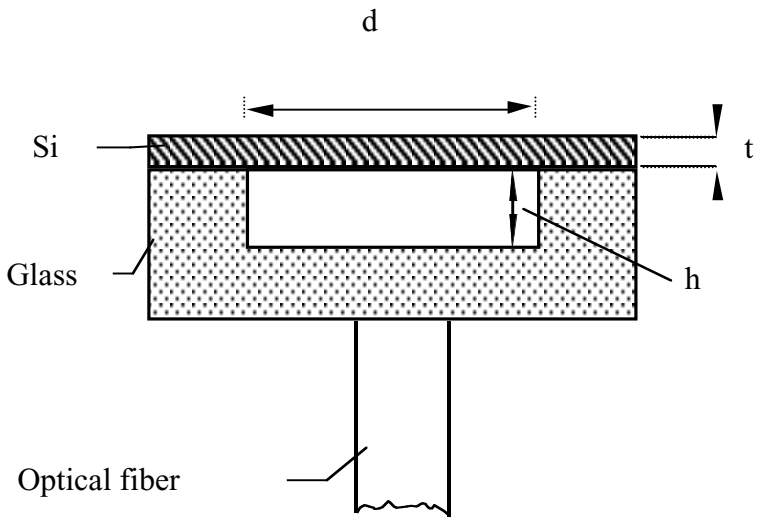

Figure 1.3 Configuration of the optically interrogated MEMS pressure sensor.

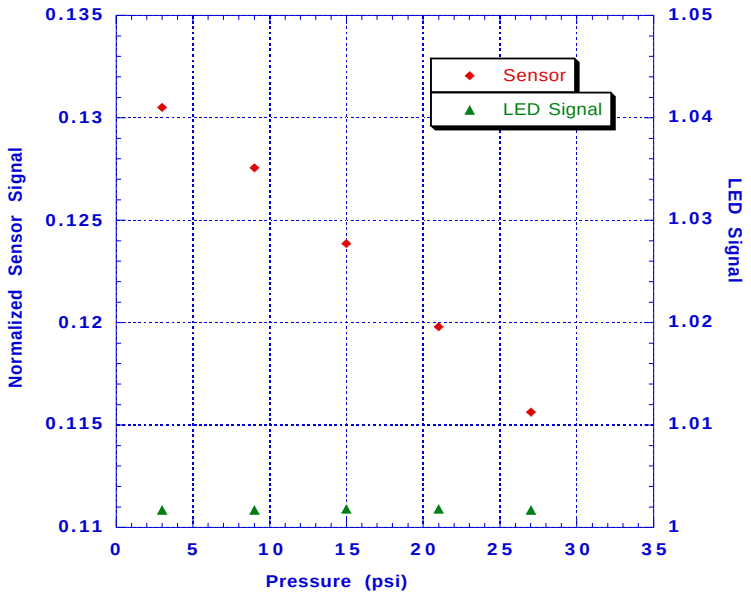

Figure 1.4 (a) Static response of an optically interrogated MEMS pressure sensor in which normalized sensor signal is plotted as a function of pressure.

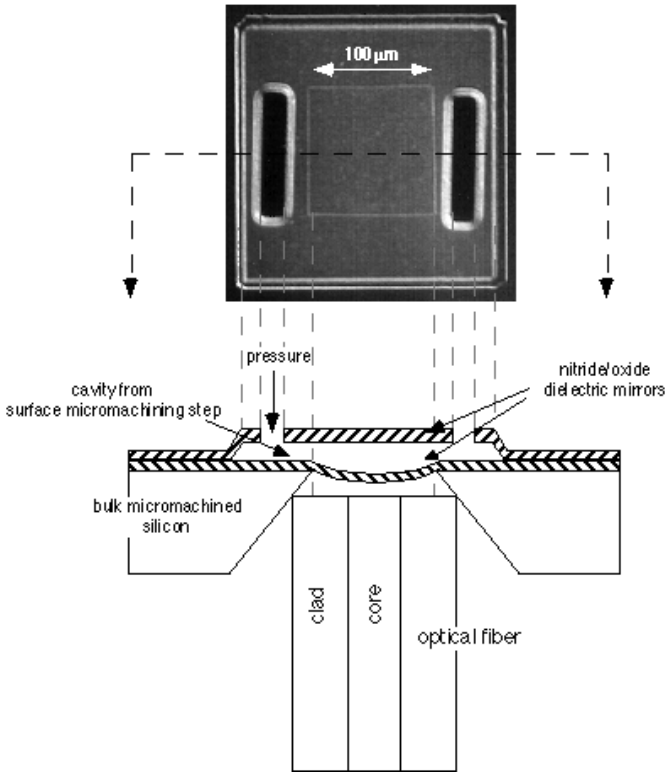

Figure 1.5 Photomicrograph (top view) and cross-sectional diagram of an air-gap Fabry-Perot cavity formed by surface micromachining. The top and bottom mirrors for the cavity are silicon dioxide/silicon nitride dielectric stacks and the sacrificial layer is polysilicon. Optical access is provided by bulk-micromachining through the back of the wafer using standard anisotropic etch procedures. An optical fiber is then inserted into the hole, and the reflected light intensity monitored.

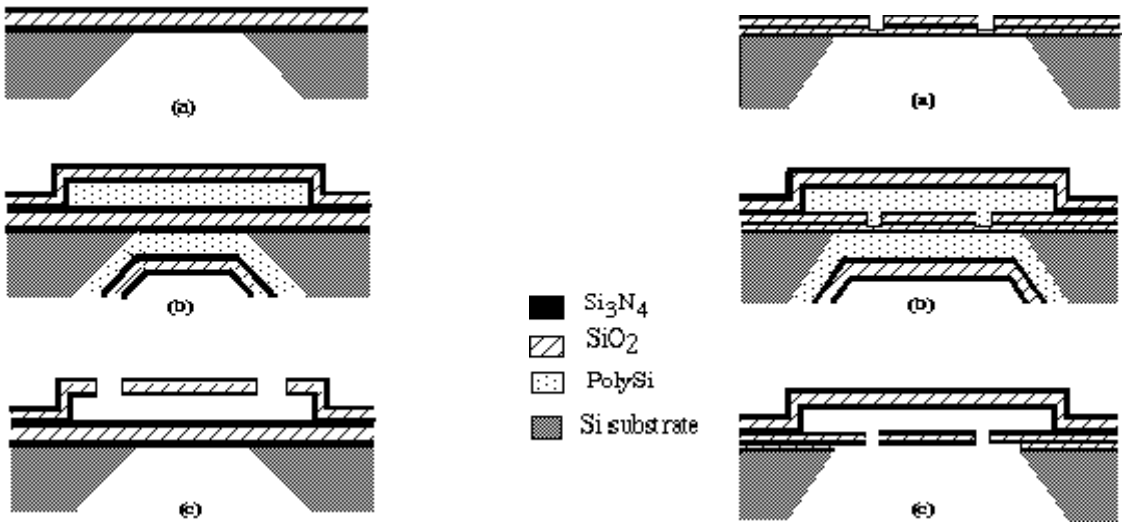

Figure 1.6 (left) Schematic view of fabrication procedure for planar bottom diaphragm pressure sensor; (a) formation of bottom diaphragm; (b) patterning and deposition of polysilicon and top diaphragm; (c) etch window formation and sacrificial polysilicon etching.

Figure 1.6 (right) Schematic view of fabrication procedure for planar top diaphragm pressure sensor; (a) formation of bottom diaphragm and etch windows; (b) patterning and deposition of polysilicon and top diaphragm; (c) blanket backside and sacrificial polysilicon etching.

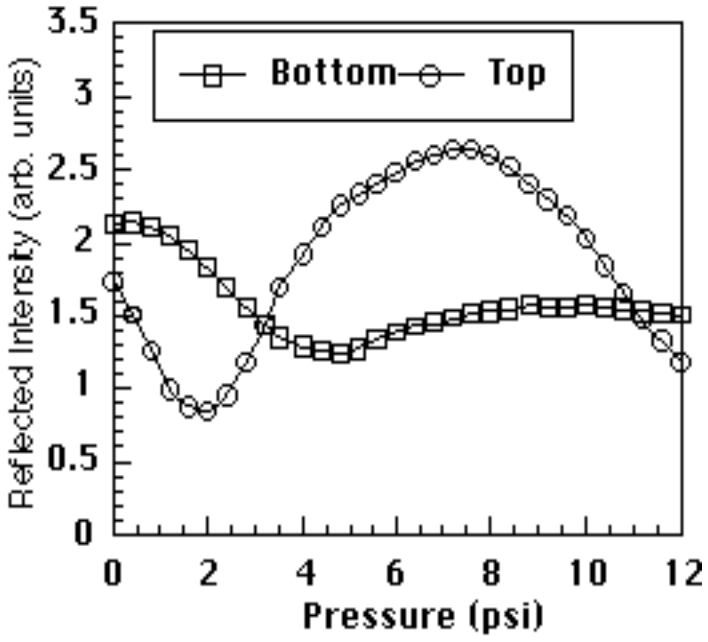
Bottom
Top
Reflected Intensity (arb. units)
Pressure (psi)
0
0.5
1
1.5
2
2.5
3
3.5
0
2
4
6
8
10
12

Figure 1.7 Measured reflected intensity as a function of pressure for a planar top and planar bottom diaphragm Fabry-Perot pressure sensor.

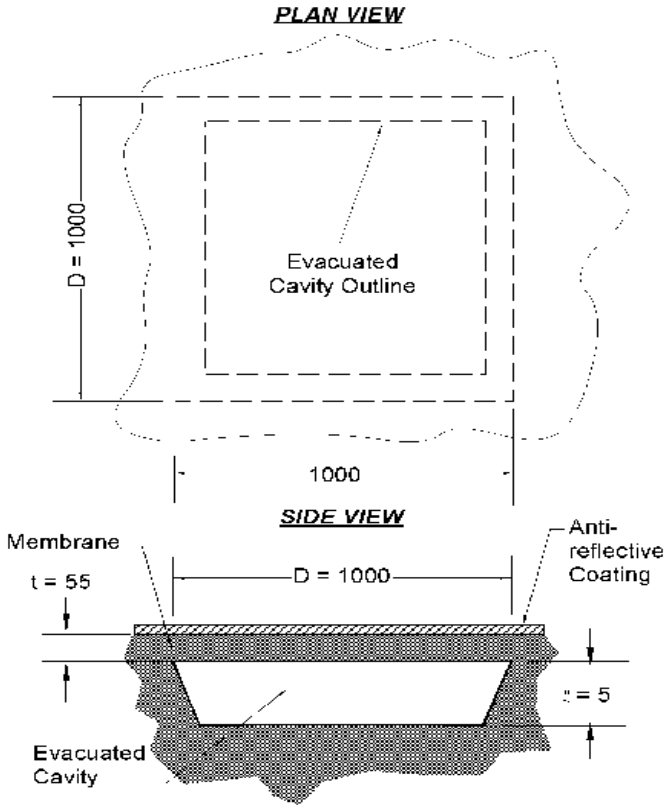

Figure 1.8 Schematic of single element micromachined optical pressure sensor. All dimensions in microns. Vertical scale exaggerated for clarity.

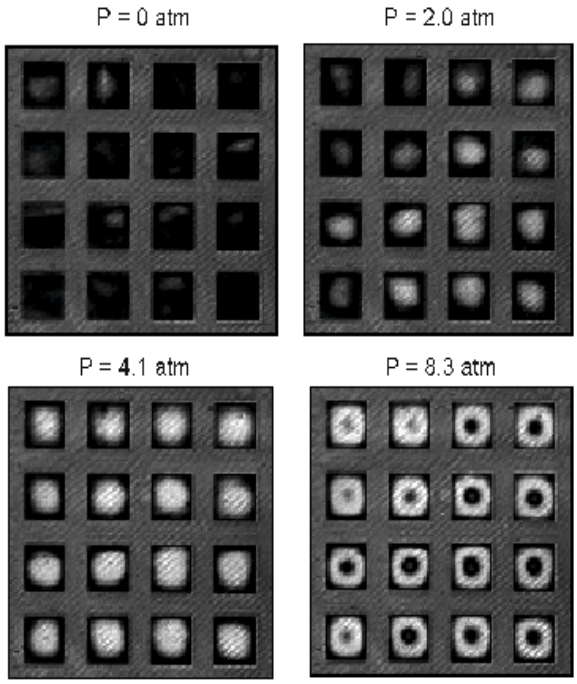

Figure 1.9 Images of a 4 x 4 array of 1 mm pressure sensors.

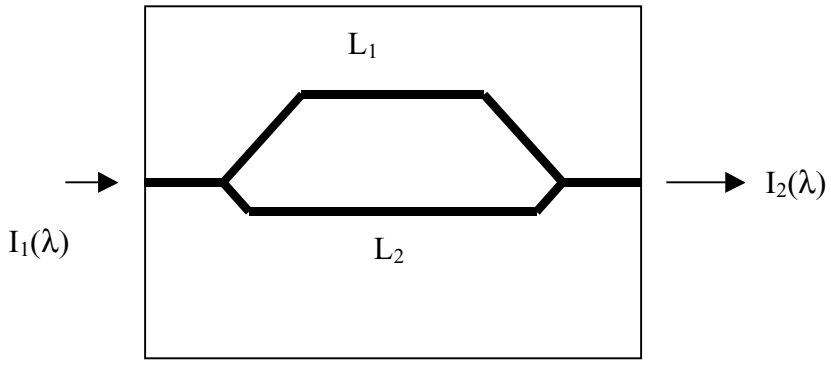

Figure 1.10 Integrated-optic interferometer for temperature measurements.

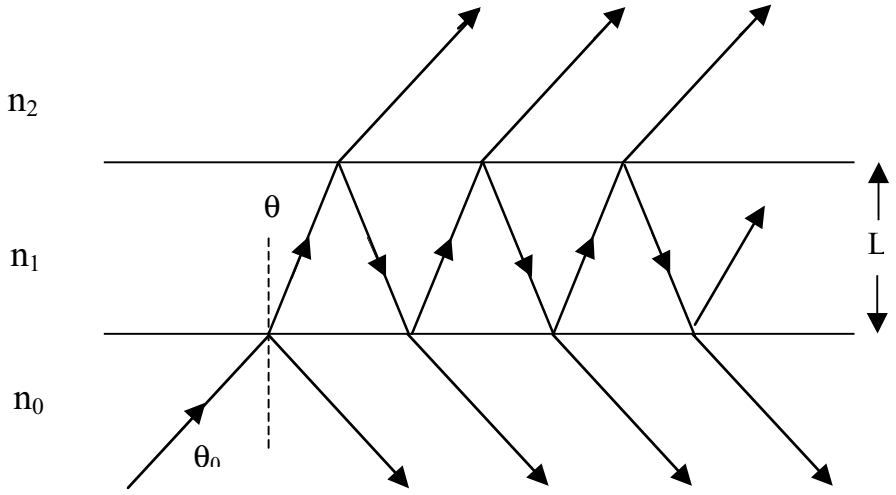
n_2
n_1
n_0
θ
θ_0
L

Figure 1.11 Solid Fabry-Perot interferometer, or etalon, which has a thickness of L and refractive index of n_1. The etalon is surrounded by a material of index n_0, where $n_1 > n_0$.

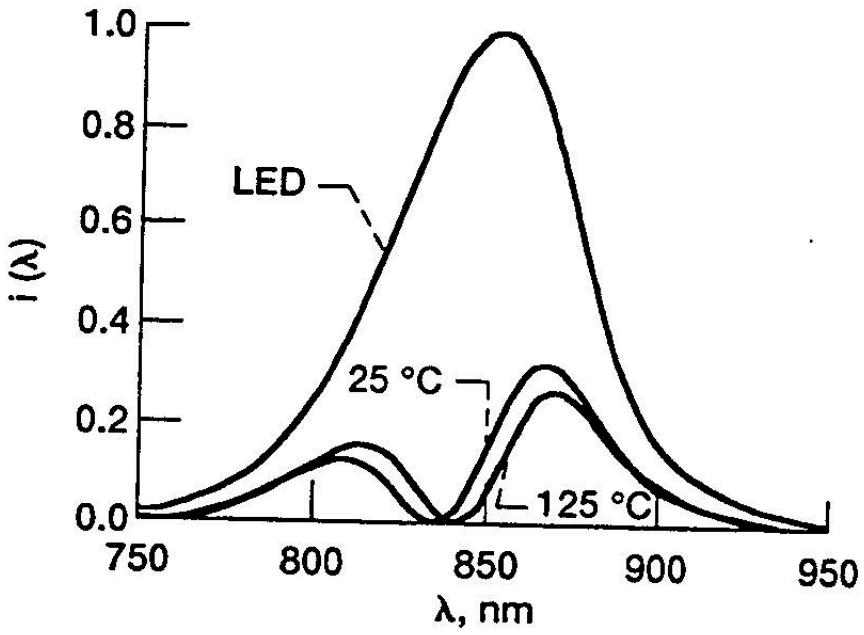

Figure 1.12 The spectrum of the LED source and the sensor s output spectra at 25 and 125 ^{0}C.

2. Design of Sensors

2.1 Introduction

This section will describe the design of Fabry-Perot type sensors. First, ideal Fabry-Perot pressure and temperature sensors will be considered. For the sake of treatment of the encapsulated temperature sensor, the design of multi-layer film Fabry-Perot will also be considered. Design will be used to predict the response of pressure and temperature sensors as a function of different sensor parameters. An idealized model will be used which neglects absorption and assumes equal reflectivites at both surfaces of the film.

2.2. Plane Wave Propagation in Homogeneous Media

Expressed in terms of the electric and magnetic field intensities, $\overline{E}$ and $\overline{H}$, Maxwell s equations [1], for an isotropic medium, which is nonconductive, nonmagnetic, and charge free, are

$$\nabla.[(\varepsilon\varepsilon_0)\overline{E}] = 0, \qquad (2.1)$$

$$\nabla.\overline{H} = 0, \qquad (2.2)$$

$$\nabla \times \overline{E} = -\mu_0 \frac{\partial \overline{H}}{\partial t}, \qquad (2.3)$$

$$\nabla \times \overline{H} = -\varepsilon\varepsilon_0 \frac{\partial \overline{E}}{\partial t}. \qquad (2.4)$$

Here ε_0 and μ_0 are the permittivity and permeability of free space, and ε is the medium s relative permittivity or dielectric constant. In general, ε is complex with real part ε_1 and imaginary part ε_2.

After taking the curl of both sides of equations 2.3 and 2.4, if one assumes that is ε uniform throughout the medium, one obtains the wave equations in $\overline{E}$ and $\overline{H}$,

$$\nabla^2 \overline{E} = \frac{\varepsilon}{c^2} \frac{\partial^2 \overline{E}}{\partial t^2}, \qquad (2.5)$$

$$\nabla^2 \overline{H} = \frac{\varepsilon}{c^2} \frac{\partial^2 \overline{H}}{\partial t^2}. \qquad (2.6)$$

The plane wave solution of these equations is given by

$$\overline{E}(\overline{r}, t) = \overline{E}_0 \exp j(\frac{\omega N}{c} \overline{u}.\overline{r} - \omega t), \qquad (2.7)$$

and

$$\overline{H}(r, t) = \frac{N}{Z_0} \overline{u} \times \overline{E}_0 \exp j(\frac{\omega N}{c} \overline{u}.r - \omega t), \qquad (2.8)$$

where $\overline{u}$ is the normalized propagation vector (i.e. $\overline{u}.\overline{u}$ =1), which must be perpendicular to $\overline{E}_0$ (i.e. $\overline{u}.\overline{E}_0$ =0).

The speed of light in free space c is

$$c = \frac{1}{\sqrt{\varepsilon_0 \mu_0}}, \qquad (2.9)$$

and the impedance of free space Z_0 is

$$Z_0 = \sqrt{\frac{\mu_0}{\varepsilon_0}}. \qquad (2.10)$$

The medium s complex refractive index N is defined to be

$$N = \sqrt{\varepsilon}. \qquad (2.11)$$

In general, N will vary as a function of ω. To emphasize its ω dependence, the relative permittivity ε is commonly designated the dielectric function. The real and imaginary parts of N are designated n and k, i.e. N=n+jk. The refractive index n determines the wave s phase velocity v_p=c/n, and the extinction coefficient k gives the absorption coefficient $\alpha=4\pi k/\lambda$, where the wavelength in free space λ is equal to $2\pi c/\omega$.

From the definition of N,

$$\varepsilon_1 = n^2 - k^2, \qquad (2.12)$$

and

$$\varepsilon_2 = 2nk. \qquad (2.13)$$

The magnitude and direction of the wave s energy flux are given by the time-average Poynting vector,

$$\overline{S}_{av} = \frac{1}{2}\,\mathrm{Re}\,\overline{E} \times \overline{H}^*, \qquad (2.14)$$

and the wave s intensity, I, is simply the magnitude of $\overline{S}_{av}$.

In the case of nonabsorptive medium, where k=0, _ is real and it is perpendicular to the planes of constant phase. For an absorptive medium that is entered at a normal angle of incidence, _ is again real and it is perpendicular to the planes of constant amplitude and constant

phase. If a plane wave enters an absorptive material at other than normal incidence, then _ is complex, and in this case the normals to the planes of constant amplitude and constant phase are not necessarily coincident, as they are parallel to Re(u) and Im(u), respectively.

2.2.1 Reflection and Transmission at an Interface Between Two Materials

Consider a plane wave, incident on a medium of complex refractive index N_1 from a medium of index N_0, at an angle of θ_0 from the normal to the interface, as shown in Figure 2.1. The xy plane is the plane of incidence and the x-axis is perpendicular to the interface so that the incident wave s normalized propagation vector is given by

$$\bar{u}_i = x\cos\theta_0 + y\sin\theta_0 . \qquad (2.15)$$

Satisfaction of Maxwell s equations requires continuity of the tangential components of _ and _ across the interface. The reflected wave, therefore, must have a normalized propagation vector,

$$\bar{u}_r = -x\cos\theta_0 + y\sin\theta_0 . \qquad (2.16)$$

For the transmitted wave,

$$\bar{u}_t = x\cos\theta_1 + y\sin\theta_1, \qquad (2.17)$$

where

$$N_1\sin\theta_1 = N_0\sin\theta_0. \qquad (2.18)$$

This last equation is Snell s law of refraction. If $k_0=0$, then

$$N_1\bar{u}_t = x\sqrt{n_1^2 - k_1^2 - n_0^2\sin^2\theta_0 + j2n_1k_1} + y\sin\theta_0 . \qquad (2.19)$$

Continuity of the tangential _ and _ components also determines the amplitude reflection and transmission coefficients, $r=E_{0r}/E_{0i}$ and $t=E_{0t}/E_{0i}$. The amplitude of the reflected and transmitted waves are most readily determined if the incident wave s electric field vector $\__0$ is decomposed into its components parallel and perpendicular to the plane of incidence. These eigenpolarization states, *p* and *s*, respectively, are maintained after reflection or transmission by the interface. The responses to an arbitrarily polarized input, therefore, can be obtained by superposition of the responses to the input s *p* and *s* components. These are determined using Fresnel s amplitude coefficients [1],

$$r_p = \frac{-N_1 \cos\theta_0 + N_0 \cos\theta_1}{N_1 \cos\theta_0 + N_0 \cos\theta_1}, \tag{2.20}$$

$$r_s = \frac{N_1 \cos\theta_0 - N_0 \cos\theta_1}{N_0 \cos\theta_0 + N_1 \cos\theta_1}, \tag{2.21}$$

$$t_p = \frac{2N_0 \cos\theta_0}{N_1 \cos\theta_0 + N_0 \cos\theta_1}, \tag{2.22}$$

$$t_s = \frac{2N_0 \cos\theta_0}{N_0 \cos\theta_0 + N_1 \cos\theta_1}. \tag{2.23}$$

2.2.2 Reflection from a Single Layer

Consider now the reflection of light from a Fabry-Perot interferometer, which, as shown in Figure 2.2, is comprised of a single film having a thickness L and complex refractive index N_1. If the angle of incidence is θ_0, and the refractive indices of the ambient and substrate are N_0 and N_2, respectively, then the amplitude reflectance of the film is [2]

$$r_F = r_{01} + t_{01}t_{10}r_{12}\exp(j2\Omega) \times \left[1 + r_{10}r_{12}\exp(j2\Omega) + r_{10}^2 r_{12}^2 \exp(j4\Omega) + ...\right] \tag{2.24}$$

where

$$\Omega = \frac{2\pi}{\lambda} N_1 L \cos\theta_1. \qquad (2.25)$$

The angle of incidence inside the film, θ_1, is determined using Fresnel s law (θ_1 may be complex). The variables r_{ij} and t_{ij} are the Fresnel amplitude coefficients, for the appropriate polarization states, for a wave incident from medium *i* into *j*.

Using $r_{01} = -r_{10}$ and $t_{01}t_{10} = 1-r^2_{10}$, which follow from equations 2.20-2.23, gives

$$r_F = \frac{-r_{10} + r_{12}\exp(j2\Omega)}{1 - r_{10}r_{12}\exp(j2\Omega)}. \qquad (2.26)$$

The film s amplitude transmittance may be obtained by similar means, and is given by

$$t_F = \frac{t_{01}t_{12}\exp(j\Omega)}{1 - r_{10}r_{12}\exp(j2\Omega)}. \qquad (2.27)$$

Consider first an ideal Fabry-Perot interferometer, which is both lossless and symmetric, so that all $k=0$ and $n_2=n_0$. If one also assumes that $n_1>n_0$, then the phase change on internal reflection is zero and the reflectivity is given by

$$R_F = \frac{2R - 2R\cos(2\Phi)}{1 + R^2 - 2R\cos(2\Phi)}, \qquad (2.28)$$

where

$$R = \left|r_{10}\right|^2, \qquad (2.29)$$

and

$$\Phi = \frac{2\pi}{\lambda}\Lambda_{OPD}. \qquad (2.30)$$

Here, the interferometer s optical path difference or OPD is given by

$$\Lambda_{OPD} = 2n_1 L\cos\theta_1, \qquad (2.31)$$

The reflectivity can be rewritten as

$$R_F = \frac{FSin^2(\Phi)}{1 + FSin^2(\Phi)}, \tag{2.32}$$

where

$$F = \frac{4R}{(1-R)^2}\ , \tag{2.33}$$

$$\text{with } R = \frac{(n_1 - n_0)^2}{(n_1 + n_0)^2}. \tag{2.34}$$

The transmissivity of the ideal Fabry-Perot interferometer is given by

$$T_F = \frac{1}{1 + FSin^2(\Phi)}, \tag{2.35}$$

As expected, for zero loss, $T_F+R_F=1$. The reflectivity is a minimum, and the transmissivity a maximum, at the resonance condition, $\Phi = \pi m$, where m is an integer. The coefficient F characterizes the resonance width (finesse, $\pi/2\ F^{1/2}$, is a useful concept only for large R). A larger R narrows the reflectance minima, or fringes, as shown by Figure 2.3, where $R_F(\Phi)$ is plotted for different values of R. Figure 2.4 shows the calculated R_F versus λ for a Fabry-Perot with $N_0=1.5$, $N_1=1$, and $N_2=3.46$ for two different values of widths. This plot shows that the spectrum is shifted as the Fabry-Perot width is changed.

2.3 Design of Ideal Fabry-Perot Pressure Sensor

The optical fiber pressure sensor (shown in Figure 1.1) is a Fabry-Perot cavity sensor consisting of two parallel, partially reflecting surfaces separated by a gap. Light is introduced into the Fabry-Perot cavity through the optical fiber. The reflected light following multiple

reflections within the cavity is carried back through the fiber. The amplitude reflectance *r* of the light from Fabry-Perot is given by equation 2.26.

When this equation is applied to a Fabry-Perot pressure sensor, it can be rewritten as

$$r_S = \frac{-r_{01} + r_{12}\exp(j2\Omega)}{1 - r_{10}r_{12}\exp(j2\Omega)}, \tag{2.36}$$

$$\text{where } r_{01} = \frac{(n_A - n_G)}{(n_{Si} + n_G)}, \tag{2.37}$$

$$r_{12} = \frac{(n_A - n_{Si})}{(n_{Si} + n_A)}, \tag{2.38}$$

$$\text{and } \Omega = \frac{2\pi}{\lambda} n_A h\,. \tag{2.39}$$

Refractive indices of glass, air, and silicon are denoted as n_G (=1.57), n_A (=1.0), and n_{Si} (=3.46) respectively and the cavity depth is denoted as *h*. Here, we have assumed normal incidence of light. And the reflectivity of the Fabry-Perot pressure sensor is given by $R_S = |r_S|^2$. This result in a periodic variation of the reflected light intensity as a function of the cavity depth *h* (Figure 2.5). Pressure causes the cavity depth to change and hence the reflected light will change.

The top diaphragm is modeled as a circular membrane [4]. The deflection of the diaphragm due to the application of pressure P is given by

$$w_{(r)} = w_c\left[1 - \frac{r^2}{a^2}\right] = \frac{3Pa^4(1-\gamma^2)}{16Et^3}\left[1 - \frac{r^2}{a^2}\right], \tag{2.40}$$

where r is the distance from the center of the plate; $w_{(r)}$ is the deflection at$r$; $w_{(c)}$ is the deflection at r=0; P is the normal pressure; a is the radius of the diaphragm; γ is the Poisson s ratio for silicon, E is the Young s modulus, and t is the diaphragm thickness.

The maximum cavity depth is designed for a deflection of $\lambda_0 / 4$ where λ_0 is the operating wavelength. Thus, the pressure that causes a deflection of $\lambda_0 / 4$ is given by

$$P = \frac{4Et^3\lambda_0}{3R^4(1-\gamma^2)}. \qquad (2.41)$$

We initially designed pressure sensors to respond over the pressure range 1-80 psi, and to operate at λ_0=850 nm, and chose a=150 μm as a size compatible with the fiber diameter and fabrication. As can be seen from the above equation, the thickness and the diameter of the diaphragm are crucial parameters for sensor design. Calculations indicate that at λ_0=850 nm, the diaphragm thickness required for making a diaphragm-center-deflection of $\lambda_0 / 4$ at 80 psi is 7.1 μm. The depth of the etched cavity in the glass wafer must be greater than $\lambda_0 / 4$, but to avoid ambiguities, must be small enough to yield a cavity where free spectral range (the wavelength range corresponding to a phase change $\Delta\Phi = \pi$, is termed the free spectral range, $\Delta\lambda_{FSR}$) somewhat greater than the LED linewidth of 100 nm. That is, the spectral width of LED imposes an upper bound for the cavity depth. It is assumed here that the source spectrum is a subset of the analyzer s range. For moderately large fringe order m, the free spectral range is $\Delta\lambda_{FSR} \approx \lambda_m^{\,2} / \Lambda_{OPD}$. .

The above requirement can then be written as

$$\Delta\lambda_{LED} \le \lambda_m^{\,2} / \Lambda_{OPD}. \qquad (2.42)$$

A free spectral range of 100 nm corresponds to a cavity depth of ≈ 3.6 μm. We chose a cavity depth of 0.640 μm to lie within these two limiting values. Figure 2.7 shows the calculated reflectivity versus wavelength of a Fabry-Perot pressure sensor for two cavity depths, one that meets the condition given by equation 2.42, and another that exceeds the limit of 3.6 μm. This plot illustrates that when the cavity depth exceeds the limit set by the equation 2.42, an ambiguity is introduced in the measurements.

We designed another pressure sensor to respond over the pressure range 1-60 psi, and to operate at λ_0=850 nm, with a=150 μm. The intention of this second design where we use a thinner silicon diaphragm is to obtain a greater response. The calculated silicon diaphragm thickness is 3.4 μm, i.e. nearly 1/2 of the previous case. Calculated sensor responses with respect to pressure for two cases of diaphragm thickness are shown in Figure 2.6. Substitution of equation 2.40 in equation 2.36 will enable to plot reflectivity with respect to pressure. Reflectivity from the sensor with 3.4 μm-thick diaphragm over the range 1-60 psi is over 3 times that from the sensor with 7.1 μm-thick diaphragm. In the case of a 3.4 μm-thick diaphragm, the reflectivity curve starts to fall at 65 psi leading to ambiguity in the measurements. For this reason this sensor will be tested in the range 1-60 psi as intended in the design.

It is important to investigate if ultra-thin silicon can withstand the strains resulting from the above pressure ranges. Diaphragm theory [4] can be used in predicting the maximum tolerable pressure P_m at maximum tensile stress (σ_m) at the center of diaphragm, and the maximum pressure P_o at which strain versus pressure relation remains linear. By modeling silicon as a clamped circular diaphragm, P_m and P_o can be related to sensor parameters by the following equations:

$$P_m = \sigma_m \frac{8}{3(1+\mu)}\left(\frac{t}{a}\right)^2, \text{ and} \qquad (2.43)$$

$$P_o = \frac{8E}{3(1-\mu^2)}\left(\frac{t}{a}\right)^4, \qquad (2.44)$$

where E is Young s modulus of silicon, μ is Poisson s ration of silicon, *a* is the radius of the diaphragm (or the cavity), and *t* is the diaphragm thickness. Though the calculated thickness of silicon diaphragm in one of the sensors is very small (3.4 μm), its maximum stress is about three orders less than the yield strength of silicon (7×10^{10} dynes/cm^2). This ensures that these membranes can withstand 60 or 80 psi.

2.4 Design of Ideal Fabry-Perot Temperature Sensor

A model of the thin-film Fabry-Perot temperature sensor will be developed in this section. This model will provide a basis for a preliminary sensor design, which consists of the selection of a material and the determination of the optimum thickness range. An idealized model will be used which neglects absorption and assumes equal reflectivites at both surfaces of the film.

Consider the thin-film Fabry-Perot interferometer shown in Figure 2.2. The film has a thickness of L and a refractive index of n_1. It is surrounded by a material of index n_0, where $n_1 > n_0$. Collimated light is assumed, and the materials are assumed to be lossless. Then, as derived in section 2.2, the interferometer s reflectance (equation 2.32) is

$$R_F = \frac{FSin^2(\Phi)}{1 + FSin^2(\Phi)}, \qquad (2.32)$$

The interferometer s reflectance is minimized at resonance, or $\Phi = \pi m$, where m is an integer. For the ideal Fabry-Perot interferometer, $[R_F]_{MIN} = 0$.

In terms of wavelength, the resonance condition is $\lambda = \lambda_m$, where

$$m\lambda_m = \Lambda_{OPD}. \tag{2.45}$$

The maximum reflectance, which occurs at $\Phi=\pi(m+1/2)$, is given by

$$[R_F]_{MAX} = \frac{F}{1+F}. \tag{2.46}$$

The interferometer s phase sensitivity is obtained by differentiating equation 2.32, which gives [3]

$$\frac{dR_F}{d\Phi} = \frac{F\sin 2\Phi}{(1+F\sin^2\Phi)^2}. \tag{2.47}$$

The phase sensitivity is a maximum at $\Phi=\pi m\pm\Phi_0$, where

$$\Phi_0 = \frac{1}{2}\cos^{-1}\left(\frac{1}{2}\sqrt{9+4/F+4/F^2} - \frac{1}{F} - \frac{1}{2}\right) \tag{2.48}$$

For small R, $\Phi_0\approx\pi/4$. As R increases and begins to approach 1, Φ_0 approaches 0. For a given Λ_{OPD}, the wavelengths of maximum sensitivity are equal to $\Lambda_{OPD}/(m\pm\Phi_0/\pi)$.

The Fabry-Perot interferometer s maximum phase sensitivity is

$$\left|\frac{dR_F}{d\Phi}\right|_{MAX} = \frac{1}{F}\left[\frac{1}{\sin^3 2\Phi_0} - \frac{1}{\sin 2\Phi}\right]. \tag{2.49}$$

Figure 2.8 shows the dependence of $|dR_F/d\Phi|_{MAX}$ on R. This result will useful in explaining pressure and temperature sensor characteristics in chapter 4.

The temperature sensitivity of the Fabry-Perot s phase shift is given by

$$\frac{d\Phi}{dT} = \pi\frac{\Lambda_{OPD}}{\lambda}\kappa_\Phi, \tag{2.50}$$

where

$$\kappa_\Phi = \kappa_n + \kappa_L. \tag{2.51}$$

Here, κ_n is the thermo-optic coefficient,

$$\kappa_n = \frac{1}{n_1}\frac{dn_1}{dT}, \tag{2.52}$$

and κ_L is the thermal expansion coefficient,

$$\kappa_L = \frac{1}{L}\frac{dL}{dT}. \tag{2.53}$$

The temperature sensitivity of the Fabry-Perot s reflectance can be determined by substituting from equations 2.47 and 2.50 into

$$\frac{dR_F}{d\Phi} = \left(\frac{dR_F}{d\Phi}\right)\left(\frac{d\Phi}{dT}\right) \tag{2.54}$$

2.4.1 Selection of Temperature Sensitive Material

G. Beheim has previously summarized a comparison of candidate materials for a thin-film temperature sensor [3]. The temperature sensitivity of various candidate materials requires that sensitivity figure-of-merit be independent of the film thickness. Assume that the temperature is determined as a function of one of resonant wavelengths λ_m. The relative temperature sensitivity of λ_m is given by

$$\kappa_s = \frac{1}{\lambda_m}\frac{d\lambda_m}{dT}. \tag{2.55}$$

Here, $\kappa_s=\kappa_\phi$. Table 2.1 tabulates the candidate materials in descending order of κ_ϕ. This table provides n, κ_n, and κ_L, together with the wavelengths at which the optical properties were measured. In the case of all the materials except aluminum, the Fabry-Perot interferometer is assumed to be a thin film. The κ_ϕ of aluminum provides the sensitivity of an interferometer

which is comprised of two mirrors separated by an aluminum spacer. The sensitivity of this air-spaced resonator is relatively low.

For all the optical materials listed in Table 2.1, $\kappa_n >> \kappa_L$, so the temperature induced phase change is almost entirely caused by the change in refractive index. The temperature sensitivity κ_n is greatest for high-index semiconductors, which are, in descending order of sensitivity, GaAs, Ge, and Si. For these semiconductors, κ_n is highly wavelength dependent. With decreasing λ, κ_n generally increases, as shown by the entries in Table 2.1 for silicon.

Of the three materials with the largest values of κ_ϕ, silicon is best suited for this application. The material with the highest temperature sensitivity, GaAs, is not sufficiently stable at temperature of 275 ^{0}C [17]. Also, stoichiometric GaAs cannot readily be deposited on the end of a fiber. Germanium, which has the second highest, κ_ϕ, is readily sputter-deposited, however, it is highly absorbing at the emission wavelengths of AlGaAs LEDs. At 830 nm, the absorption coefficient of germanium is 4.5×10^4 cm^{-1}, so that transmission through 1 μm produces a 20-dB loss [14]. At 1.3 μm, α is much lower, 0.68×10^4 cm^{-1}, but this wavelength is outside the range of inexpensive silicon photodiodes. Silicon is preferred to germanium for this application, because its absorption coefficient is much lower at the AlGaAs emission wavelengths. At 830 nm, $\alpha=0.19\times10^4$ cm^{-1}, which causes a 17% absorption in 1.0 μm [14].

In addition to a high κ_ϕ, the Fabry-Perot material should have a high refractive index. A higher value of n provides a larger R, which increases the maximum reflectivity $[R_F]_{MAX}$ and the maximum phase sensitivity $\left|dR_F/d\Phi\right|_{MAX}$. Table 2.2 provides, for each of the candidate materials, $\left|dR_F/d\Phi\right|_{MAX}$ and $[R_F]_{MAX}$, both of which increase with increasing n_1. Once again, absorption of these materials is neglected to simplify this preliminary design. For silicon,

$[R_F]_{MAX}$=0.53, which provides sufficient sensitivity that no reflectivity-enhancing coatings are necessary.

Based on the above considerations and the fact that silicon can be bonded to an optical fiber, silicon was determined to be the best material for the fabrication of a thin-film Fabry-Perot temperature sensor.

2.4.2 Determination of Fabry-Perot Sensor s Thickness

The design principle of thin-film temperature is similar to that of the pressure sensor because both sensors are based on the Fabry-Perot interferometer. However, since we have used a different measurement system involving an optical spectrometer, some design criteria in tracking of spectral resonance is outlined below.

An important design parameter is the interferometer s fringe order, which is given by $m=\Lambda_{OPD}/\lambda_m$, where λ_m is the monitored resonant wavelength and m is an integer. As shown by equation 2.50, increasing m increases the temperature sensitivity of the phase shift Φ. Increasing m also decreases the period of $R_F(\lambda)$, so that analysis of R_F requires the resolution of smaller wavelength differences. The wavelength change corresponding to $\Delta\Phi=\pi$ is termed the free spectral range, $\Delta\lambda_{FSR}$. For moderately large m,

$$\frac{\Delta\lambda_{FSR}}{\lambda_m} \approx \frac{\lambda_m}{\Lambda_{OPD}}. \qquad (2.56)$$

It has been assumed throughout this section that the analyzer s spectral bandwidth $\delta\lambda_A$ and the wavelength sampling interval $\delta\lambda_S$ are both sufficiently small to allow the fringes of $R_S(\lambda)$ to be resolved.

For low values of R, $R_F(\lambda)$ is approximately sinusoidal (for sufficiently large m, figure 2.3) and $\delta\lambda_A$ can be as large as $\Delta\lambda_{FSR}/2$. As R is increased, $R_F(\lambda)$ becomes less sinusoidal (figure 2.3) and is increasingly constituted by components of higher order. Therefore, a smaller $\delta\lambda_A$ is required. For large R, $\delta\lambda_A$ should be smaller than the fringe width (FWHM), which is approximately $\Delta\lambda_{FSR}$ divided by the finesse.

The spectral width of the optical source $\Delta\lambda_{LED}$, imposes a lower bound on the fringe order. To determine Φ independently of the received signal level, $\Delta\lambda_{LED}$ should be large enough to permit the analysis of a good portion, at least 1/2, of a free spectral range. The requirement that $\Delta\lambda_{LED} \geq \Delta\lambda_{FSR}/2$ gives

$$\frac{\Delta\lambda_{LED}}{\lambda_m} \geq \frac{\lambda_m}{2\Lambda_{OPD}}. \qquad (2.57)$$

For a typical AlGaAs LED, λ=850 nm and $\Delta\lambda_{LED}$= 80 nm, which gives m≥5. For silicon, this corresponds to $L_1 \geq 0.62$ μm.

The required measurement range also needs to be considered in determining a design value of m. The temperature increase that causes a phase change $\Delta\Phi=\pi$, thereby shifting λ_{m+1} to the original position of λ_m, is inversely proportional to m and is given by

$$\Delta T_{FSR} = \frac{\lambda_m}{\Lambda_{OPD}\kappa_\Phi}. \qquad (2.58)$$

If the temperature is determined from the resonant wavelength λ_m, or, equivalently, if the temperature is determined by measuring Φ at a fixed wavelength, then the measurement range, T_{MAX}-T_{MIN}, can be no greater than ΔT_{FSR}. That is, T_{MAX} can be no greater than the temperature at which $\lambda_{m+1}(T) = \lambda_m(T_{MIN})$. Thus,

$$m \le \frac{1}{\kappa_{\Phi}(T_{MAX} - T_{MIN})}. \qquad (2.59)$$

For a silicon sensor with a 25 to 300 ^{0}C range, m must be less than 46, which gives L< 6.3 μm. In this case we chose L_1= 3.4 μm so that L_1 is within the above limiting cases.

2.4.3 Sensitivity to Pressure

When used in harsh environments, the sensor will be exposed to a variable air pressure. The effect of pressure on the refractive index of the silicon Fabry-Perot interferometer was estimated by assuming that the refractive index changes can be related to the changes in the bandgap energy E_g. Since dE_g/dT=-0.046 eV/^{0}C and $dE_g/dP=1.7\times10^7$ eV/psi [18], $n^{-1}dn/dP=-2.8\times10^{-10}$/psi is obtained based on the published value for κ_n of $n^{-1}dn/dP=7.6\times10^{-5}/^0$C. The effect of pressure changes on the interferometer s thickness was determined from $L^{-1}dL/dP=-(1-2\nu)/E$. Using the published values for the Young s modulus E and Poisson s ratio ν [19], it was determined that $L^{-1}dL/dP=-3.0\times10^{-8}$/psi. Combining the effects of changes in *n* and L, the sensitivity to pressure of the sensor s output was determined to be $dT_M/dP=-4.0\times10^{-4}$ ^{0}C/psi. This degree of cross sensitivity is insignificant for most of the applications where the range of pressures will be much less than 100 psi.

2.4.4 Design of Encapsulation for Temperature Sensor

Silicon nitride oxidizes very slowly and is largely impermeable to oxygen and water [12]. For these reasons it is widely used as a mask for the selective oxidation of silicon [13]. The optical properties of the three-film structure, $Si/Si_3N_4/Al$, will now be considered in the design of

the encapsulation structure. We follow here a design procedure previously used by G. Beheim [3].

The Si_3N_4 layer constitutes a second Fabry-Perot resonator, which is coherently coupled to the much thicker silicon resonator. Normal incidence will be assumed. The complex phase shift (one-way) of the silicon resonator is then

$$\Omega_1 = \frac{2\pi}{\lambda} N_1 L_1 . \tag{2.60}$$

The real part of Ω is

$$\Phi_1 = \frac{2\pi}{\lambda} n_1 L_1 . \tag{2.61}$$

Since k_2=0, the phase shift of the Si_3N_4 resonator is real so that $\Omega_2=\Phi_2$, where

$$\Phi_2 = \frac{2\pi}{\lambda} n_2 L_2 . \tag{2.62}$$

To be an effective diffusion barrier, the Si_3N_4 layer need not be thick, L_2>10 nm is adequate. Because of the disparity in L_1 and L_2, it makes intuitive sense to model the sensor as a silicon Fabry-Perot interferometer, the second mirror of which is nitride-coated aluminum. Because the Si_3N_4 layer can be very thin, its order of interference can be chosen so that the reflectivity of the nitride-coated aluminum does not vary significantly over the spectral range of the LED.

Figure 2.9 shows the three-film sensor structure. Here the materials 0 through 3 are the SiO_2 optical fiber, the silicon, the Si_3N_4, and the aluminum films, respectively. Following the derivation in the section 2.2, the sensor s amplitude reflectance is determined to be

$$r_F = \frac{-r_{10} + r_{123}\exp(j2\Omega_1)}{1 - r_{10}r_{123}\exp(j2\Omega_1)}, \tag{2.63}$$

where the amplitude reflectance of the nitride-coated aluminum is

$$r_{123} = \frac{-r_{21} + r_{23}\exp(j2\Omega_2)}{1 - r_{21}r_{23}\exp(j2\Omega_2)}. \qquad (2.64)$$

The reflectivity of the nitride-coated aluminum, $R_{123}=|r_{123}|^2$, is maximized (assuming all n and k are λ independent) at the anti-resonance condition, which is

$$2\Phi_2 + \Phi_{21} + \Phi_{23} = \pi(2p+1), \qquad (2.65)$$

where Φ_{21} and Φ_{23} are the phase shifts associated with r_{21} and r_{23} and p is an integer. Since k_1 is small and $n_1>n_2$, $\Phi_{21}\approx\pi$. If the aluminum is modeled as an ideal metal (i.e. k_3 infinite), then $\Phi_{23}=-\pi$. The reflectivity R_{123} is then a maximum for $\Phi_2=\pi(p+1/2)$. The zeroth-order reflectance maximum, $\Phi_2=\pi/2$, is in this case provided by a quarter-wave layer, i.e. L_2=106 nm for λ=830 nm.

At λ=850 nm, the complex refractive indices are N_1=3.664+j0.005, N_2=2.01, and N_3 =2.92+j7.76. Figure 2.10 shows $R_{123}(\lambda)$ which was calculated using these refractive index values, for L_2=0, 106, and 318 nm. The non-zero values of L_2 are approximately the thicknesses that provide zeroth and first-order constructive interference at λ=850 nm. As shown by figure 2.8, a larger interference order requires more precise control of the film s thickness, if one is to obtain an $R_{123}(\lambda)$ that is approximately constant over the LED s spectral width. Since thicker nitride layer provides no apparent benefit, L_2 was fixed at 106 nm.

Besides the reflectance magnitude, the phase change on reflection is also important, as the phase change Φ_{123} determines the resonance condition of the encapsulated silicon interferometer. That is, it determines the spectral position of resonance. Since we are interested in spectral shift of these resonance points, absolute position of these resonance points is not important. Therefore, as an approximation, we will take Φ_{123} to be constant in the vicinity of λ=850 nm. Because R_{123} is approximately constant and for $800<\lambda<900$ nm, $R_F(\lambda)$ of the dual cavity

interferometer is very similar in form, over the LED s spectral range, to $R_F(\lambda)$ of the uncoated silicon Fabry-Perot interferometer.

Because of the considerably higher reflectivity of the encapsulated silicon s back surface, considerable increase in fringe visibility can be seen in the plot of reflectivity versus wavelength for L_1= 3.4 μm, and L_2= 106 nm. A high fringe visibility, in the wavelength range of operation, is desired as this makes it possible to more accurately determine the interferometer s resonant wavelength, in spite of perturbations to the spectrum which are caused by the fiber-optic link.

2.5 Concluding Remarks

An expression for reflectivity from a thin film that forms Fabry-Perot interferometers was derived using Maxwell s equations. A pressure sensor based on Fabry-Perot interferometer was designed for operating in the pressure range 1-80 psi. This design was done for use of the pressure sensor in a LED based reflectometry measurement system.

A thin-film temperature sensor was designed for operating in the temperature range 25-300 ^{0}C. Aluminum-coated silicon nitride (Si_3N_4/Al) was proposed as a structure, which should act as an oxidant-impermeable encapsulant providing long-term stability. The optimum thickness of layer was determined to be 106 nm. The effect of encapsulating films on the temperature sensitivity κ_ϕ was shown to be negligible in a previous study [3]. An idealized model was used which neglects absorption and assumes equal reflectivites at both surfaces of the film.

2.6 References

[1] C. R. Paul, and S. R. Nasaar, Introduction to Electromagnetic Fields , McGraw-Hill, New York, 2 nd ed., 1987.

[2] A. Yariv, Quantum Electronics , Wiley, New York, 4th ed., 1998.

[3] Glenn Beheim, Fiber-Optic Temperature Sensor Using a Thin-film Fabry-Perot Interferometer , Ph.D. thesis, Case Western Reserve University, Cleveland, Ohio, May 1996.

[4] Mario Di Giovanni, Flat and Corrugated Diaphragm Design Handbook (Mercel Dekker, NewYork), 1992.

[5] D.T.E. Marple, Refractive Index of GaAs , J. Appl. Phys., 35, pp.1241, 1964.

[6] S.S. Ballard, K.A. McCarthy, W.L. Wolfe, Optical Materials for Instrumentation , University of Michigan Report No. 2389-11-S, 1959.

[7] H.W. Icenogle, B.C. Patt, W.L. Wolfe, Refractive Indices and Temperature Coedfficients of Germanium and Silicon , Appl. Opt. 15, 2348, 1976.

[8] W.G. Driscoll,ed., Handbook of Optics, (McGraw-Hill, New York, 1978).

[9] S.M. Sze, Physics of Semiconductor Devices, 2nd Edition, pp. 851, John Wiley & Sons, New York, 1981.

[10] G. Cocorullo, and I. Rendina, Thermo-Optical Modulation at 1.5 μ m in Silicon Etalon , Electronic Letters, 28, pp. 83, 1992.

[11] H.H. Li, Refractive Index of Silicon and Germanium and its Wavelength and Temperature Derivatives , J. Phys. Chem. Ref. Data 9, pp. 561, 1980.

[12] G.E. Jellison, Jr. and F.A. Modine, Optical Functions of Silicon at Elevated Temperatures , J. Appl. Phys., 76, pp. 3758, 1994.

[13] R.J. Harris, G.T. Jonston, G.A. Kepple, P.C. Krok, and H. Mukai, Infrared Therooptic Coefficient Measurement of Polycrystalline ZnSe, ZnS, CdTe, CaF_2, and BaF_2, Single Crystal KCl, and Ti-20 Glass , Appl. Optics, 16, pp.436, 1977.

[14] E.D. Palik, ed., Handbook of Optical Constants of Solids, Academic Press, Orlando, 1985.

[15] W.J. Lu, A.J. Steckle, T.P. Chow, and W. Katz, Thermal Oxidation of Sputtered Silicon Carbide Thin Films , J. Electrochem . Soc., 131, pp. 1907, 1984.

[16] G. Beheim, K. Fritsch, and D.J. Anthan, Fiber-Optic Temperature Sensor Using a Spectrum-Modulating Semiconductor Etalon , NASA TM-100153, 1987.

[17] J.M. Molarius, E. Kolawa, K. Morishita, M.A. Nicolet, J.L. Tandon,J.A. Leavitt, and L.C. McIntyre,Jr., Tantalum-Based Encapsulants for Thermal Annealing of GasAs , J. Electrochem. Soc, 138, pp. 834, 1991.

[18] S.M. Sze, Physics of Semiconductor Devices, 2nd Edition, pp. 15-16, John Wiley & Sons, New York, 1981.

[19] K.E. Petersen, Silicon as a Mechanical Material , Proc. IEEE 70, pp.420, 1982.

Material	$\lambda(\mu m)$	n	κ_n	κ_L	κ_ϕ
GaAs	0.9	3.6[4]	120[4]	5.7[5]	126
Ge	2.55	4.06[6]	100[6]	5.7[7]	106
Si	2.5	3.44	46[6]	2.6[8]	
	1.5	3.5	53[9]		
	1.26	3.51[10]	59[10]		
	0.78	3.695[11]	76[11]		79
CdTe	1.15	2.79[12]	53[12]	5.0[12]	58
TiO_2	0.7	2.55, n_0[7]	16[5]	7.1[5]	23
		2.83, n_e[7]	35[5]	9.2[5]	44
ZnS	0.63	2.35[12]	27[12]	6.9[12]	34
Al	—	—	—	23	23
MgO	0.77	1.74[5]	8.1[5]	14[5]	22
Si_3N_4	0.80	2.01[13]	NA	2.8[14]	19[15]
SiC	0.83	2.61[16]	NA	4.2[14]	17[16]
SiO_2	0.63	1.46[7]	15[7]	0.5[7]	15
Al_2O_3	0.85	1.76[7]	10[7]	5[7]	15

Table 2.1 Properties of candidate Fabry-Perot materials. Units of κ_n, κ_L, and κ_ϕ are $10^{-6}/^0C$.

Material	n	$\left\| dR_F/d\Phi \right\|_{MAX}$	$[R_F]_{MAX}$	$\delta T_\theta(^0C)$
GaAs	3.6	0.58	0.51	12
Ge	4.06	0.71	0.59	12
Si	3.695	0.60	0.53	19
CdTe	2.79	0.34	0.32	44
TiO_2	2.55, n_0	0.26	0.26	130
	2.83, n_e	0.35	0.34	58
ZnS	2.35	0.20	0.20	110
MgO	1.74	0.03	0.03	300
Si_3N_4	2.01	0.10	0.10	250
SiC	2.61	0.28	0.27	170
SiO_2	1.46	0	0	630
Al_2O_3	1.76	0.03	0.03	430

Table 2.2 Properties of Fabry-Perot temperature sensors fabricated from candidate materials.

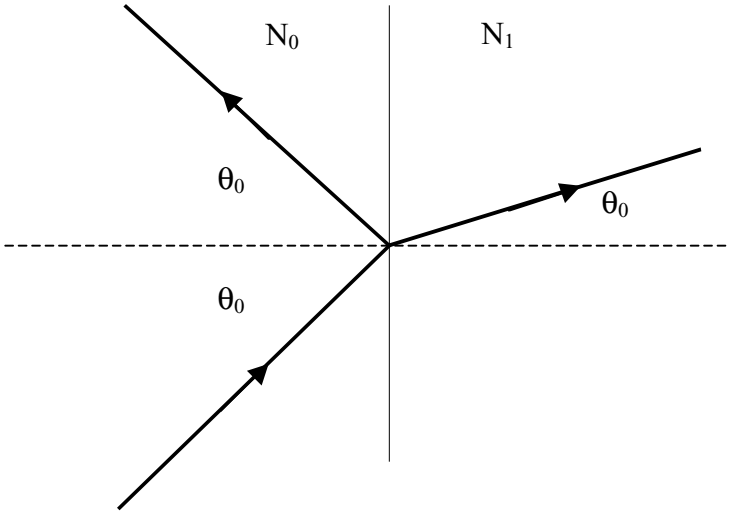

Figure 2.1 Transmission and reflection at an interface between two materials with complex refractive indexes N_0 and N_1.

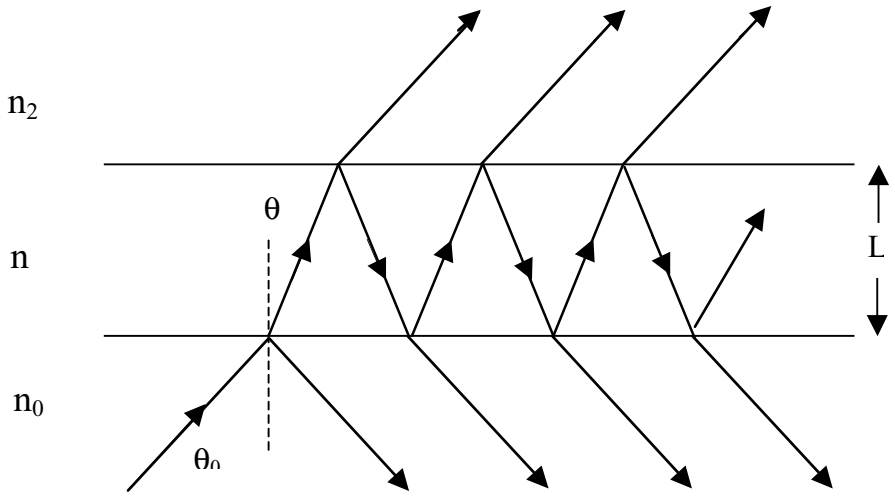

Figure 2.2 Transmission and reflection from a single film.

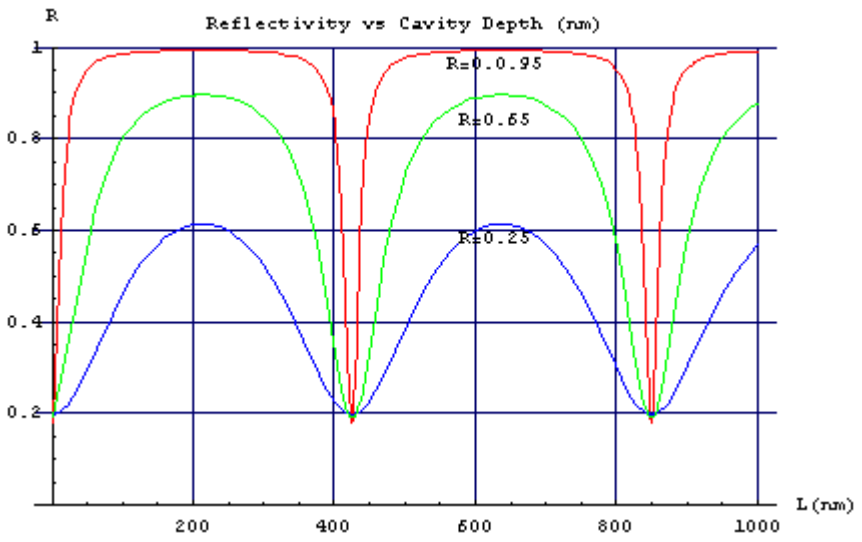

Figure 2.3 $R_F(\Phi)$ is plotted for different values of R. A larger R narrows the reflectance minima, or fringes.

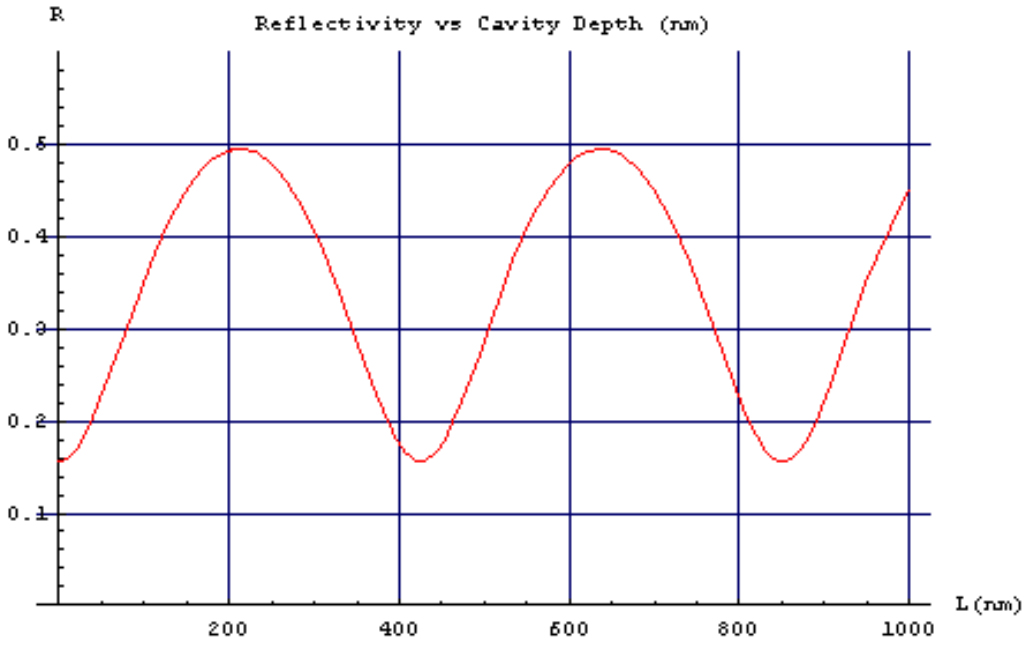

Figure 2.4 Periodic variation of the reflected light intensity from a Fabry-Perot type sensor as a function of separation of reflectors (or the cavity depth h in this case).

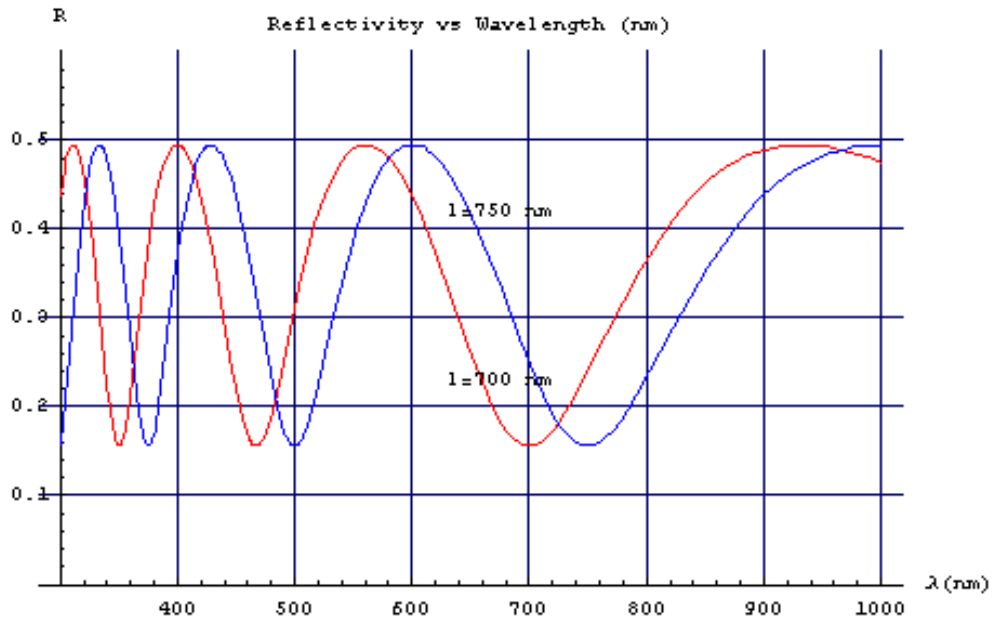

Figure 2.5 calculated R_F versus wvelength for a Fabry-Perot with N_0=1.5, N_1=1, and N_2=3.46 for two different values of widths.

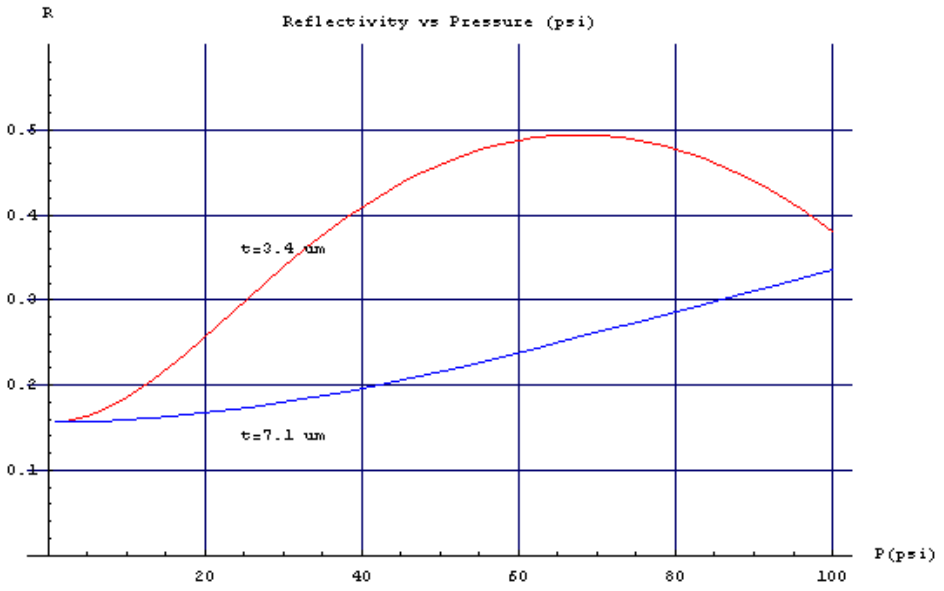

Figure 2.6 Calculated sensor responses with respect to pressure for two cases of diaphragm thickness t=3.4 μm, and t= 7.1 μm,

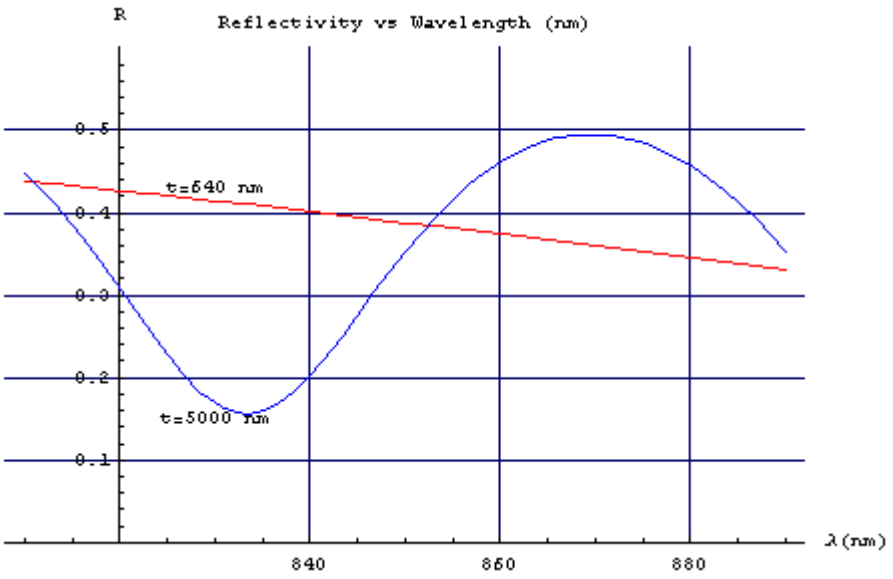

Figure 2.7 Calculated reflectivity versus wavelength of a Fabry-Perot pressure sensor for two cavity depths, one that meets the condition given by equation 2.42, and another that exceeds the limit of 3.6 μm.

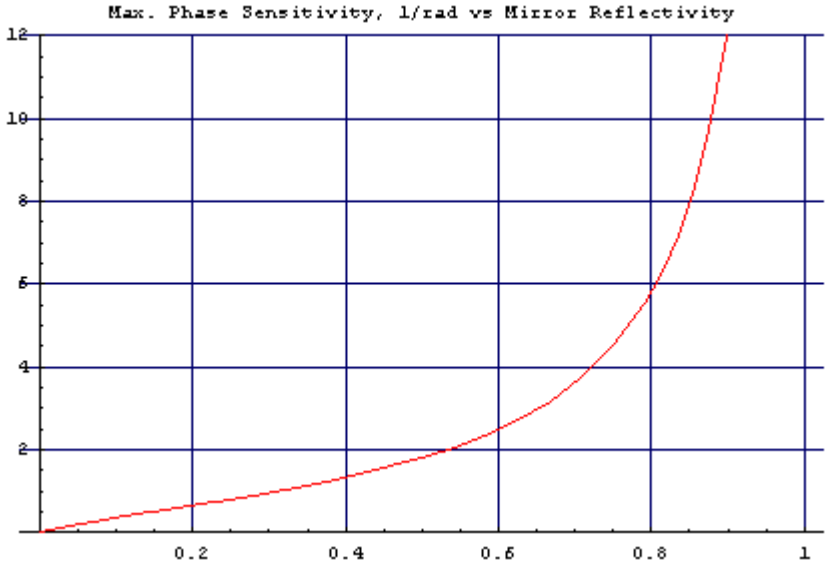

Figure 2.8 The dependence of $\left|dR_F/d\Phi\right|_{MAX}$, Fabry-Perot interferometer s maximum phase sensitivity, on R, the reflectivity.

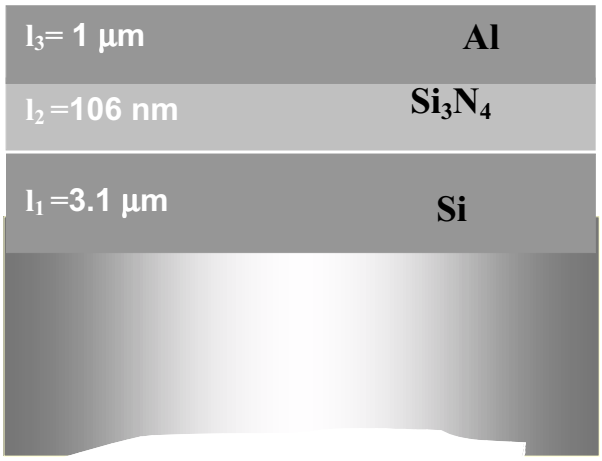

Figure 2.9 The three-film sensor structure. The materials 0 through 3 are the SiO_2 optical fiber, the silicon, the Si_3N_4, and the aluminum films, respectively.

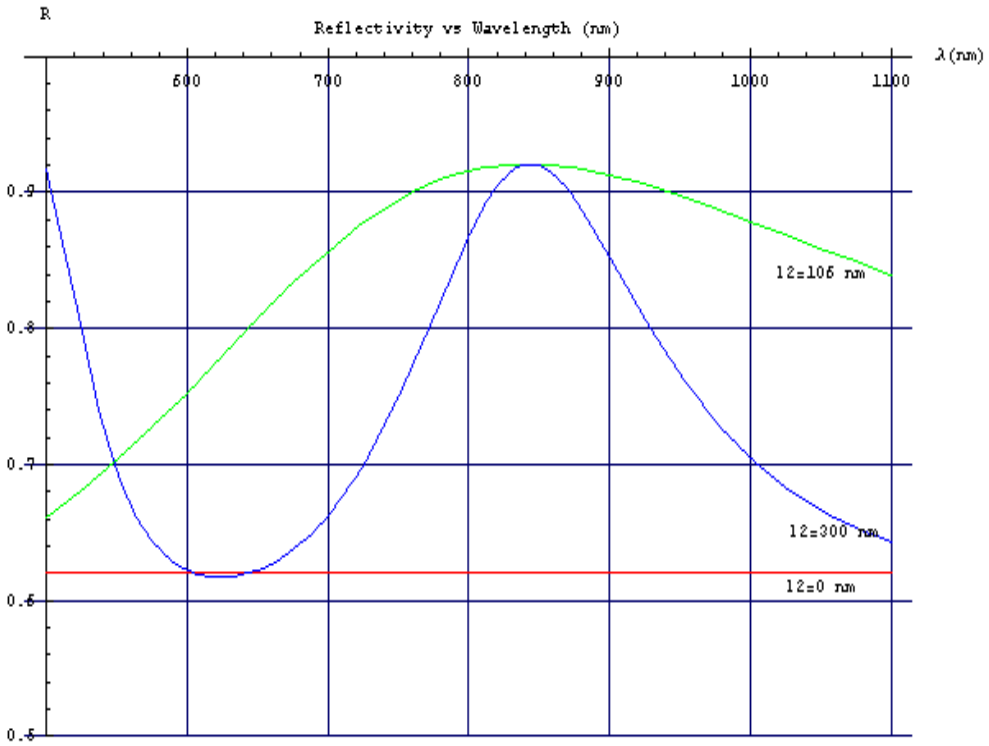

Figure 2.10 Calculated $R_{123}(\lambda)$using these refractive index values, for L_2=0, 106, and 318 nm.

3.0 Fabrication of Sensors

3.1 Introduction

The fabrication of sensors incorporated MEMS compatible michromachining processes. Even though silicon micromachining conventionally applies processing onto a wafer, we have done it on a commercial optical fiber end; in addition, the light guiding capability of the optical fiber was utilized.

Our approach in micromachining an optical fiber end is unconventional in that the area of the fiber end face where a cavity is etched is very small (<1 mm^2). An obvious drawback with this approach is the difficulty in controlling the thickness of photoresist and in applying photoresist uniformly. The details of each process and its limitations are discussed in this section; bonding of the fiber to silicon is discussed in detail including some characterization results of this process. Fabrication of a single pressure sensor fabricated on an optical fiber is presented starting with a summary of the fabrication process. Fabrication of a linear fiber sensor array, and a temperature sensor are also discussed.

3.2. Summary of Fabrication of Pressure Sensor

The core of this thesis is the fabrication of the sensor configuration shown in Figure 1.1 on an optical fiber. We have devised a fabrication plan where the key design parameters such as of

diaphragm thickness, initial cavity depth, and cavity diameter can be achieved for the calculated values to provide linear response over various pressure ranges. The main processing steps are summarized in this section (Figure 3.1).

The fibers used have cladding diameters of 200 and 400 _m. A cavity at the end of a fiber is formed in an innovative way by patterning its end photolithographically, and then wet etching of the fiber core area in a buffered HF solution (NHF_3: HF≡12:1). Thinned Shepley 1818 positive photoresist (thinner: Shepley 1818≡1: 2) was used to form a thin layer of photoresist. The cavity on the fiber end face was formed photolithographically by removing photoresist on the core; two different exposure techniques were used. Buffered HF was used in etching 0.5 _m deep cavities. Next step was to bond a thin silicon diaphragm onto the fiber end using anodic bonding [1], which is used commonly in MEMS for bonding glass and silicon wafers. We envisioned that we could use this bonding mechanism for bonding silicon to optical fibers since optical fibers are made out of glass. Extremely thin silicon wafers (3-10 _m) are now commercially available and have been used in our early experiments.

3.3 Fiber Cleaving & Polishing

The first step in general for cleaving or polishing is to strip enough of the jacket from the fiber to allow scribing the cladding of the fiber. However, the custom made borosilicate glass fibers we used did not have a jacket. Therefore, the first step was to clean the fibers with reagent grade isopropyl alcohol. A Kimwipe moistened with a little alcohol was used. Determination of the length of the fiber used was based on the convenience of handling them through the rest of the fabrication process. In most of the cases fibers were cut into 7-10 cm long pieces. Fibers were cleaved using a Fujikura Precision Fiber Cleaver. According to the manufacturer, this

cleaver consistently yields end faces that are perpendicular to the fiber axis within $\pm 1^0$. As the Figure 3.2 shows, the fiber end faces of the cleaved fibers are not uniformly flat across the fiber end face [2]. This is common with any cleaving tool and is the case with fibers of any size. For this reason, and the need for flat (and smooth) fiber end faces for bonding silicon onto these end faces, we follow a tedious polishing step.

The fiber sample for polishing is mounted inside a ferrule of a SMA-type connector by enlarging the ferrule diameter to the diameter of the fiber and by applying epoxy to the backside of the connector. The fiber extended from the ferrule by a length less than its diameter in order to minimize the chances of breakage during polishing. Then the SMA connector was inserted into a polishing disc (Figure 3.3) by making sure that the fiber end would not protrude past the bottom surface of the polishing disc. Polishing papers of three different grit-size-papers were used; they are (in the order polishing carried out) 3 _m, 1_m, and 0.3 _m. Each time, the polishing paper was changed from higher to lower grid size paper, the fiber end face was cleaned with isopropyl alcohol and dried immediately afterwards by blowing dry nitrogen [3]. In order to obtain a smoother surface polishing, Cerium Oxide polishing liquid (COPL) by Beuler Inc. was used. COPL is supposed to act not only as a good mechanical polishing agent, but also as a chemical agent that enhances the surface smoothness further. Again, polishing was carried out by diluting COPL with water in the following order: undiluted COPL, 2:1 diluted in water, 4:1 diluted in water. These steps of polishing on soft cloth paper with COPL gave better results in terms of average smoothness of the fiber end face.

3.4 Characterization of Fiber End Faces Using Atomic Force Microscope (AFM)

Polished fiber end faces were characterized by topography measurements of Atomic Force Microscopy (AFM). Fibers had to be cut into very short (~3 mm) pieces in order to use with AFM. Taking advantage of the ease in handling the AFM tip onto a desired point very accurately, we took surface topography on the cavity bottom, which acts as a reflector in the Fabry-Perot sensor. The AFM used has a vertical resolution of 5 . Figure 3.4 shows AFM measurements of the cavity bottom. Surface roughness numbers are low enough to treat the cavity bottom as optically polished. Since the RMS surface roughness is much smaller than the wavelength of operation (850 nm), these surfaces can be considered as optically polished. Further, we used AFM line profile measurements to determine the cavity depth, which in most of the cases was less than 1 _m. As Figure 3.5 shows, AFM line profile of an 80-_m-diameter cavity has a flat bottom and a satisfactory roughness number of 10 nm. The line profile of a cavity is also useful in determining the cavity depth; this method was employed in determining the etch rate for borosilicate glass fibers.

3.5 Photolithographic Patterning of Cavity

Prior to application of photoresist, an adhesion promoter, HMDS, was applied on the fiber end. A thin layer of thinned Shipley 1818 positive photoresist (photoresist: thinner = 2:1) was applied by dipping on the same fiber end followed by soft baking for 15 minutes in an oven at 90 ^{o}C. The thickness of photoresist could not be controlled. The thickness was found to vary between 3 to 5 _m- a drawback of this method. The cavity on the fiber end face was formed by photolithographic patterning utilizing two different exposing techniques (Figure 3.6). Both of these techniques used blue Argon ion laser light (λ = 457.9 nm) for exposing photoresist. The first technique involved coupling blue Argon laser light into the opposite fiber end from the one

on which fabrication would take place using a low magnification microscope objective (5X). A low magnification objective was necessary because the beam diameter had to be nearly equal to that of the core diameter in order to get Gaussian beam emerging from the other end where photoresist was coated. This technique exposed the photoresist leaving a circular area of photoresist whose diameter was equal to that of core diameter of the fiber. A red light lamp coupled to the microscope, CCD camera mounted to the microscope, and a TV monitor (Figure 3.7) was used for initial focusing of the fiber. As shown in this figure, the position where the laser beam would be focused was marked on the TV screen. The fiber was aligned so that its center coincided with this point. A typical exposure power in one of our experiments was 100 W exposed for 60-80 sec using this technique. Figure 3.8 shows a picture of a patterned Corning MM fiber (100/140 _m) where a circular area of PR is removed. The removed area has a diameter of 100 _m equal to that of the core of the fiber. This technique was found to be very accurate (< 2%) in forming a cavity to a designed diameter.

The second technique simply directed blue light onto the photoresist-coated fiber end face using a high magnification objective (50X). Red light was used as before for focusing the fiber end face (approximately the same focusing point (horizontally) was observed for blue laser light) while the second technique caused the photoresist to develop leaving a circular area whose diameter was equal to the beam diameter. The fiber was then raised up from focus by an amount that was determined previously for obtaining a given beam diameter. Vertical motion could be controlled to an accuracy of ± 1 μm. This latter technique was found to be less accurate in forming a calculated cavity diameter since the 50X objective produces diffraction effects and spatial spreading of the beam at the perimeter of the laser beam (see Figure 3.6) as one moves off-focus. The appropriate exposure power depends on the photoresist thickness and can be

determined in conjunction with exposure time for a given case. The exposure time of course depends on the photoresist thickness and laser power; for example, 100 W exposed for 30-40 sec was typical. Figure 3.9 shows a picture of a patterned MM fiber (400 _m diameter) where a circular area of PR is removed in the central portion of the core. The removed area has a diameter of 92 _m.

Development of the exposed fibers was carried out by dipping the fibers in 5:1≡DI H_2O: Microposit 351 developer solution for 30-50 Sec. After this time period, fibers were dipped in DI H_2O for 5 minutes followed by blowing dry nitrogen. Following this, fiber end faces were observed under optical microscope to determine if the developing time was sufficient. Development time is dependent on the exposure power, exposure time, and photoresist thickness [4]; since photoresist thickness could be controlled to be within only 2 μm, development time varied from 30 to 50 sec for 400 μm diameter fibers. We therefore, repeated the above steps starting with the developing time of 30 Sec. until we observed under the microscope that the fibers end faces were not under developed. Before the etching process, patterned-fibers were hard baked in an oven at 120 ^{0}C for 30 minutes to allow evaporation of any solvents remaining.

3.6 Wet Etching of Fiber Tip

Wet etching was chosen for forming a cavity because it is simple, and yet it can be done in a controlled manner. Hydrofluoric (HF)- based etchants are typically used for etching of silicon dioxide. Several similar reactions for the HF-based etching of silicon dioxide are given in literature. For pure HF etching, the overall reaction is [5], [6],

$$SiO_2 + 6HF \longrightarrow H_2SiF_{6(aq)} + 2H_2O.$$

The reaction in Buffered HF solutions is

$$SiO_2 + 4HF + 2NH_4F \longrightarrow (NH_4)_2SiF_6 + 2H_2O.$$

And the reaction involving the HF ion (discussed below) is

$$SiO_2 + 3HF_2^- + H^+ \longrightarrow SiF_6^{2-} + 2H_2O.$$

HF is a weak acid; except when present in very small concentrations, it does not completely dissociate into H^+ and F^- ions in water. The etch rate of both silicon dioxide and silicon nitride increases linearly with the concentrations of both HF and HF_2^- for concentrations lower than 10M, while being independent of the concentration of F^- ions alone. The HF_2^- complex attacks oxide about 4.5 times faster than HF. Higher- order complexes, such as $H_2F_3^-$, appear to occur at higher HF concentrations (e.g., in 49% HF) and attack oxide even faster than HF_2^- [7]. Thus, etch rate increases faster than linearly with HF concentration. As HF and HF_2^- are consumed, the etch rate decreases. Buffering with NHF therefore, helps to keep the pH and thus the concentrations of HF and HF_2^- constant, stabilizing the etch rate [8].

Since the cavity depth (0.640 μm) of Fabry-Perot fiber optic pressure sensor needs to be etched very accurately, the etching process requires high control. For this reason, we used buffered HF in etching of patterned fiber end faces. Initially, BHF (5:1) (also known as buffered oxide etch, or BOE) were used in our etching experiments. 5:1 refers to five parts by weight of 40-weight-percent ammonium fluoride (the buffer) to one part by weight 49-weight-percent hydrofluoric acid. It was found that the etch rate for borosilicate glass was too high (780˚nm/min), and as a result, the total etch time for etching 0.640 μm deep cavity is less than one minute. This low etching time causes significant inaccuracies in etch depth; therefore, NH4F: HF≡12:1 (BHF) was used. This resulted in a measured etch rate of 120 nm/min, thus making the total etching time to be 5-6 min (Figure 3.10).

The etching was done at room temperature. Because, this etchant is buffered, its etch rate does not vary much with use. Moreover, this etchant can be masked with photoresist (the adhesion is much better than in higher concentrated HF). Etch rate was determined by measuring the depth of 100 μm diameter cavity etched at different time intervals. Cavity depths were determined using AFM line profile measurements; AFM was preferred over profilometer (typically used in profilometry measurements in micromachining) because AFM tip could be easily positioned over any region of interest on fiber end face. In addition to the above advantage, AFM can produce high-resolution 2-D topography, and is more accurate in surface roughness measurements. Experimental results of etch rates are summarized in Figure 3.10. Two sets of data points and their average is shown in this figure. This plot shows the etch depth for patterned (400 μm diameter fiber, and 100 μm diameter patterned circular area) borosilicate glass fiber. As can be seen from the above plot, the absolute change in etch-depth for the two trials decreases with longer etching times. This may be due to instability in the etch process at the beginning leading to more scattered data points than at longer etch times. An etch rate could be listed because the computed standard deviation for the points was smaller than the average rate. The calculated etch rate is 120 ± 6 nm.

Wet etching of cavities described above was followed by removal of photoresist from the fiber tips. Dipping in Acetone at room temperature was done for this purpose, but at certain instances where photoresist was not removed easily, Acetone cleaning was done at elevated temperatures (70 ^{0}C) by keeping the Acetone beaker on a hot plate for up to 5-10 minutes. Special care was taken not to let Acetone become depleted as a result of evaporation under these elevated temperatures. Acetone cleaning was followed by Base cleaning where further cleaning of the fibers was done. Mixing 1 part of Ammonium Hydroxide with 5 parts of DI H_2O and

heating this mixture up to 70 ^{0}C on a hot plate and then by adding another part of Hydrogen Peroxide (H_2O_2) made the base cleaning solution. Fibers were dipped in this solution for 15 minutes and then rinsed in running DI H_2O.

3.7 Bonding of Silicon to Optical fiber tip

The expression wafer bonding means sticking of surfaces to one another without intermediate adhesives. This will occur if two surfaces of matter come close enough for atomic bonds to establish across their interface. This requires that the surfaces be extremely flat, smooth, and clean. The atomically flat surfaces such as those on silicon wafers will, when stacked without any applied external pressure and temperature, adhere and establish bonds of hydrogen character. When exposed to sufficient thermal treatment (annealing), these initial bonds will be replaced by stronger ionic, covalent and metallic ones and as such merge irreversibly. This is called direct bonding . It was first reported by Lasky etal in 1985 [9] and has since then been surveyed considerably and matured into an indispensable tool in MEMS. Hermetic sealing of cavities, packaging, electrical isolation of material and assembly of devices are just a few examples of frequent applications of direct bonding in MEMS.

Despite the usefulness of semiconductor direct bonding there are two major drawbacks to the technique, one being the high temperatures needed (900-1200 ^{0}C), and the other being the strict demands on surface smoothness. The high temperature limits the flexibility and use of other techniques in MEMS toolbox as low-temperature process steps such as aluminization cannot be performed prior to bonding due to its low temperature melting point (660 ^{0}C). The extremely high demand for surface smoothness can impede hermetic sealing of processed wafers.

The bonding of silicon to fiber uses a complementary bonding method: anodic bonding. This is a well-established and versatile tool that allows fairly rough surfaces (1 m) [10] to be bonded at relatively low temperatures (50—450^{0}C). Field-assisted bonding or hermetic glass-metal sealing are alternative terms for anodic bonding. It cannot be considered as a direct bonding technique, as the bonding mechanism does not initiate spontaneously.

3.8 Ultra-thin Silicon Wafers

Calculated values of silicon diaphragm-thickness for the pressure and temperature sensors were in the range 2-10 _m. These Ultra-thin silicon wafers are commercially available for various MEMS applications. Ultra-thin wafers are defined as single-crystal, silicon wafers with thickness below ~ 200 _m, near the limit of mechanical thinning techniques. Virginia Semiconductor, Inc. of Fredericksburg, Virginia, USA, produces these wafers with thickness down to ~ 2 _m with diameters up to 4 inches.

One advantage of using ultra-thin wafers and incorporating bonding is it removes the thinning step from pressure sensor fabrication. No etching or polishing steps are required in fabricating the pressure membrane since the bonded wafer is already the desired thickness. Another advantage of using ultra-thin silicon wafers is that the thickness variation, doping, and uniformity of the membrane are all known and controllable before fabrication. In contrast, membrane thickness control is about 0.5 _m for etch-stop techniques of thinning silicon wafers and the membrane doping profile and concentration is dependent upon the specific etch or polish method [11]. Doping concentrations and profiles are comparable to normal thickness wafers and Total Thickness Variation (TTV) is generally less than 2 _m over 2-inch wafer; thickness variation for these ultra-thin wafer pieces over a 400 _m diameter optical fiber we used in our

experiments can be considered constant. Bond-quality, ultra-thin wafers are double side polished and have micro roughness 10 comparable to prime grade, normal thickness wafers. Figure 3.11 shows a picture of a 10 _m thick wafer exhibiting the flexibility of these thin silicon membranes.

To a thickness of about 100 microns, ultra-thin wafers are mechanically similar to normal wafers and can be processed using standard techniques. As the thickness decreases further, the wafer exhibits greater flexibility to the point, at about 20 _m thick, that the wafer can be deformed into a tube, with the wafer flat contacted with the opposite edge. At a thickness less than about 10 _m, ultra-thin wafers become transparent to visible light. It is believed that the increased flexibility allows ultra-thin wafers to bond to surfaces with roughness orders of magnitude greater than the limit for bonding normal thickness wafers. This is especially advantageous in our case where the fiber end face has significant surface roughness of ~10 nm (measured with AFM) resulting from polishing. The decreased thickness also makes ultra-thin wafers more susceptible to breakage from mishandling. But, our fabrication process was such that it requires minimum handling of these ultra-thin wafer pieces.

3.9 Anodic Bonding Mechanism

Anodic bonding, i.e. hermetic sealing of glass and metal at temperatures several hundred degrees below thermal softening of glass, was first reported in the pioneering article Field-assisted glass-metal sealing by G. Wallis and D. Pomerantz in 1969 [12]. This phenomenon is based upon the high electrostatic field that develops over the wafer interface as a voltage is applied over the materials to be bonded. The electrostatic field brings the wafers into close

enough proximity for the surface atoms to establish irreversible chemical bonds across the interface.

The set-up for anodic bonding is analogous with an electrochemical cell with the glass acting as a solid electrolyte embodying mobile ions, which transport charges to the electrodes as a dc-field is applied (Figure 3.12). The cathode is contacted to the glass wafer. The metallic wafer at the bonding interface serves as the anode. An electrochemical half-cell reaction at the anode supplies the circuit with electrons by oxidation of the silicon. Stable silicon dioxide is formed at the bonding interface as the glass furnishes the anode with oxygen. A prerequisite for the anodic oxidation of silicon at the bond interface is that the area is furnished with oxygen. Oxygen-ions are embodied in the glass have fairly high activation energy and are not easily displaced. Cations on the other hand, especially alkali ions such as Na^+, Li^+, and K^+, hold comparatively small activation energy and start to migrate at fairly low process temperature and voltage. Na^+ in Pyrex (the most frequently used glass used for anodic bonding) has a calculated activation energy $E_a \approx 0.97\pm 0.14$ eV [13]. Hence, as temperature is raised and voltage applied, the positive monovalent and divalent ions embodied by the glass are removed from the vicinity of the anode an ion-depleted region will arise in the wafer interface. As this depletion layer is of major importance for the anodic bonding process, a critical characteristic of the anode material is that it must not inject mobile ions into the glass, i.e. the anode material must be ion blocking . A major part of the applied dc voltage will divide between this depleted region and the initial space between the wafers (V_d+V_1) (Figure 3.12). A large electric field arise that pull the wafers into close proximity and also render possible for the migration of oxygen towards the bond interface. The bonding current decreases with time due to the growth of the depletion region and

the electronically isolating interface oxide. Densification of the depleted region is another reason for the bonding current to abate with time [14].

Anodic bonding parameters have to be selected carefully in order to guarantee a satisfactory and reproducible seal. Incorrect choices result in unwanted effects such as oxidized silicon tracks, non-hermetic seals [15], warped wafer stack [16], plastic deformation of glass [10], sealed cavities [17], and void formation, which will hamper with the quality of the performance of a device. Anodic bonding process parameters such as voltage, temperature, time, electrode configuration, pre-treatment of wafers, bonding atmosphere, surface morphology and heating source have to be pondered upon before application. Important parameters and their effect on anodic bonding are presented below.

3.9.1 Temperature and Voltage

The process temperature affects bonding quality and reliability in two major ways:

(1) The mobility of ions in the bulk glass drastically increase with increasing temperature, leading to a consequent increase in the initial electrostatic force pulling the wafers into contact. At low temperature on the other hand, the initial electrostatic attraction of the wafers is smaller due to low mobility of ions within the glass, leading to a relatively slow formation of the space-charge region. Go *et al* [18] have shown that the temperature is the parameter having the greatest influence on anodic bond strength whereas bonding temperature, voltage and electrode configuration together are those of major importance for bonding velocity.

(2) Residual stress remains in the device due to mismatch in thermal expansion coefficient of the bonded materials. Internal stress due to thermal mismatch of anode material and glass has

negative effect on the reliability of a device. As an example, capacitive characteristics of a device will alter if the membrane distance varies due to buckling. This is truer for Fabry-Perot interferometer type devices with flexing silicon diaphragm since they are inherently very sensitive. The reproducibility finally, will be uncertain and membrane buckling deteriorates the properties of, and sometimes even destroys, the functionality of capacitive and optical devices [19].

3.9.2 Fabrication of a shallow cavity of extreme height-to—width ratio

The most common way of performing anodic bonding is to first stabilize the temperature at a process value prior to applying the voltage (voltage shock method). However, this approach is limited when bonding cavities of sub-micron depth, as the initial electrostatic pressure over the cavity is high enough for the membranes to attract and bond. The temperature ramp method , an alternative to voltage shock method, applies the voltage previous to ramping of the temperature to process value, thus prohibiting the voltage drop over the shallow cavities from high initial values as most of the applied voltage V will drop in the bulk glass. As the temperature has reached process value, the depletion layer has begun to form and the voltage drop in the cavities does not reach as high values as in the case of the voltage shock method. Utilizing this method, cavities of extreme height-to-width ratio (300 nm deep and 500 _m wide) were successfully manufactured [17] and coupled to an optical fiber in order to measure transient pressures [20].

3.9.3 Silicon-thickness, doping and resistivity

The thickness of the silicon wafer has to be considered since some degree of stress will remain in the wafer after bonding and cause warp and bow which to some extent can be compensated for by wafer thickness considerations [21]. Thin wafers are more flexible than thick ones and more easily overcome irregularities [22]. This is especially the case in bonding silicon to a fiber end face with a shallow cavity (<1 _m) because we use ultra-thin silicon of thickness 4-10 _m. Using ultra-thin is favorable in that bonding is possible even for mechanically polished fiber end faces with average roughness value as high as ~10 nm.

The doping of silicon does not have to be taken into consideration when bonding at temperatures above 350 ^{0}C as silicon then becomes degenerate and acts like a metal as far as anodic bonding is concerned, i.e. an equipotential is established across the wafer as soon as the voltage is applied. When bonding at temperatures below 300 ^{0}C or when using the temperature ramp method [17], a doping dependent depletion layer is formed in the silicon.

3.9.4 Surface morphology

One of the major advantages of anodic bonding is that the process is relatively insensitive to surface roughness compared to the demand put forth by silicon-to-silicon direct bonding. For silicon-to-silicon direct bonding to occur, a microscopic surface roughness greater than 5 will result in void formation at the wafer interface. The corresponding value of maximum surface roughness for successful anodic bonding is in the _m range [10] (i.e. a factor 2000) which renders possible bonding of wafers with deteriorated surface polish due to prior processing, or with deposited metal conductors in the bonding surface [15]. The above account of surface roughness requirements for anodic bonding was evident in our experiments on bonding of silicon to fiber.

3.9.5 Electrode Configuration

The electrode configuration on the anode side is of little importance due to the relatively high electrical conductivity of silicon and metals at the bonding temperatures used. The electrode configuration on the cathode side is of major importance as it influences the electric field applied over the glass and thus effect the ion conduction. The advantage of a pin cathode is that the bond wave propagates radially from a single point of contact and thus prevents air from being trapped as voids in the bond interface. Using a plate cathode on the other hand renders possible bonding at considerably lower process parameters, thus minimizing problems of residual thermal strain, plastic deformation, and sealed cavities. It is shown that reliable bonds can be achieved at 280 C using a plate electrode [17]. Plaza *et al* has shown that a star-shaped electrode combines the advantages of a point and plate electrode [23].

In this work, the electrode configuration for cathode is different from all of the above-described configurations because the cathode electrode is a metal-coated fiber (Figure 3.13). It was found, in this case, that the electrode configuration did not matter as long as the uncoated length of fiber was made shorter than 2 mm (Figure 3.13) at temperature of 400 ^{0}C and voltage of 1000 V. Further, bonding silicon to fiber involves only a very small area (fiber diameter ≤ 400 _m); as a result many complications observed in wafer-to-wafer bonding were not observed in silicon to fiber bonding.

3.9.6 Choice of glass for anodic bonding

The most common glass used for anodic bonding is Pyrex (corning #7740, Hoya SD-2 (Hoya) and Tempax (Schott #8330). These inorganic borosilicate glasses all contain around 4% sodium; other metal ions in the glass are lithium, potassium, calcium, and aluminum. Most alkali-containing glasses behave at elevated temperatures like solid electrolytes. This property of glass is a key mechanism for anodic bonding. Bonding to silicon patterned by SiO_2 usually requires glass with a high volume resistivity to avoid electrical discharge in shallow cavities [24]. Schott AF37 is such a glass, which high volume resistivity is due to its low content of alkali ions (<0.3 %). When fabricating devices extremely sensitive to residual strain such as anodically bonded optical pressure sensors, the thermal expansion match of glass to silicon is of great importance [17]. Optical devices for high-temperature applications require glass of low alkali content [24]. Low viscosity glass enables bonding of materials of slightly different thermal expansion [25].

3.9.7 Preliminary bonding test results

There are several bonding techniques that are commonly used in MEMS for bonding glass and silicon wafers, namely anodic bonding [26], hydrophilic fusion bonding [27], hydrophobic fusion, and many other methods combining the above [28-29]. Fabrication of a pressure sensor required bonding of a thin silicon diaphragm on to a fiber end face. We envisioned that the anodic bonding mechanism could be used for bonding silicon to optical fibers since optical fibers are made out of glass. Optical fibers from several manufacturers were tested for anodic bonding in the range of temperatures (200-500 ^{0}C) and voltages (700-1500 Volts). It is observed that at temperatures above 300 ^{0}C, weak bonding took place regardless of the voltage applied. We identified this as weak-thermo-compression bonding [30] that exists in many material-pairs at

such elevated temperatures when they are in contact and have smooth surfaces. Strength of bonding between the fiber end face and silicon in this case was identified to be too small for hermetic sealing of the cavity. Further, these preliminary bonding experiments suggested that telecommunication fibers made out of pure silica likely contained too few alkali ions for the anodic bonding mechanism.

Fusion or direct bonding such as hydrophilic fusion bonding does not require applied voltages, elevated temperatures for the initial contact, or that either material be an insulator. Bonding occurs primarily through chemical reactions between species, such as hydroxyl groups for silicon, on the two surfaces. The two materials are mated together at room temperature and then annealed at high temperatures around 1100 ¡C to increase the bond strength. Lord Raleigh first published an investigation of the adherence of pieces of silica at room temperature in 1936. Among his observations were that the surfaces must be clean and smooth, that thinner pieces are easier to bond due to elastic deformation, which allowed the surfaces to conform to each other, and that temperature differences are detrimental to bonding due to thermal expansion. Fusion bonding has since been used in fabricating many MEMS devices including pressure sensors [31].

Hydrophilic Fusion Bonding [27], though used in some MEMS applications, was considered not suitable in bonding silicon to fiber end face. As explained before, hydrophilic fusion bonding being a direct bonding method requires that the bonding surfaces be extremely smooth. Because fibers undergo a mechanical polishing step which make the surfaces carry an average roughness of 8 nm, the possibility of fusion bonding as an alternate bonding technique was ruled out.

3.9.8 Anodic Bonding of Silicon on Borosilicate Glass Fiber Tips

The experimental set up for bonding of silicon to fiber is shown in Figure 3.13. The ultra-thin silicon piece to be bonded was placed on a clean thick-silicon wafer placed on a hot plate. Borosilicate glass fiber was coated with silver paint for electrical connection except at the end where bonding is supposed to take place. The uncoated length was made to be ~ 1mm; it was observed that this length be made less than 2 mm for creating enough electric field for a voltage of 1000 V to be applied between the fiber and silicon. The fiber was mounted on a metal holder so that metal-coated part of fiber was in contact with this holder (negative dc voltage of 1000 V applied to this holder (or fiber)). The fiber with its holder was fixed to a tilted stage coupled with XYZ-stage, which has 5- degrees of freedom of motion; this arrangement allowed the fiber to be brought down to silicon so that its end face is entirely in contact with silicon. A stereomicroscope was aided in observing that the fiber is held approximately vertically so that the above requirement is met. The accuracy of the above requirement is low because of the strong electrostatic field (typically 500 V/mm) that is generated as a result of the depletion layer at the interface,

The temperature ramp method , described above, was adopted as opposed to the voltage shock method , since the fiber end face involved cavities of extreme height-to-width ratio (640 nm deep and 150 _m diameter). This method applied the voltage of 1000 V previous to ramping of the temperature to process value of 400 ^{0}C, thus prohibiting the voltage drop over the shallow cavities from high initial values as most of the applied voltage V would drop in the bulk glass. After the temperature had reached process value of 400 ^{0}C, the voltage was continued to apply for another 3 minutes before both voltage and temperature were turned off. Pictures of bonded silicon on fiber end face are shown in Figure 3.14. Figure 3.14(a) shows a case where thin

silicon is undesirably bonded to the bottom of the cavity from the voltage shock method, while Figure 3.14(b) shows a case where it is not bonded to the bottom as a result from the temperature ramp method . Both cases are for 400 _m diameter fiber, 7 _m thick silicon, and at above mentioned anodic bonding parameters.

3.10 Fabrication of Linear Pressure Sensor Arrays

Fabrication of a linear pressure sensor array is similar to that of single sensor. In this effort, we have tried to fabricate six identical sensors that extend linearly over a length of 1.5 cm each separated by nearly 3 mm. Six fibers were mounted on an aluminum fixture using ceramic epoxy (Section 4.3, Figure 4.9). All fabrication steps were done to all six fibers simultaneously. All six sensors were designed to have the following sensor parameters:

Cavity depth = 0.640 _m

Cavity diameter = 180 _m

Silicon diaphragm thickness = 3.4 _m

It was important to see how closely each of these sensors was identical as far as above sensor parameters were concerned. Cavity depths for these sensors were not measured, but etching profile measurements indicate the cavity depth could vary by approximately ±5%. Cavity diameter for each of the sensors in the array was measured using an optical microscope with an uncertainty of ±1.5 _m. The cavity diameters for the six sensors were 151, 150, 150, 150, 150, 150 _m. This indicates that the fabrication of cavities on fiber end face can be done to an accuracy of < 1%. The thickness of ultra-thin silicon wafer piece used in this experiment was 7 _m; we used a piece of silicon from an area where the measured the thickness was constant within ±1.0 _m. The temperature ramp method , described above in section 3.9.8, was adopted

in bonding silicon to the fiber end face. The other side of each fiber was connectorized with SMA connectors for connecting fiber sensors to the measurement system.

3.11 Fabrication of Thin-film Temperature Sensor

The fabrication of uncapped temperature sensor only involved bonding a piece of ultra-thin silicon onto a fiber end face. Bonding was done using the voltage shock method (anodic bonding) explained in section 3.9.2. Therefore, the fabrication of uncapped temperature sensor is not further discussed here. Encapsulated (capped) sensor (Figure 2.9 in chapter 2) has two oxidant-barrier layers deposited on one side of silicon: low-pressure chemical vapor deposited (LPCVD) silicon nitride layer (106 nm design thickness) and an electron-beam evaporated aluminum layer (1 _m thickness). The reasons for choosing the above layer materials and the design considerations are described in chapter 2. In fabricating the encapsulated temperature sensor, we first deposited the above layers on silicon in the above order and then anodically bonded the multi-layered silicon onto the fiber end face. Bonding was carried out as shown in Figure 3.15 at a temperature of 400 ^{0}C and at a voltage of 1000 V. The voltage was applied between the metal-coated fiber and the uncoated surface of silicon (figure 3.15).

The summary of LPCVD deposition process of silicon nitride was as follows:

Design Si_4N_3 film thickness =106 nm;

Temperature: 770 ^{0}C;

Pressure: 300 mTorr;

Gases and their flow rate in sccm: $SiCl_2H_2$ (dichlorosilane), 25;

NH_3 (Ammonia), 100;

Deposition rate: 57 /min;

Deposition time: 19 minutes.

Following silicon nitride deposition, 1 μm thick layer of aluminum was e-beam deposited at chamber pressure of 10^{-7} Torr and at an e-beam current of 55 mA (Deposition rate: 0.2 micron/min).

Spectroscopic ellipsometry was used in determining the thickness of silicon nitride layer. It is a nondestructive optical technique typically used to determine the optical properties of substrates and thin films. This experimental method is based on measuring the polarization ellipse of a light beam reflected off a sample at a given angle. The angle of incidence on our ellipsometer can be varied from 55 to 75 degrees in 5-degree increments. Using a 75W Xenon arc lamp source, the ellipsometer has a wavelength range from 250 nm to 1000 nm.

A monochromatic light beam of known polarization is reflected off the sample at a given angle of incidence altering both the intensity and polarization state of the beam. A polarization analyzer and photodetector are used to measure ϕ and δ angles as a function of incident angle and wavelength. These measured parameters are defined as

$$Tan(\phi)Exp(j\delta)=\frac{R_p}{R_s}$$

where *Rp* and *Rs* are the pseudo-Fresnel reflection coefficients of the sample, with p denoting the direction of the plane of incidence and s the direction perpendicular to the incident plane.

From this data, the complex index of refraction and film thickness can be determined using a computer model fit. First, an initial model of the sample is created. Then, using a nonlinear regression technique, the model parameters are varied to fit the experimental data.

Experimental data (Figure 3.16) of spectral ellipsometer is as follows:

Mean Square Error = 1.253

Thickness = 105.56–0.263

Real part of refractive index = 1.9839–0.00082

Imaginary part of refractive index= 0.018849–0.000228.

After several processing runs, we obtained the film with above set of optical properties where the thickness and refractive index was shifted minimally from the expected values (the design thickness by nearly 1 nm, and the refractive index shifted by 0.04). The above shifts can be attributed to the change in actual temperature at which the deposition was done from the specified temperature.

3.12 Concluding Remarks

A simple micromachining process compatible with MEMS was developed in fabricating a novel pressure sensor on an optical fiber. The light-guiding capability of optical fibers and the photoresist-exposing capability of a low-wavelength Argon ion laser (λ=457.9) laser were utilized in this process. Commercially available ultra-thin silicon (4-7 μm) wafers were used avoiding an extra step of thinning of silicon. A disadvantage associated with applying photoresist onto such a small area as an optical fiber end face was the inability to control the thickness of the photoresist. In this case we have been able to minimize the effect of this problem by using thinned photoresist. However, the overall accuracy of the diameter of circular cavities on fiber end faces has been less than 1%. Atomic force microscopy (AFM) accurately determined the wet-etched cavity depth and its bottom profile on fiber end faces allowing us to determine the etch rate of borosilicate glass fibers in buffered hydrofluoric acid. Bonding of silicon to fiber end face, the last step in the fabrication of pressure sensor, was done successfully by employing anodic bonding method. Following successful fabrication of a single pressure sensor, an array of six identical sensors was fabricated simultaneously.

The success of bonding silicon to fiber end faces led to the fabrication of thin film temperature sensor. The temperature sensor was fabricated by bonding 4 μm thick silicon onto fiber end face. An encapsulation scheme for the temperature sensor was proposed, namely aluminum coated silicon nitride (Al/Si_3N_4). The uncoated side of silicon was bonded to fiber end face using the anodic bonding method.

The bonding of silicon to fiber end face can be extended to fabrication of other MEMS based micro-optic devices where fiber optic interrogation is advantageous.

3.13 References

[1] S. Tatic, etal, Bonding quality characterization of silicon-glass anodic bonding , Sensors & Actuators, pp.223-227, 1997.

[2] Guide to Connectorization ans Polishing Optical Fibers, ThorLabs Inc., 1997.

[3] Gerd Keiser,Optical Fiber Communications, third edition, McGraw-Hill International Editions, International editions 2000.

[4] T. Carriere, B. Agius, I. Vickridge, J. Siejka, and P. Alnot, Characterization of silicon nitride films deposited on GaAs by RF Magnetron Cathodic Sputtering , J. Electrochem. Soc. 137, pp. 1582, 1990.

[5] S.A. Campbell, The Science and Engineering of Microelectronic Fabrication , Oxford University Press, New York, 1996.

[6] J. Lasky, Bonding of silicon to silicon , Applied Physics Letters, 48(1), pp 78, 1986.

[7] S.K. Ghandi, VLSI Fabrication Principles, New York: Wiley, Chapter 9,1983.

[8] J. S. Judge, A study of the dissolution of SiO_2 in Acidic Fluoride Solutions , J. Electrochemical Soc., Vol. 118, no. 11, pp. 1772-1775, November 1971.

[9] H. Kikyuma, N. Miki, K. Saka, J. Takano, I. Kawanabe, M. Miyashita, and T. Ohmi, Principles of Wet chemical Processing in ULSI microfabrication , IEEE Trans. Semicon. Manufact., vol. 4, no. 1, pp. 26-35, February 1991.

[10] W. R. Runyan and K.E. Bean, Semiconductor Integrated Circuit Processing Technology , Reading, MA: Addison-Wesley, 1990.

[11] T. Anthony, Anodic bonding of imperfect surfaces , Journal of Applied Physics, 54, pp 2419-2428, 1983.

[12] K. R. Farmer, D. V. Ivanov, W. Peng, M. Beggans Optical pressure sensor head fabrication using ultra-thin silicon wafer bonding, Proc. 1999 SPIE International Symposium on Design, Test and Microfabrication of MEMS/MOEMS .

[13] G. Wallis, D. Poerrantz, Field assisted glass-metal sealing , J. Appl. Phys., 40(10), pp. 3946,1969.

[14] P. Nitzsche, etal, Ion drift process in Pyrex-type alkali-borosilicate glass during anodic bonding , J. Electrochem. Soc., 145(5), pp 1755-1761, 1998.

[15] D. Carlson, K. Hang, and G. Stockdale, Ion depletion, of glass at a blocking anode II , J. Am. Ceram. Soc., 57(7), pp. 295-300, 1974.

[16] T. Corman, P. Enoksson, and G. Stemme, Low-pressure-encapsulated resonant structures with integrated electrodes for electrostatic excitation and capacitive sensors , Sensors and Actuators, A(66), pp. 160-166, 1998.

[17] H. Engelke, and M. Harz, Curvature changing or flattening of anodically bonded silicon and borosilicate glass , Sensors and Actuators, A 55, pp. 201-209, 1996.

[18] A. Richard, K. Sundin, and Y. Backlund, Low temperature anodic bonding of a sub-micrometer fabry-perot cavity , Fifth Int. Symp . On Semiconductor Wafer Bonding, Honolulu, Hawai, 1999.

[19] J. Go, Y. Cho, Experimental evaluation of anodic bonding process based on the Taguchi analysis of interfacial ftracture toughness, Sensors & Actuators, 73, pp.52-57, 1999.

[20] A. Gozma, Characterization of the electrostatic bonding od silicon and Pyrex glass , J. Electromech. Microeng., 5, pp. 98-102, 1995.

[21] K. Sundin, et al, Fabry-Perot cavity sensor system with compensation for fiber attenuation and sensor temperature variation , accepted for presentation at North. Opt. 2000, Uppsala, Sweden, 2000.

[22] A. Cozma, Characterization and optimization of electrostatic bonding of wafers , Ph.D. thesis, Department of Electrotechnie, Katholieke Universiteit, Leuven:Leuven, 1993/1994.

[23] K. Ljungberg, Phenomenon of silicon wafer bonding Solid State Electronics, Uppsala:Uppsala, pp. 59, 1995.

[24] J. Plaza, J. Esteve, and E. Lora-Tamayo, Nandestructive anodic bonding test , J. Electrochem. Soc. 144(5), pp. 108-110, 1997.

[25] T. Rogers, J. Kowal, Selection of glass, anodic bonding conditions and material compatibility for silicon glass capacitive sensors , Sensors and Actuators, A 46-47, pp. 113-120, 1995.

[26] M. Esashi etal, Low-temperature silicon-to-silicon anodic bonding with intermediate low melting point glass , Sensors & Actuators, A21-A23,pp 31-934, 1990.

[27] Y. Kanda, K. Matsuda, C. Murayama, and J. Sugaya, The Mechanism of Field Assisted Silicon-Glass Bonding , Sensors & Actuators, Vol. A21, pp. 939-943, 1990.

[28] Zhi-Xiong Xiao, Silicon--glass wafer bonding with silicon hydrophilic fusion bonding technology , Sensors and Actuators A: Physical, ISSN : 0924-4247 Vol./ Iss. : 72 / 1, pp. 46-48, 1999.

[29] K Tanaka,E Takata, K Ohwada, Anodic bonding of lead zirconate titanate ceramics to silicon with intermediate glass layer , Sensors and Actuators A - Physical 69: 2 Instrumentation & Measurement, 29, pp199-203, August 1998.

[30] Lehmann, V., Ong,. I.W.K., and G sele, U., "Semiconductor Wafer Bonding" Advanced Materials, 8, pp. 372-374,1990.

[31] P. Barth, "Silicon fusion bonding for fabrication of sensors, actuators and microstructures," Transducers 89, Proceedings of the 5th International Conference on Solid-State Sensors and Actuators and Eurosensors III, 2, pp. 919-926, June 1990.

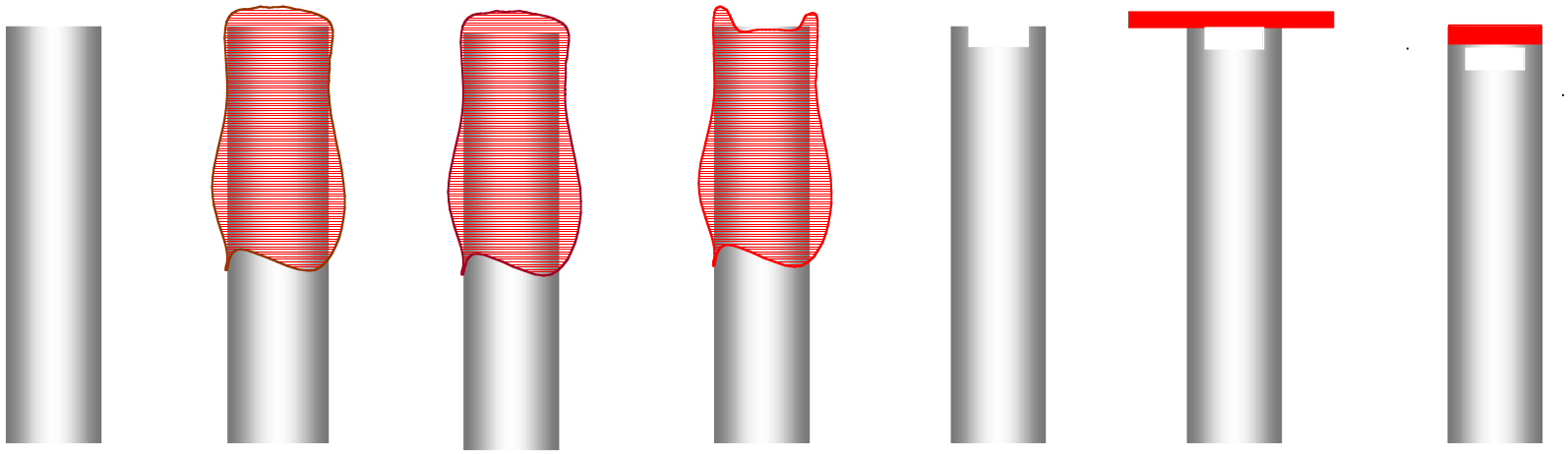

Figure 3.1 Fabrication steps in order (left to right), cleaved/polished fiber, photoresist coated fiber, blue light coupled fiber, patterned fiber, cavity on fiber, silicon bonded fiber, pressure sensor on fiber.

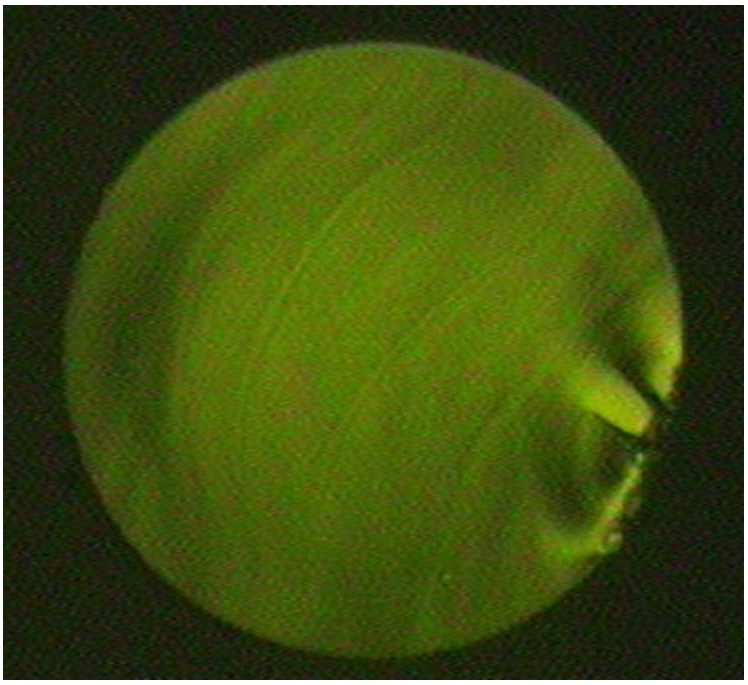

Figure 3.2 The fiber end faces of the cleaved fibers are not uniformly flat across the fiber end face

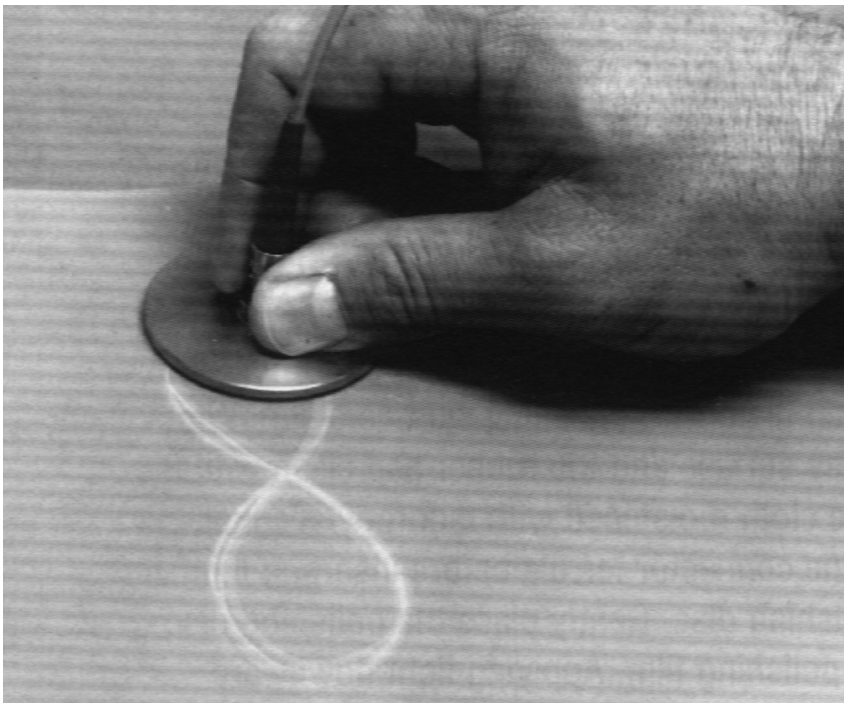

Figure 3.3 Fiber Polishing on polishing paper

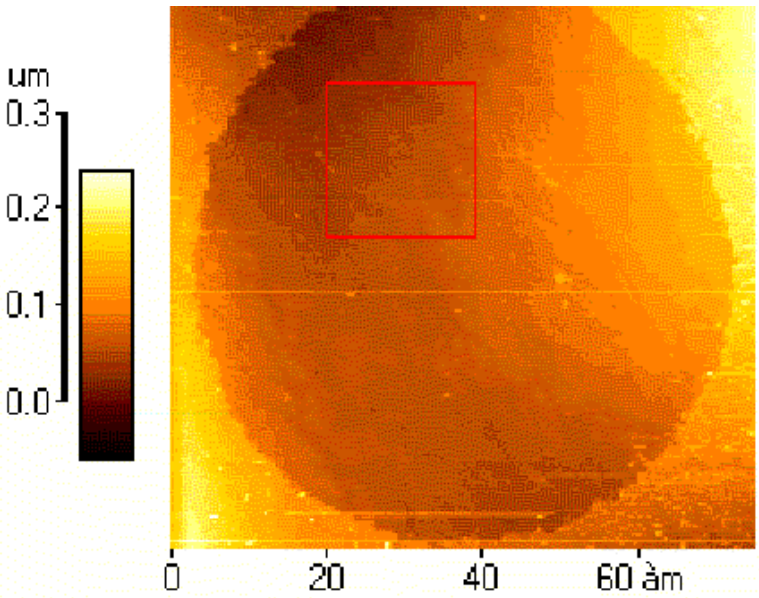

Region	Rp-v	Rms rough	Ave rough	Mean Ht	Surface area
[A]	834 Å	123 Å	103 Å	528 Å	396.9 à²

Figure 3.4 AFM topography measurements of the cavity bottom. Surface roughness numbers are of the same order as those of the initial end face and are low enough to treat the cavity bottom as optical polished.

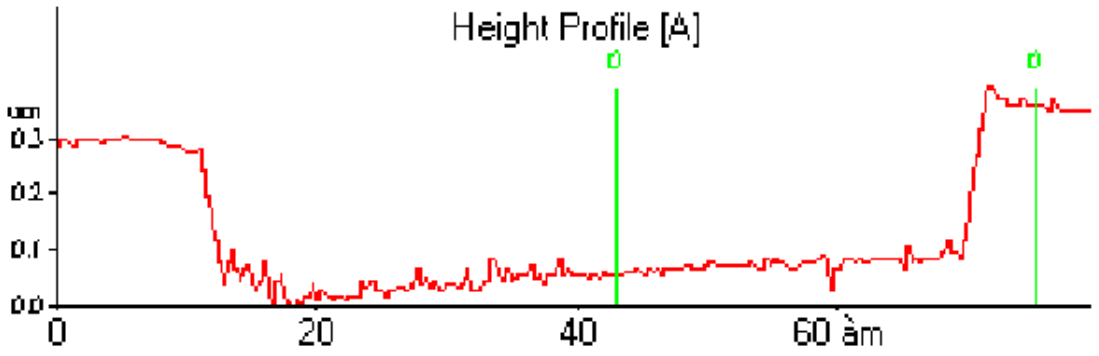

Figure 3.5 AFM line profile of an 80-_m-diameter cavity. The line profile of a cavity was used in determining the cavity depth; this method was employed in determining the etch rate for borosilicate glass fibers.

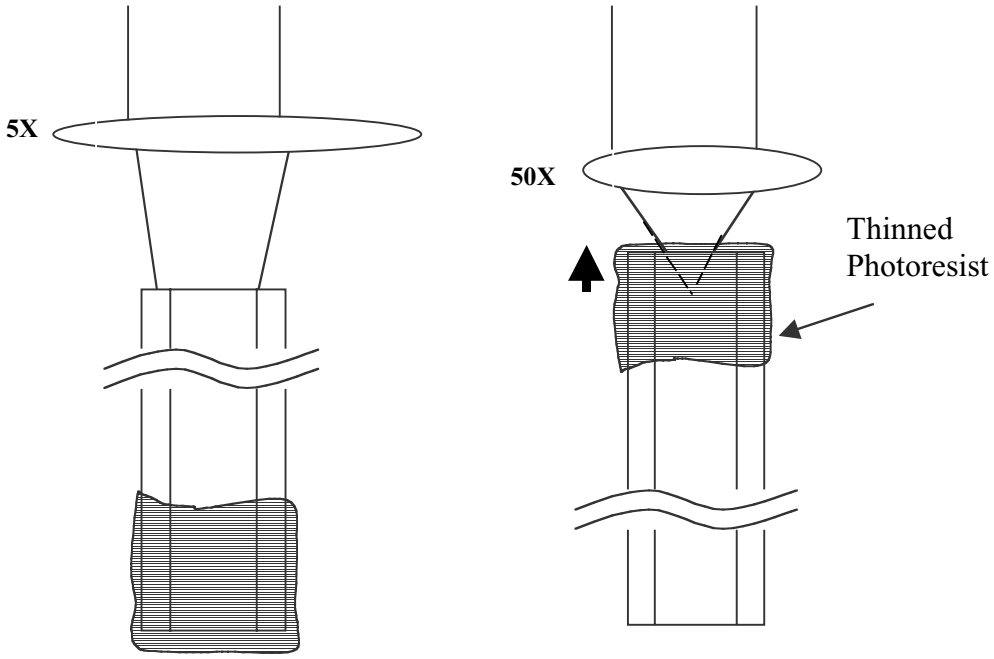

Figure 3.6 Schematics of two photoresist exposure techniques. Both of these techniques used blue Argon ion laser light (λ = 457.9 nm) for exposing photoresist. The first technique (left) involves coupling of light into the opposite fiber end using a low magnification microscope objective (5X) so that the focused laser beam diameter is comparable to the core diameter. The second technique (right) simply directs laser light onto the photoresist-coated fiber end face using a high magnification objective (50X). In this case, the fiber is positioned away from the beam focal point by an amount that corresponds to the required beam diameter

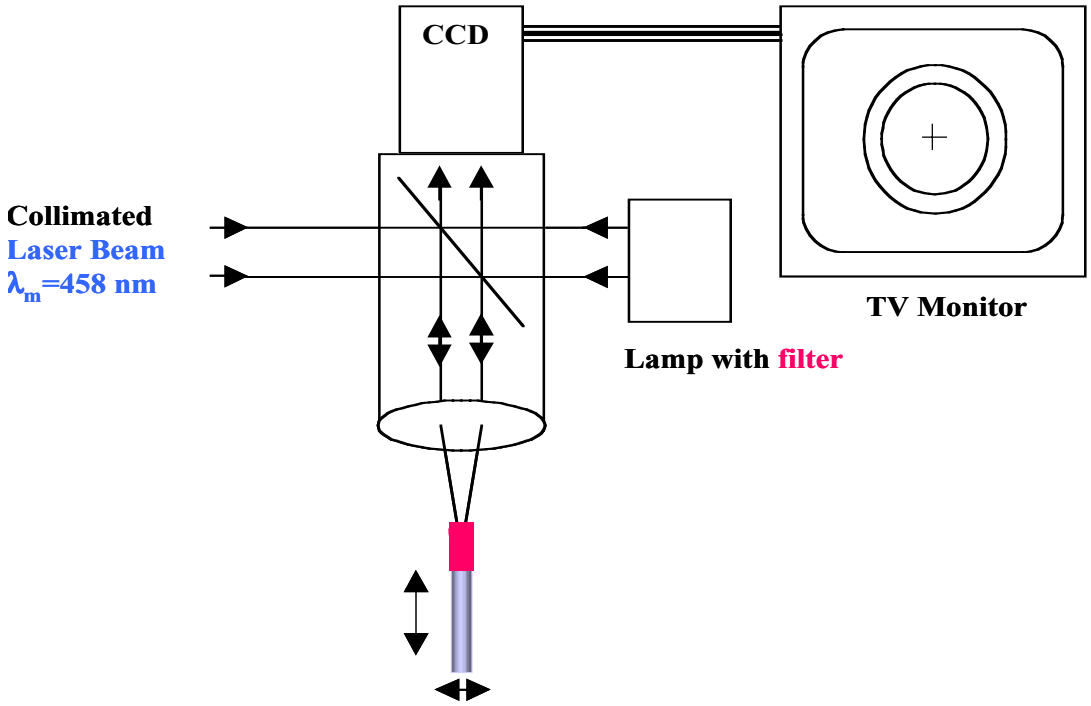

Figure 3.7 Experimental set up for photoresist coated fiber consisted of a red light lamp coupled to the microscope, CCD camera mounted to the microscope, and a TV monitor. The position where the laser beam would be focused was marked (as a + in the middle of the screen) on the TV screen. The fiber was aligned so that its center coincided with this point.

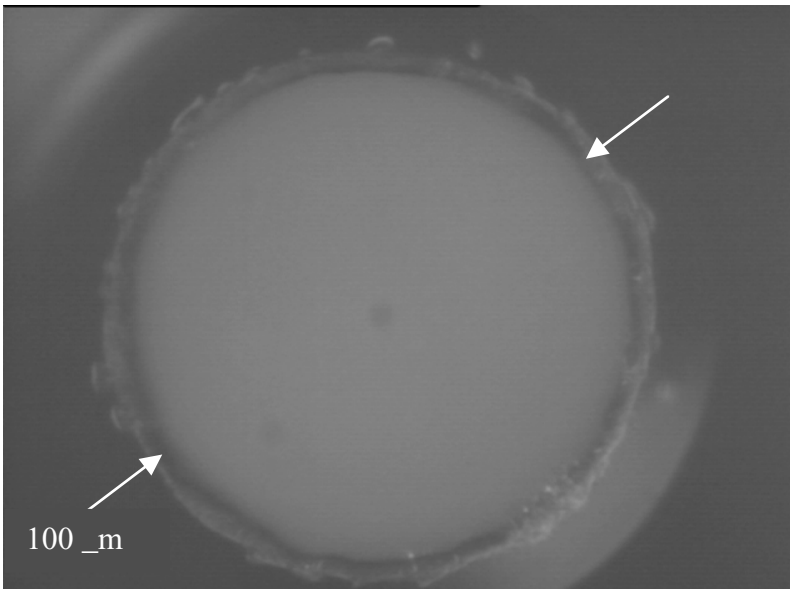

Figure 3.8 A picture showing a patterned Corning MM fiber (100/140 _m) where a circular area of PR is removed. The removed area has a diameter of 100 _m equal to that of the core of the fiber.

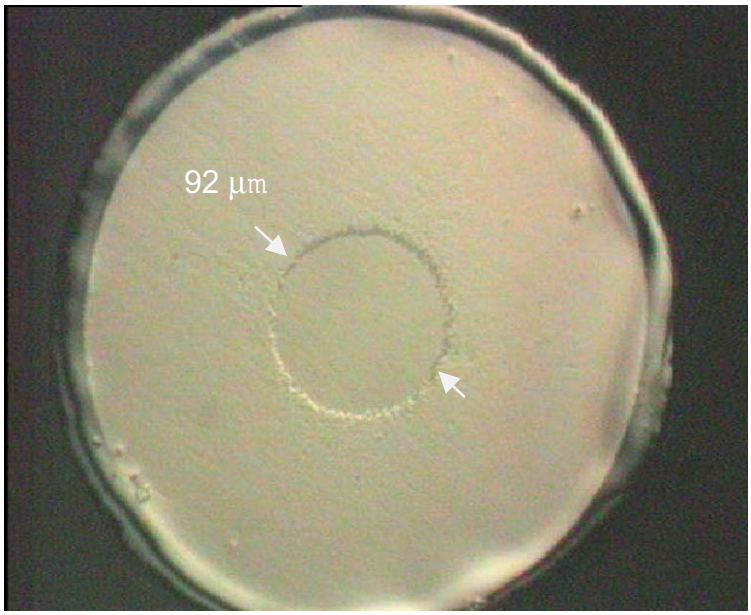

Figure 3.9 A picture of a patterned borosilicate glass fiber the second exposure technique where blue light is simply directed onto the photoresist-coated fiber end face using a high magnification objective (50X). A circular area of PR is removed. The removed area has a diameter of 92 _m.

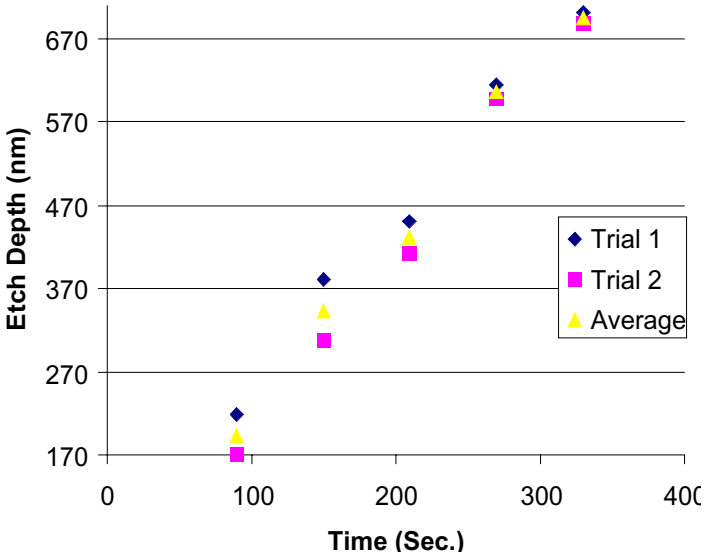

Figure 3.10 Measured etch depths for a patterned fiber end face (borosilicate glass) with a cavity of 100 _m diameter at different etching times. The rate was calculated to be 120 nm/min. The etching solution was NH4F: HF≡12:1.

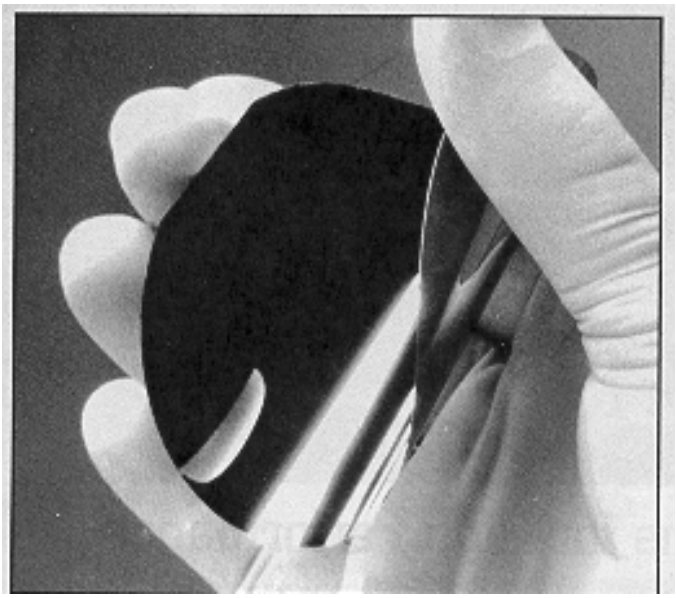

Figure 3.11 A 10-_m single crystal silicon membrane manufactured at the Virginia Semiconductors Inc. The picture exhibits the flexibility of these ultra-thin silicon (membranes) wafers.

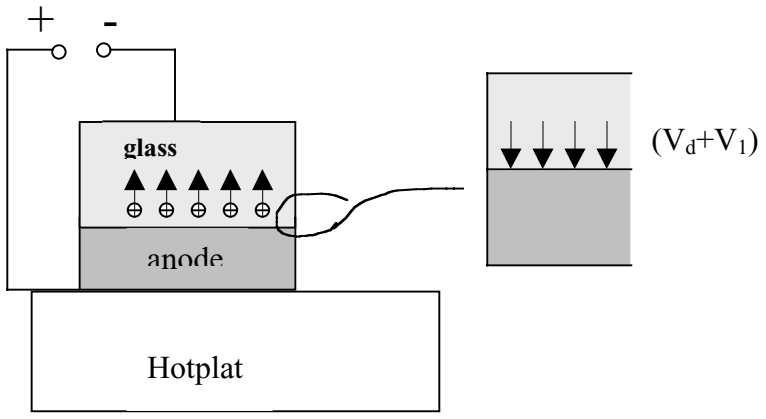

Figure 3.12 The set-up for anodic bonding. Charges are transported to the electrodes as a dc-field is applied. The cathode is contacted to the glass wafer. The metallic wafer at the bonding interface serves as the anode.

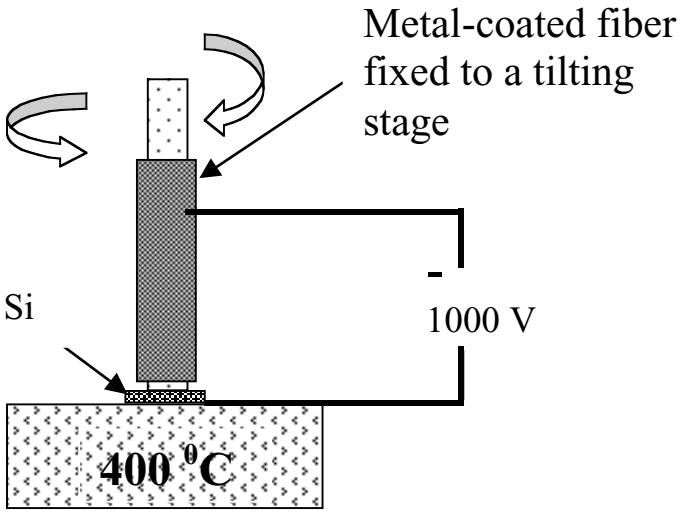

Figure 3.13 The experimental set up for bonding of silicon to fiber.

(a)

(b)

Figure 3.14 Ultra-thin silicon anodically bonded to a fiber end face. (a) thin silicon is undesirably bonded to the bottom of the cavity from the voltage shock method, while (b) silicon is not bonded to the bottom as a result from the temperature ramp method . Both cases are for 400 _m diameter fibers, 7 _m thick silicon, and at anodic bonding conditions of temperature 400 ^{0}C and voltage 1000V.

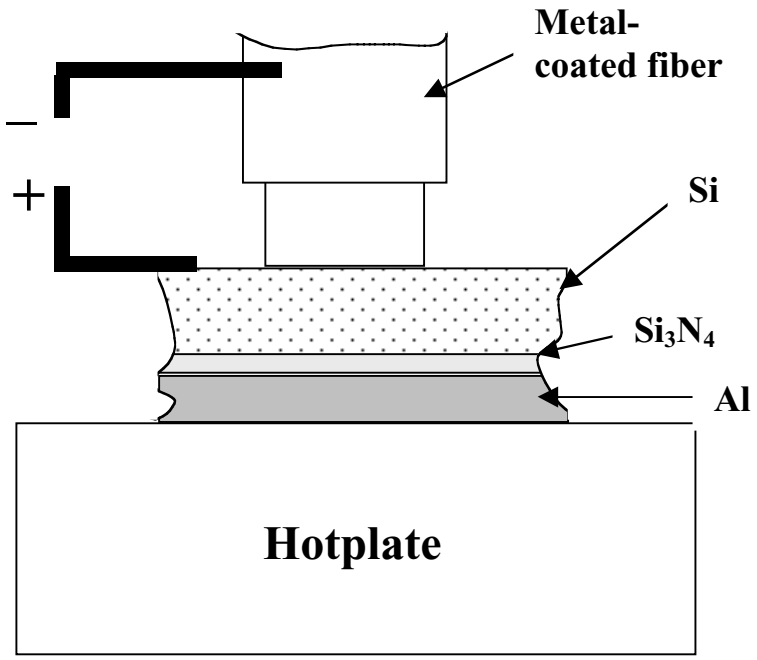

Figure 3.15 Anodic bonding set-up of multi-layered silicon onto the fiber end face (not to scale). Bonding was carried out at a temperature of 400 ^{0}C and at a voltage of 1000 V. The voltage was applied between the metal-coated fiber and the uncoated side of silicon.

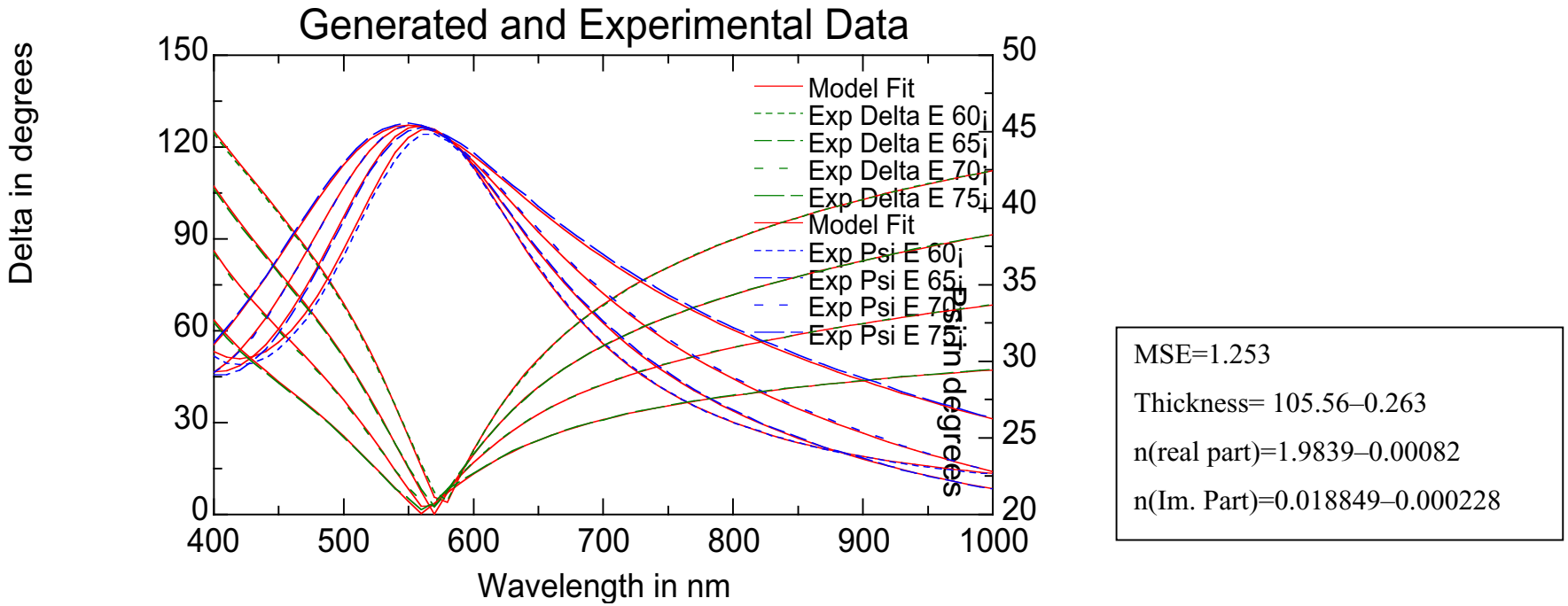

Figure 3.16 Thickness and refractive index measurements of silicon nitride on silicon using spectral ellipsometer.

4.0 Characterization of Sensors

4.1 Introduction

The creation of optical fibers with a small extinction coefficient has encouraged the development of sensors operated entirely by optical signals and requiring no external electrical supplies. These sensors are often called passive sensors. The passive sensors have been developed to date usually as intensity-encoded sensors and therefore they require special efforts such as a reference channel in order to minimize the influences of long-term aging of source characteristics as well as short-term fluctuations of optical power loss in the cable on the accuracy of measurements. Using frequency as the information parameter for a quantity to be measured presents advantages such as transmission through extended systems and over large distances without error, and simplicity in digitizing by counting its periods. And wavelength-encoded measurements also present these advantages, but more importantly, they are link-insensitive; thus, more suitable for harsh environment applications. In this section we present a review of fiber optic sensor interrogation schemes followed by the results of pressure and temperature sensors.

Fiber optic pressure and temperature sensors were fabricated using the design and processes described in chapters 2 and 3 respectively. Two single pressure sensors, and two temperature sensors were fabricated and tested by reflectometry. An array of six identical linearly spaced pressure sensors were also fabricated and tested. Pressure measurements were made over the 14 to 80 psi range while temperature measurements were made over the 23 to 300 ^{0}C range. Temperature sensors were tested both with and without encapsulation.

4.2 Review of Sensor Interrogation Schemes

A major problem faced when designing a fiber optic sensor is that, unlike electrical wires, fiber optic transmission can vary by 10% with large temperature changes and remates of optical fiber connectors [1] . Since constant fiber transmission cannot be relied upon, researchers have pursued more complicated sensor schemes, which do not count on constant link transmissivity. Such schemes may also make the sensor independent of fluctuations in source brightness.

Passive optic sensors suited for field use must meet a common set of requirements.

(1) Link independence: Insensitivity to variation in transmission through the fibers.

(2) Temperature insensitivity: The accuracy of the sensor will be no better than the uncorrectable drift in scale factor and zero experienced in the sensor environment.

(3) No ambiguity problem: When interrogated by a fixed wavelength source, an interferometric sensor s output is periodic with measurand (Figure 4.1). Movement of the phase through a minima or maxima creates an ambiguity. One solution is to restrict the range. Other techniques, such as sweeping the source wavelength, monitoring transmittance at multiple wavelengths, or designing the device to produce simultaneous cosine-sine outputs can allow phase tracking over more than π radians phase change.

(4) Existence of zero: Phase tracking techniques can permit following an interferometer's phase change over an extremum. However, when the source is first activated, and after a power interruption, the measurand may have to be set to a known state to permit determination of the correct fringe order. In such a case, the sensor is said to lack a zero. Once the sensor has been initialized, phase tracking can enable determination of the measurand wherever it may venture. It is desirable that the sensor possesses a zero to eliminate initialization procedure.

In addition to the above considerations, there are several other issues, although of lesser importance, those are worthy of consideration:

(1) Does the source have to be temperature stabilized to keep its wavelength from drifting?

(2) What kind of fibers link the sensor head, and how many?

(3) How complex is extracting (demodulating) the measurement from the sensor output?

(4) What is the size of the sensor head and fiber diameter?

(5) Can the head or demodulation electronics be replaced without recalibrating?

In intensity sensors, the transmission between fibers is controlled by the measurand. Although interferometric sensors may be used in this manner, intensity sensors typically do not take advantage of techniques such as spectral encoding or two-wavelength ratioing. Unless other techniques such as four-fiber compensation [2] are employed, the sensor will not be link insensitive. Nevertheless, their simplicity, ease of demodulation, output monotonicity, and unusually high temperature immunity makes them attractive.

A typical Fabry-Perot pressure sensor is considered as an example in explaining above considerations further. A pressure sensor head, which is compact and often described in the literature, consists of a thick slab, a spacer layer, and a thin diaphragm cap arranged to form a Fabry-Perot (F-P) cavity (Figure 4.2). The head is attached to the tip of a fiber into which light is coupled, and light reflected back from the head is measured (Figure 4.3). If the absolute intensity of light reflected is measured, a detector may monitor the source brightness. For ease of connectorization, multimode fibers are typically used.

An important design consideration is whether the interferometer's optical path length (OPL), which is twice the mirror spacing in the Fabry-Perot cavity, is greater than the source coherence length L_{coh}. The coherence length may be calculated from the spectral line width ($\breve{}\,\lambda$)

$$coh = \frac{\lambda_0^2}{\Delta\lambda} \quad , \tag{4.1.1}$$

where λ_0 is the wavelength at the peak spectral power density. As the cavity mirror spacing is increased from 0˚μm, the reflectance will periodically vary between a minima and a maxima. As the separation increases, approaching $L_{coh}/2$, the amount of variation will diminish and monotonically approach 0. For cavity lengths significantly greater than $L_{coh}/2$, the power reflected will be independent of cavity length. In this case, the reflectance minima are spaced closely enough in wavelength that the separation between them is less than the line width of the source. Wavelengths not reflected by the cavity are missing from the envelope emitted by the source (Figure 4.4).

Various techniques have been have been proposed to interrogate this sensor head. A good summary of review of various measurement techniques can be found in the reference [3]. Lieberman and Blonder [4] propose using a LED to measure a 0.5˚μm cavity and monitoring the coherently reflected intensity. This technique, while simple to demodulate, is not link independent and the cavity reflectance will depend on the wavelength emitted by the LED, which will vary 0.3˚nm/ ^{0}C [5] . In addition, reflection from connectors will be indistinguishable from that of the head.

Saaski *et al*. [6] and Dakin *et al*. [7] solve the link sensitivity problem by calculating the diaphragm deflection, and thus pressure, from the intensity ratio of two reflected wavelengths. Saaski *et al*. used a single LED source with a 1 to 2˚μm cavity spacing and split the reflected light into two wavelengths, which were separately monitored. Since effects which alter the fiber transmissivity equally at both ends of the LED spectrum will not affect this ratio, the technique is link insensitive.

Although ratioing the intensity of the two wavelengths returned from the sensor head can reduce link sensitivity, connector back reflection will add equally to the ratio's numerator and denominator, altering it. In addition, while the source monitor intensity and back reflected head signals emerge from different fibers, some cross coupling can occur. Dakin *et al*. [7] reduced this problem by connecting their head to the coupler of figure.˚4.5 via 1.1˚km of optical fiber and pulsing the LED's at a frequency (23˚kHz) which would place the light pulses reflected from the head electrically 90^0 out of phase both from cross coupled signal used to monitor the LED and from reflections from connectors close to the coupler. Processing relying on this phase shift employing synchronous demodulation, the technique used in lock-in amplifiers, can remove the cross coupled signals. Rejection of light reflected from connectors placed near the electronics (far from the head) will also occur.

Diaphragm deflections in devices presented so far are restricted to $\lambda_0/4$ to prevent ambiguity and ensure a zero, regardless of what movement may be permitted from diaphragm breakage considerations. Temperature changes will cause variations in cavity separation, so it is desirable to permit as large a deflection as possible. Halg [8] has described a sensor configuration, which consists of a F-P head with a 3˚µm cavity spacing ($>^{\circ}L_{coh}/2$), which may be fed by a single multimode optical fiber. An LED illuminates the cavity and the reflected light falls on three detectors simultaneously. Two of the detectors have F-P filters on them; one filter is $\lambda_0/8$ thicker than the other. The difference between the optical path length of the filters and the head F-P cavities is $<^{\circ}L_{coh}$ so the light falling on the filtered detectors varies as pressure alters the cavity gap. As the head cavity length changes one detector will see maximum intensity while the other will see intensity in between the maximum and minimum. If one filtered detector's normalized output is plotted vs. the other, the curve will spiral out, and then back. If

the head optical path length is confined to be either greater or less than the reference cavities, each point on the spiral will correspond to a unique head gap. Back reflection from connectors will add to the signal from the filtered and normalization detectors, which could cause an incorrect, turn on the spiral to be chosen and thus a large error in the pressure measurement.

Another demodulation technique which works with cavity movements in excess of $\lambda_0/2$ and uses a wide line width source is to send the light reflected from the sensor head, which has its OPL$^{\circ}>>^{\circ}L_{coh}$, into an analyzing interferometer and adjust it for maximum fringe visibility. Then the analyzing interferometer's OPL matches that of the sensor. Such a technique is insensitive to variations in source wavelength, link transmissivity, and light reflected from connectors, but requires either moving parts or an electro optic modulator. It is also necessary to accurately ascertain the OPL of the analyzing interferometer. A demonstration of the technique is given in [9] . Their analyzing interferometer consists of two metal-coated glass plates whose separation can be controlled with a piezoelectric translator. This separation is determined by incorporating the metal-coated plates, which form a capacitor, in a circuit whose frequency is proportional to the plate's spacing. To set the plate's separation to match the head, a sinusoidal dither, which varies the plate separation by ~2°μm, is applied to the piezoelectric translator, and the fringe movement (AC output of the interferometer) measured with a photodiode. The fringe amplitude will increase as the dither moves the mirrors to the place of maximum fringe visibility.

In the dither cycle, as the plate separation changes, a rapidly varying sinusoid, corresponding to interference between the two plates, will be noted. This variation will come under an envelope, and its peak will coincide with the glass plate separation providing maximum fringe visibility. At the peak, the head and analyzing interferometer's OPL will match. To make the average plate separation coincide with this peak, the analyzing interferometer's photodiode

output is high-pass filtered (giving it zero DC content), rectified, and peak followed (low pass filtered). The sign of the dither sinusoid then multiplies this signal, which will follow the envelope. If the envelop peak coincides with the zero crossing of the dither, the peak will be split, with one-half being multiplied by +1 and one half by -1 and the product will have zero DC value. If the peak falls on one side of the dither (say the -1 side) then the multiplication will produce a signal having a negative average value which when low pass filtered gives a negative DC voltage. The DC signal is fed back to the piezoelectric translator, which adjusts the mirror spacing, making its average position identical to that of the sensor head.

An alternative approach by Belsley *et al*. is to replace the piezoelectrically adjusted cavity with a spectrometer-microprocessor [10]. In this scheme LED light with a coherence length less than twice the spacer thickness interrogates a F-P cavity at the end of an optical fiber. The reflected light, spectrally modulated by the cavity (Figure 4.4), is wavelength-separated. To decrease the time between pressure measurements, a linear photodetector array simultaneously measures the wavelength-segment's amplitude. This information is fed into a microprocessor, which determines the pressure (they are not specific about how that's done). It is claimed that the instrument possesses a 0.002% resolution, a 0.02% hysteresis and a temperature zero point shift of 0.005%/ ^{0}C. Since the microprocessor must process many intensity points and may need to use a computationally complex algorithm to extract the pressure, a concern is that the time between readings may be excessive. No data rates are provided, however.

In a separate paper, Velluet *et al.* [11] suggests that a spectrophotometer-determined cavity separation can give the absolute cavity size, with no restriction that it move less than $\lambda_0/4$. The period of the sinusoidal variation in wavenumber (reciprocal wavelength) space can provide a coarse estimate, with the phase providing the refinement. One possible problem if the cavity is

vented to make a relative pressure sensor is that air between the two plates can squeeze-film dampen rapid pressure variations, limiting the device s frequency response [12] .

4.3 Packaging of Prototype Sensors

One of the very important advantages with the pressure and temperature sensors described in this thesis is epoxy is not used in the fabrication process. This results in application of these sensors in high temperature environments where otherwise limited by use of epoxy. Some fiber optic sensors described in Chapter 1 use optical fibers for interrogating sensor head which is a separate entity [Ref. 1-5, Chapter 1]. In these cases, fixing of the fiber to the sensor head requires use of epoxy, thus limiting the high temperature applications.

The two sensors described in this thesis are integrated into the end face of an optical fiber, thus not requiring epoxy, but as we present in this section, the prototype pressure sensors were packaged in order to test in a pressure chamber. In this process, we have used epoxy; however, this is not a requirement inherent to the device as was the case with above mentioned sensor types.

Pressure sensors were fabricated on 6 cm long fiber pieces. A packaged pressure sensor is shown in Figure 4.5. The end where the pressure sensor was fabricated connected to a 1/2 swage lock so that this end can be screwed in to the pressure chamber. The other end was connected to a SMA connector so that this end could be connected to one of the arms of 2×1 coupler in the measurement system. The SMA connector was linked to the Swage lock via 1/16 stainless steel tubing. The summary of the procedure for the packaged pressure sensor shown in Figure 4.5 is as follows: the tubing on the backside of SMA connector (back-ferrule) was removed while leaving the front-ferrule in the connector. 1/16 tubulation was inserted into the

backside of the connector and was epoxied. The removed back-ferrule was replaced and was potted with electronic hard potting. Next, the tubulation was cut into the length of the fiber sensor. This step followed attaching the 1/16 swage-lock nut and ferrule to the tubulation with the sensor in the tubulation in such a way that only a few millimeters of length protruded from the front-ferrule of the SMA connector. The sensor was now epoxied into the Swage lock assembly. Finally, after epoxy was cured, fiber was cleaved at the SMA connector ferrule and polished as described in section 3.3.

The packaged fiber sensor pressure sensor array is shown in Figure 4.6. Six identical sensors were fixed to an aluminum fixture using epoxy. The fixture was specially designed for use with the pressure chamber. The backside of the fixture carries six metal tubulation providing the fibers with flexibility to bend. The other side of all six-fiber sensors was connectorized with SMA connectors.

Temperature sensors were not packaged when tested. One side of the temperature sensor was connectorized for connecting to the measurement system.

4.4 Results and Discussion - Characterization of Sensors

In this section we present some of the initial testing of the pressure and temperature sensors. These initial testing results will be compared with calculated results.

4.4.1 Characterization of Pressure Sensor

The optical detection scheme is based on the fact that the reflected light from the sensor is spectrally shifted (see Ref.1). This measurement scheme is shown in Figure 4.7. A broadband light emitting diode (LED) centered at 850 nm was routed onto the sensor through a 2×2 coupler.

The reflected light was collected back through the same fiber and was routed to a second 2×2 coupler that splits the reflected light into two equal intensity signals. One of the signals was routed to a photodetector and the other to a high band pass optical filter and photodiode combination. This detection scheme effectively measures the change in reflectivity that result from shifting of the spectrum of the Fabry-Perot sensor (Figure 2.5). The ratio of the output of the two photodetectors was taken to be a measure for the sensed parameter.

A pressure sensor fabricated on an optical fiber with the design values of cavity diameter d=150 μm, cavity depth h=0.640 μm, and diaphragm thickness t=7.1μm was tested showing an approximately linear response to static pressure 0-80 psi. The slope of the best fit to the data gives a sensitivity of about 0.11 mV/psi with ± 0.01 mV/psi departure from linearity. The static pressure response results are shown in Figure 4.8. Each pressure point is the average of 100 readings acquired. The pressure was also monitored with a Druck pressure calibrator and the output was acquired with a computer based data acquisition system. The LED and photodiodes were maintained at a constant temperature with a thermoelectric cooler assembly that can be monitored during experiment to insure constant LED output.

Another pressure sensor was designed to respond over the pressure range 1-60 psi, and to operate at λ_0 =850 nm with d=150 μm, h=0.640 μm, and t=3.4 μm. The intention of this second design where we use a thinner silicon diaphragm was to obtain a greater response. Calculated sensor responses with respect to pressure for two cases of diaphragm thickness are shown in Figure 4.9. According to Figure 4.9 reflectivity from the sensor with 3.4 μm-thick diaphragms over the range 1-60 psi is over 3 times that from the sensor with 7.1 μm-thick diaphragms. The static pressure response results for the two pressure sensors are shown in Figure 4.10. The sensor with 3.4 μm thick diaphragm shows greater response than the sensor with 7.1 μm thick

diaphragm. The slope of the best fit to the measured data for 3.4 μm thick diaphragm gives a sensitivity of about 0.20 mV/psi with ± 0.01 mV/psi departure from linearity.

Even though experimental results of static pressure tests show reasonable sensor performance in terms of response values and sensitivity, these values are about 5 times smaller than those reported previously in [1]. Smaller response values can be due to large losses for reflected light at the inter-connection that connects a 400- m-diameter fiber on which this sensor is fabricated to a 200 m diameter fiber in the measurement system. And low sensitivity values can be attributed to number of reasons. Diaphragms on cavities with smaller diameters deflect to pressure less than those with larger diameters. For example, silicon diaphragm of thickness 7.1 m on a cavity with diameter of 150 m deflect only 37 nm over a pressure range 1-80 psi, whereas a diaphragm of same thickness on a cavity with diameter 300 m deflects 350 nm over the same pressure range (equation 2.40). Multi-mode fibers used in these experiments allow a large number of modes to propagate. Calculations are based on normal incidence of light into the interferometer (air cavity). The angular distribution of the incident light into the cavity will reduce the fringe visibility thus affecting the sensitivity of the sensor. Higher-order modes in the fiber have a larger propagation angle in the fiber so they will have a larger angle of incidence, θ_1 (figure 2.2) once they couple into the air cavity of the sensor. The measured $R_S(\lambda)$ is a power-weighted average of the reflectances of the individual modes. It can be expected that this effect causes a lower sensitivity. Surface roughness on the cavity bottom (resulting from polishing of fiber end face) would also contribute to the effect that light enters the cavity at a range of angles.

4.4.2 Characterization of Linear Pressure Sensor Array

Characterization of pressure sensor arrays was done in a similar manner to that of the single pressure sensor. The same measurement system in figure 4.10 was used. In this initial testing, sensors were tested individually one after the other. The response of individual sensors in the array is shown in figure 4.11. Sensors in the array were numbered in the order they were tested. The sensors numbered 1 through 6 in the array have the following responses in mV: 2.4, 10.5, 12.0, 0.8, 1.0, and 0.6. Only sensors numbered 2 and 3 have significant responses and their response values of 10.5 mV and 12.0 mV respectively are comparable to previously tested single pressure sensor with the same sensor parameters. These two sensors numbered 2 and 3 have approximately the same sensitivity of 0.2 mV/psi.

The other sensors numbered 1, 4, 5, and 6 all have responses less than 3.0 mV. The responses from all six sensors are shown in one graph in figure 4.12. It is also important to note that the base signal level for each sensor is shifted. Shifts as large as 80 mV can be seen. This is likely to result from reflections from SMS-SMA connectors that connect the sensor fiber to the measurement system as well as from fabrication complications of the sensors. Two fabrication steps where most errors are introduced to the sensor parameters are bonding of silicon to fiber and wet etching of the cavity. Bonding alters the effective cavity depth from the design value since it is done at high temperature and slightly different thermal expansion coefficients for fiber and silicon causes the silicon diaphragm to bend over the cavity. And the etching results in Figure3.11 shows that etch depth could vary as much as 30 nm resulting in the variation of the amount of reflected light. Cavity depth also affects the sensitivity of the sensors (Figure 2.7).
An important objective of this project, however, demonstration of processing of number of fibers simultaneously, was achieved. It should be noted that fibers were mounted on the fixture after

each fiber was polished individually. Thereafter, other processing steps were carried out simultaneously for all six fibers.

4.4.3 Characterization of Temperature Sensors

In this section we present characterization of both uncapped (bare silicon bonded on fiber end face) and capped (or encapsulated) (aluminum coated silicon nitride deposited on silicon bonded on fiber end face) temperature sensors. These thin-film Fabry-Perot type sensors were characterized by spectral reflectometry, as described below. To minimize link-sensitive errors, the reflected spectra $R_F(\lambda)$ were divided by the source spectrum $R_{LED}(\lambda)$ to give the sensor reflectivity $R_S(\lambda)$. The source spectrum $R_F(\lambda)$ is actually the one-way transmissivity of the fibers and the 2×1 coupler superimposed on the source spectra. Therefore, to obtain a normalized spectrum, the raw reflectivity spectrum $R_F(\lambda)$ is related to the sensor reflectivities $R_S(\lambda)$ by $R_S(\lambda)=R_F(\lambda)/R_{LED}(\lambda)$.

The measurement system for the temperature sensors is shown in figure 4.13. LED light source (λ=850 nm) with 80 nm FWHM is launched into the optical fiber via a 2:1 fiber-optic coupler at the end opposite the sensor head. The light travels along the fiber to the sensor head. About 15 percent of the incident light is reflected back along the fiber from the silicon-glass interface. The remainder of the incident light travels on to the silicon-air interface, and the light incident on this reflector re-enters the fiber and propagates back along the fiber, along with the light reflected from the silicon-glass interface. The thin-film temperature sensors were inserted into a testing oven chamber. The temperature of the air in the chamber was controlled to within $\pm 0.5\ ^0$C, as measured by a thermocouple.

The fiber-optic coupler directs the two backward-propagating light beams to a spectrometer that is integrated with a 1,200 columns×200 rows-pixel back-illuminated linear charge-coupled-device (CCD) photodetector array on a computer plug-in spectrometer card. Because of interference between the two backward-propagating beams, the CCD output shows characteristic interference fringes; that is, a reflected-intensity versus wavelength spectrum. The dispersion of the spectrometer in the spectral region of 850 nm was measured to be 0.0379 nm/pixel. That is, the spectral range of the spectrometer is 1200×0.0379=45.5 nm. Windows-based image acquisition and analysis software named PixelView captured 16-bit data that corresponded to the image s pixel intensity values and placed the image into personal computer memory, pixel-by-pixel. The spectrometer s wavelength was manually set in such a way that wavelength 850 nm corresponded to the 600^{th} pixel-column in the CCD. The difference between the coefficients of relative refractive index change of Si and optical fiber with temperature gives rise to a spectral shift in the spectrum.

The sensed temperature was determined as a function of λ_m, the resonant wavelength of order m. The fringe order is given by $m=2nL/\lambda_m$ where L is the thickness and n is the refractive index of the Fabry-Perot. The order of the monitored resonance was chosen so that it could be excited, throughout the entire temperature range, with the emission from an 850 nm-wavelength LED.

Figure 4.14 shows the experimental $R_S(\lambda)$ for a thin-film temperature sensor whose silicon thickness is 3.1 μm ($R_S(\lambda)$ was obtained at different temperatures). The thickness of silicon was measured by measuring the step profile of ultra-thin silicon piece bonded onto a glass wafer using Deteak Profilometer. The profilometer has a vertical measurement accuracy of 5 . And the ultra-thin silicon piece used was separated from the wafer piece that was used in the sensor,

so that the measured thickness was an estimate for silicon in the temperature sensor. Figure 4.15 shows the calculated spectrum in the vicinity of 850 nm for a lossless silicon Fabry-Perot whose thickness is 3.1 μm. Periodicity of the calculated spectrum (32 nm) is approximately equal to that in the measured spectrum (31 nm) in the Figure 4.18. Moreover, the resonance minimum of interest is slightly shifted: it is at 836 nm in the calculated spectrum while it is at 839 nm in the measured spectrum. These discrepancies may be due to treating the calculated Fabry-Perot as lossless. However, the mismatch of measured periodicity and positions of minima with those of calculated would not affect the calibration of sensors where we measure shift in resonance minimum, i.e. shift in λ_m, with temperature.

The resonant wavelengths were presumed to correspond to the local minima in the $R_S(\lambda)$ functions, which were located using the following algorithm. To determine λ_m, the reflectivities $R_S(\lambda)$ were obtained in the form of two-dimensional array of numbers corresponding to individual pixel responses of the CCD; in this array, the column-responses represent the spectral distribution. These numbers were first saved as a text file, and then were imported to calculation software Mathematica for mathematical manipulation and plotting. Once the normalized sensor reflectivity spectrum $R_S(\lambda)$ was obtained by $R_S(\lambda)=R_F(\lambda)/R_{LED}(\lambda)$, a third-order polynomial was fit to a row of one-dimensional array of numbers in the two-dimensional array of $R_S(\lambda)$. The row number was chosen from the middle region, i.e. 100^{th} row, where the CCD response was uniform. A third-order polynomial was fit to $R_S(\lambda)$ in the ±3.5 nm region about the minimum. Finally, λ_m was determined by calculating the position of the polynomial s selected minimum. When $R_S(\lambda)$ was obtained at different temperatures and was plotted on the same plot, the minima shift could be seen (Figure 4.16). This plot shows that the spectrum moves towards higher wavelengths; this should be expected since the refractive index of silicon increases with

temperature in this temperature range. The above algorithm presented was found to be simple and adequate for the purpose of calibrating the sensors and assessing their stability.

The capped (aluminum coated silicon nitride) sensor was operated in the range 25-300 ^{0}C. In this case the connectors were not disturbed between the measurements. For this sensor, the total shift in minima over the above temperature range is 16.2 nm. The dispersion of the spectrometer in the spectral region of 0.0379 nm/pixel was used in the determination of shift in spectral minima. The $R_S(\lambda)$ measurement of an un-encapsulated sensor with 3.1 μm thick silicon at the above extreme temperatures of 25 and 300 ^{0}C showed a total minimum shift in minima of 16.8 nm (Figure 4.17). Although $d\lambda_m/dT$ would be unaffected by the thickness of silicon, encapsulation of silicon increases the overall reflectivity of silicon thin —film and thereby increasing the fringe visibility which could improve the resolution of λ_m.

In these experiments, the sensor fibers were connected to the 2×2 coupler by means of a detachable SMA-SMA adapter for convenience. But, in a more systematic and extensive study done by G. Beheim on sputtered thin-film temperature sensors, sensor fibers were fused spliced [11]. This approach prevents reflections from the fiber end faces that reduce the sensor s fringe visibility. Reduced fringe visibility gives rise to inaccurate determination of minima/maxima, thereby giving rise to inaccurate determination of temperature. Use of detachable connectors/adapters not only reduces visibility of fringes, but it also gives rise to variation of reflected light level. This was evident when the sensor fiber was remated repeatedly by keeping the sensor at a constant temperature of 250 ^{0}C. A simple test done to gather data at 10 remating occurrences at 250 ^{0}C showed that λ_m did not vary beyond the measurement uncertainty. This scatter may not affect our temperature measurements using the spectrometer because we determine the temperature by tracking the spectral minima/maxima and effects due to remating

can be considered to be λ-independent. But for the use of other measurement system, such as those that measure intensity of light, this will yield inaccurate results.

Figure 4.18 shows that a quadratic function accurately fits the data for the encapsulated temperature sensors. A linear fit to λ_m (T) provides $\kappa_\phi=(7.2\pm0.1)\times10^{-5}/^0C$ for the capped sensor, and $\kappa_\phi=(7.5\pm0.6)\times10^{-5}/^0C$ for uncapped sensor where $\kappa_\phi=\lambda_m^{-1}d\lambda_m/dT$ (Figure 4.21 and Figure 4.22). Since $\lambda_m\approx832$ nm, $\kappa_\phi=\lambda_m^{-1}d\lambda_m/dT$, can be used as an approximate means to convert λ_m changes to the measured temperature T_M. The measured values of κ_ϕ are close to the value of $7.9\times10^{-5}/^0C$ that was determined using the published material properties for crystalline silicon. In the case of uncapped sensor, κ_ϕ has a greater uncertainty than in the capped sensor; this is apparent in Figure 4.19 where data points are scattered more than in the case of capped sensor. This could result from increased fringe visibility in the case of capped sensor, which allows accurate determination of resonance minima. Further, the uncapped sensor allows stray light in the sensor that could contribute to scattering of data.

It is evident from the plots in Figure 4.20 that the graph corresponding to the capped sensor has κ_ϕ that is more deviated from the published value of $7.9\times10^{-5}/^0C$ than the uncapped sensor. There are two reasons to this effect, they are, (1) capped sensor design was based on a very simplified model and (2) LPCVD deposited Si_3N_4 film thickness was slightly shifted from the design value. Uncapped sensor, however, resulted in κ_ϕ is equal to $7.9\times10^{-5}/^0C$ within the measurement uncertainty.

The plot shown in Figure 4.21 shows the deviation of temperature for the capped sensor from quadratic and linear fits. Temperature values on the Y-axis correspond to the deviations of resonance shifts from the quadratic and linear fits and were calculated using $\kappa_\phi=\lambda_m^{-1}d\lambda_m/dT$. This plot shows that there is a maximum deviation of nearly 6 ^0C(from quadratic fit), leading to

an accuracy of temperature measurement by the same. It is as high as 11 ^{0}C in the case of linear fit. It is also important to note that there are other effects such as connector remating, wavelength —dependent changes in the transmissivity of the fiber link, and fiber bending that contribute to the accuracy of temperature measurement. But study of these effects is beyond the scope of this thesis. It is also reported that the temperature resolution of this type of sensors is limited by the wavelength stability of the fiber-coupled spectrometer [11].

4.5 Stability of Sensors

Two sensors, one encapsulated and the other uncapped, were fully exposed to the air inside an oven chamber. They were held in close proximity to each other and the reference thermocouple. The oven temperature was brought to the 250 ^{0}C soak temperature and allowed to stabilize for 6 hrs before the baseline $R_S(\lambda)$ measurements were performed. Subsequently, $R_S(\lambda)$ of each sensor was measured at intervals of 24 hrs. The resonant wavelengths were determined using the method described in the above section. The shifts in λ_m, relative to the baseline values, were converted to changes in T_M using the measured value of $\kappa_\phi=(7.5\pm0.6)\times10^{-5}/^0$C for the uncapped sensor, and $\kappa_\phi=(7.2\pm0.1)\times10^{-5}/^0$C for the encapsulated sensor where $\kappa_\phi=\lambda_m^{-1}d\lambda_m/dT$. Measured temperature data for capped and uncapped sensors over 10 day period is shown in Figure 4.22. It shows that none of the sensors show any systematic drifting of temperature. Instead they show random variation about the temperature recorded on day 1. In fact, the stability tests should have been done for much longer than 240 hrs for observance of any temperature drift due to oxidation, but time constraints prevented such long-term stability measurements to be completed before the submission of this thesis.

4.6 Concluding Remarks

Common problems with optical sensing systems have been presented. Examples of optical pressure sensor measurement systems of various designs have been provided. Intensity sensors, while simple to interrogate, require more effort to link insensitize. Two measurement systems, which measure spectral shifts, have been employed in characterizing the sensors.

Two pressure sensors were tested in the pressure range 1-80 psi. Sensor sensitivities of 0.1 mV/psi and 0.2 mV/psi were obtained. Higher sensitivity was achieved by design of a sensor with thinner diaphragm. Pressure sensor array was tested in the same measurement system as single pressure sensors. Two of six sensors in the array yielded a sensitivity of 0.2 mV/psi. Inability to control the cavity depth accurately and complications resulting from high temperature bonding method were attributed to insignificant response from other sensors in the array.

Temperature sensors were tested in the range 25 to 300 ^{0}C. The measured values of $\kappa_\phi = \lambda_m^{-1} d\lambda_m/dT$ for both capped as well as uncapped sensors are close to the value of $7.9\times10^{-5}/^0$C that was determined using the published material properties for crystalline silicon. Encapsulated sensor and uncapped sensors yielded minimum temperature readings of 5 and 12 ^{0}C respectively. Short-term stability test performed at 250 ^{0}C on these sensors did not show any systematic drift of temperature. Long-term stability tests are to be performed.

4.7 References

[1] L. A. Johnson and S. C. Jensen, Problems and Approaches for Remote Fiber Optic Absolute Sensors, presented at Fiber Optic and Laser Sensors III, San Diego, CA, and published in Proceedings of SPIE, vol. 566, pp. 45-53, 1985.

[2] I. P. Giles, S. McNeill, and B. Culshaw, A Stable Remote Intensity Based Optical Fibre Sensor, *J. Phys. E: Sci. Instr.* , vol. 18, pp. 502-504, 1985.

[3] Greg Brabander, Ph.D. Thesis, University of Cincinnati, Cincinnati, Ohio, 1997.

[4] R. A. Lieberman and G. E. Blonder, An Improved Interferometric Pressure Optrode, presented at Fiber Optic and Laser Sensors V, San Diego, CA, and published in proceedings of SPIE, vol. 838, pp. 49-59, 1987.

[5] B. Masterson and J. Webb, Better Diode Lasers Will Expand Applications in Many Areas, *Photonics Spectra*, pp. 119-124, May 1992.

[6] E. W. Saaski, J. C. Hartl, G. L. Mitchell, R. A. Wolthuis, and M. A. Afromowitz, Multimode Fiber Optic Pressure Sensor with Extended Range, presented at Fiber Optic and Laser Sensors V, San Diego, CA, and published in proceedings of SPIE, vol. 838, pp. 46-48, 1987.

[7] J. P. Dakin, C. A. Wade, and P. B. Withers, An Optical Fiber Pressure Sensor, presented at Fiber Optics 87, London, England, and published in proceedings of SPIE, vol. 734, pp. 194-201, 1987.

[8] B. Halg, A Silicon Pressure Sensor With an Interferometric Optical Readout, presented at International Conference on Solid State Sensors and Actuators, pp. 682-684, 1991.

[9] G. Beheim, K. Fritsch, and R. N. Poorman, Fiber-Linked Interferometric Pressure Sensor, *Rev. Sci. Instr.*, vol. 58, pp. 1655-1659, 1987.

[10] K. L. Belsley, D. R. Huber, and J. Goodman, All-Passive Fiber-Optic Pressure Sensor, *InTech*, vol. 33, pp. 39-42, 1986.

[11] M. T. Velluet, P. H. Graindorge, and H. J. Arditty, Fiber Optic Pressure Sensor Using White Light Interferometry, presented at Fiber Optic and Laser Sensors V, San Diego, CA, and published in proceedings of SPIE, vol. 838, pp. 78-83, 1987.

[12] M. Andrews, I. Harris, and G. Turner, A Comparison of Squeeze-Film Theory With Measurements on a Microstructure, *Sensors and Actuators A*, vol. 36, pp. 79-87, 1993.

[11] Glenn Beheim, Ph.D. thesis, Case Western Reserve University, Cleveland, Ohio, May 1996.

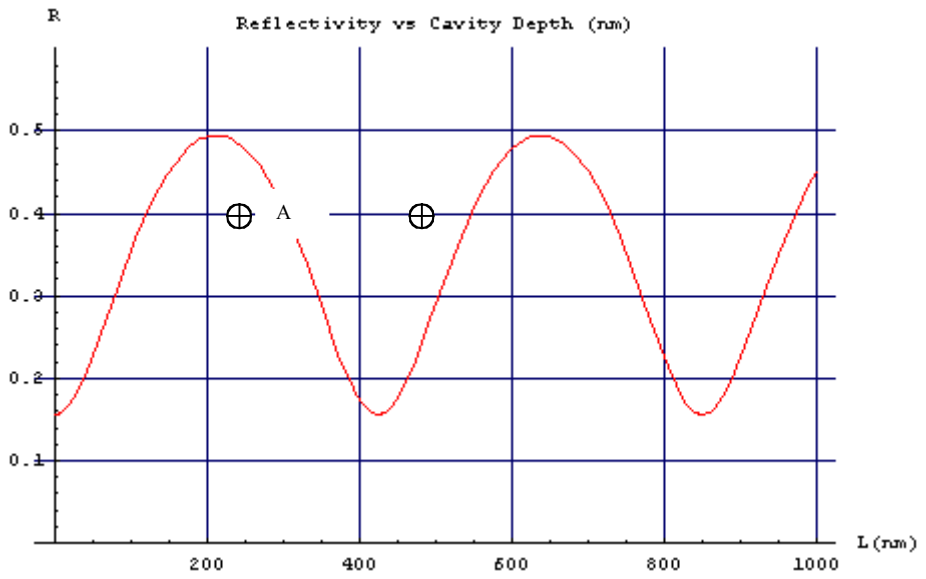

Figure 4.1 The ambiguity problem: If sensor output is at *A* and falls, has the measurand increased or decreased? Existence of zero problem: If the measurand could lie between 200 and 600, and at turn-on the sensor output is 0.4, what is the measurand? Link independence problem: If the DC signal from the output fiber is 0.4 and the measurand lies between 0.3 and 0.5 but the fiber transmissivity could have changed since calibration, what is the measurand?

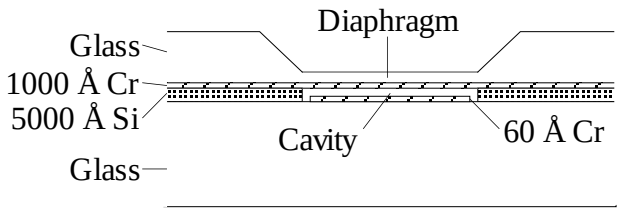

Figure 4.2 F-P pressure sensor head

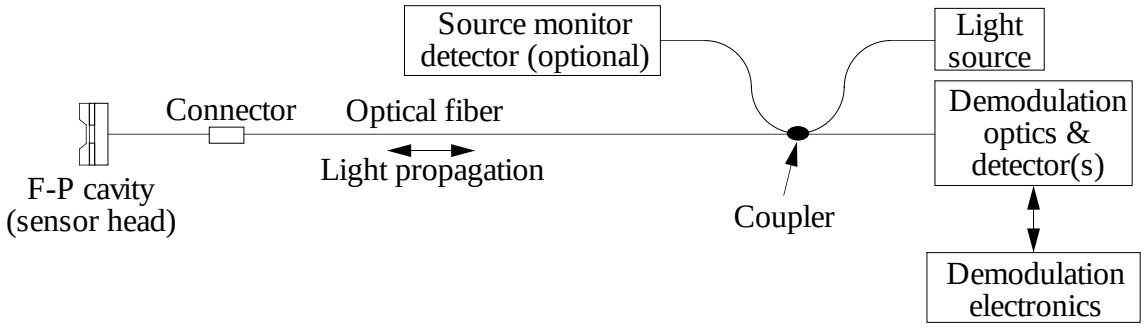

Figure 4.3 Typical implementation of F-P type sensor.

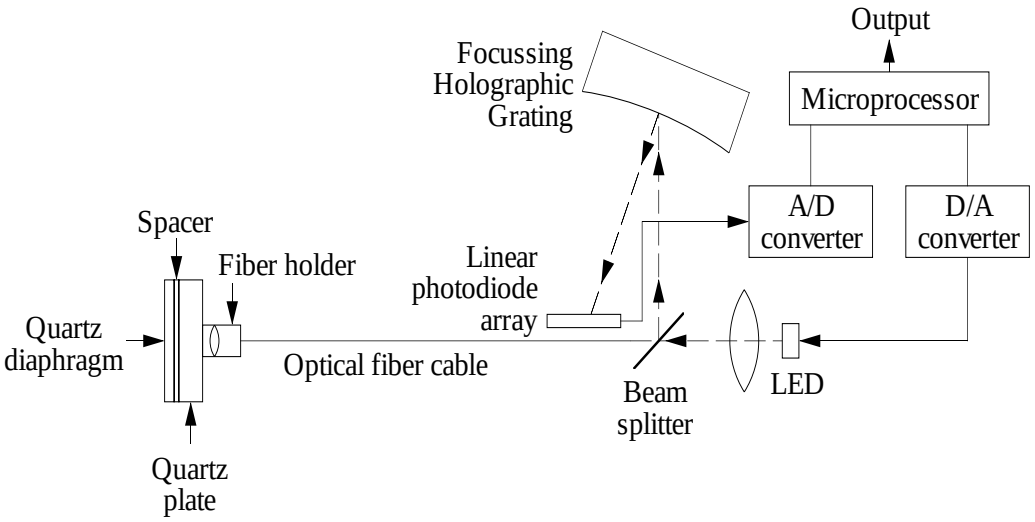

Figure 4.4 Pressure sensor employing a F-P head and a spectrometer to determine cavity separation. [8].

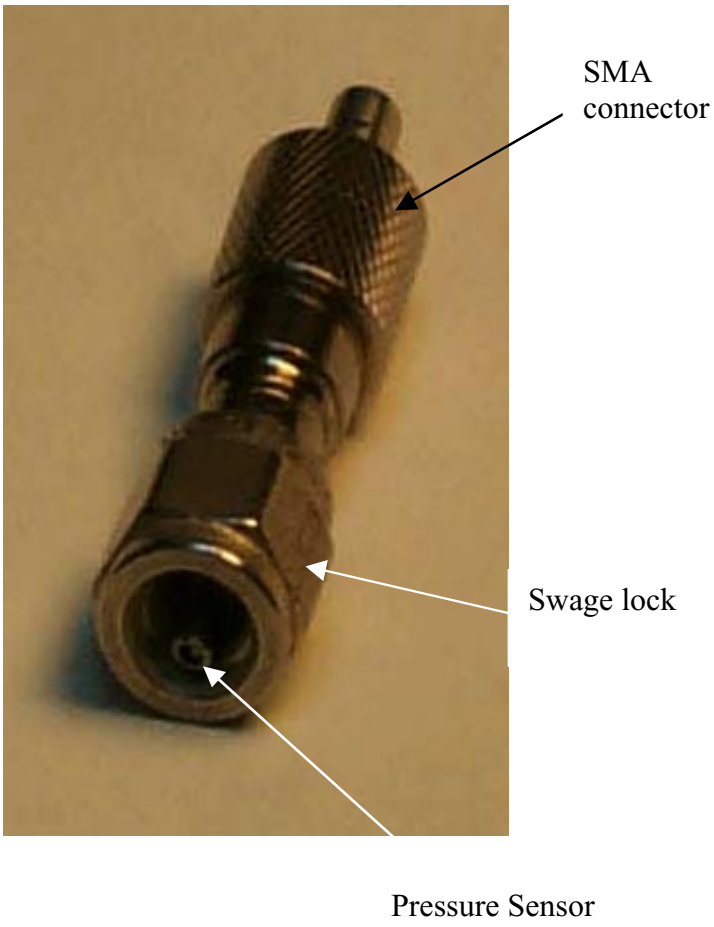

Figure 4.5 Packaged pressure sensor.

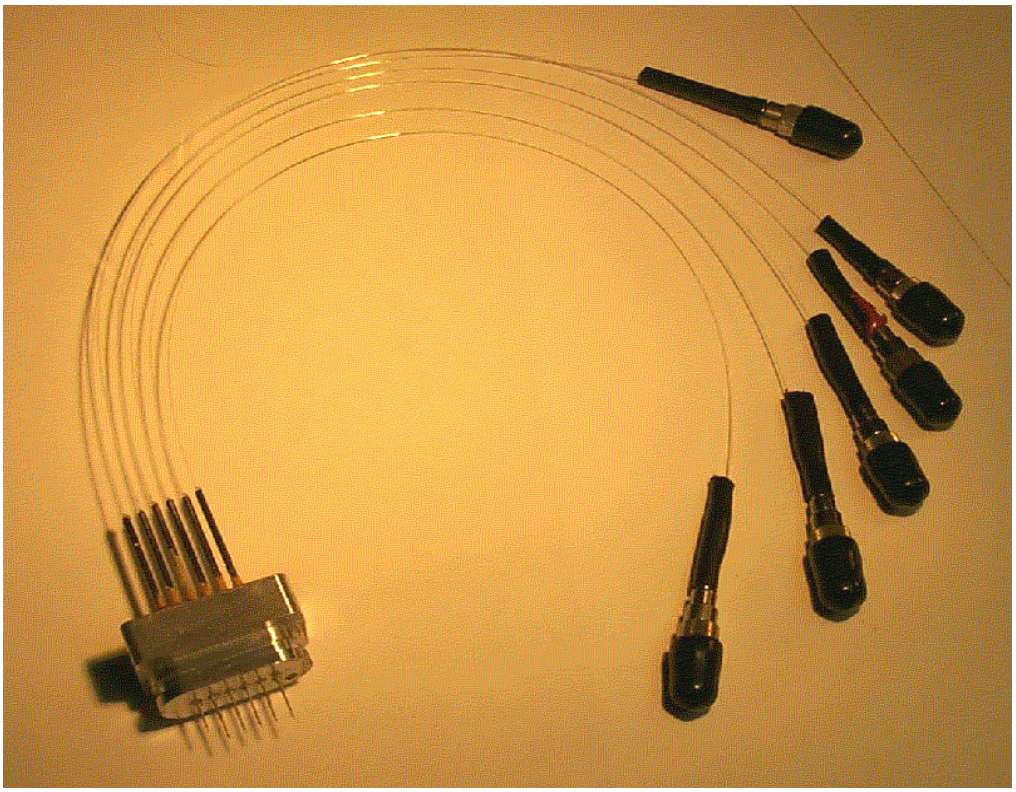

Figure 4.6 Packaged pressure sensor array.

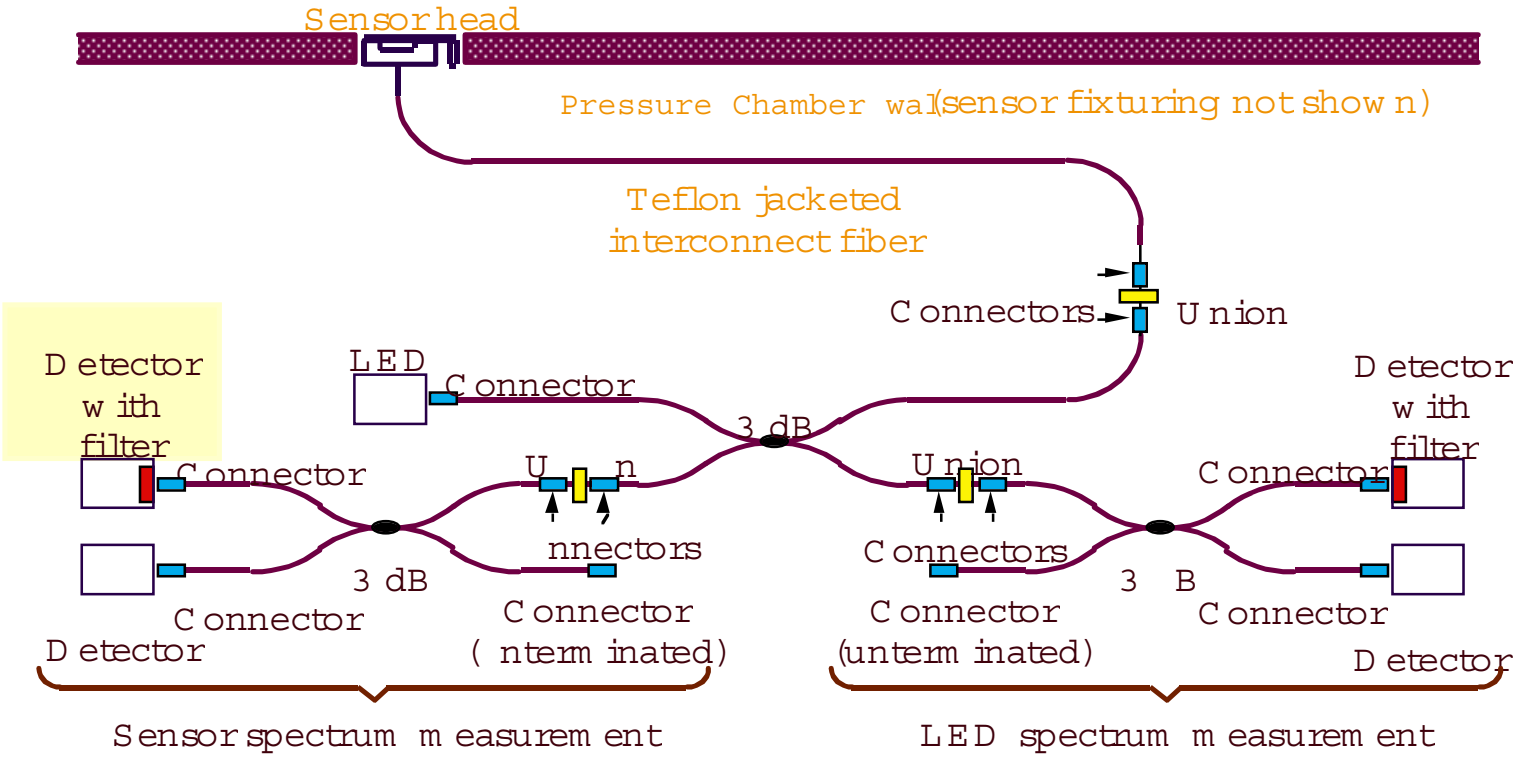

Figure 4.7 Pressure sensor measurement system.

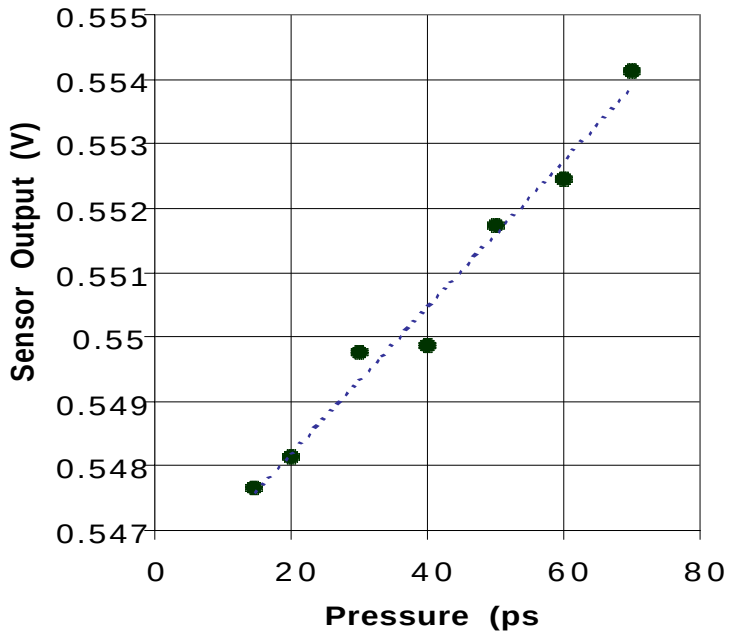

Figure 4.8 Plot of sensor output in volts versus pressure in psi. Each pressure point is an average of 100 readings. The best fit to the data gives a sensitivity of about 0.11 mV/psi with ± 0.01 mV/psi departure from linearity.

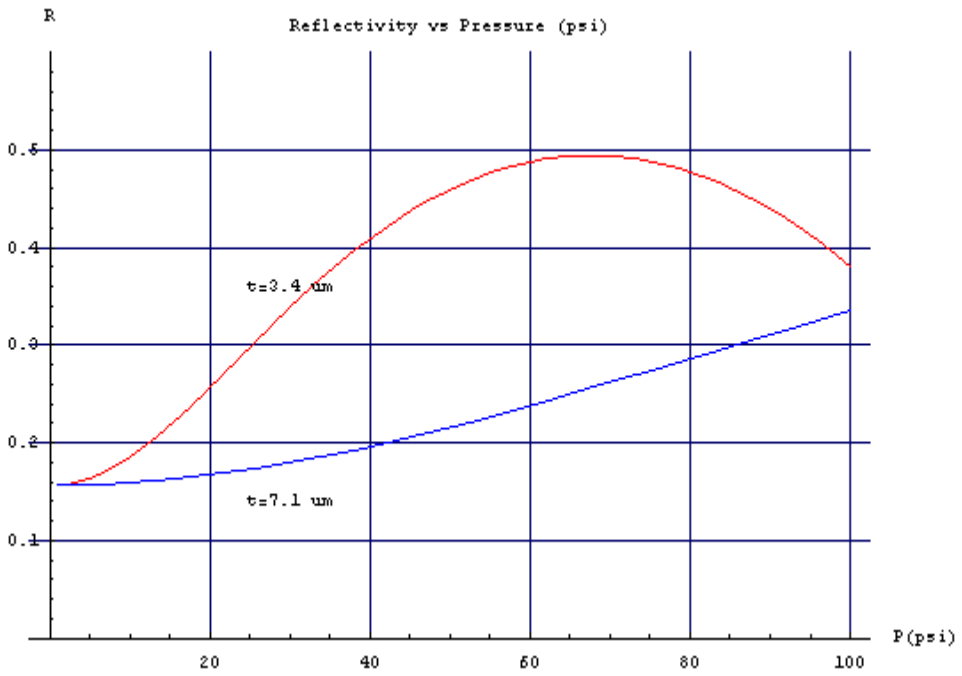

Figure 4.9 Calculated sensor responses with respect to pressure for two cases of diaphragm thicknesses t=3.4 μm, and t=7.1 μm. The cavity depth h=0.640 μm and cavity diameter a= 180 μm for both cases.

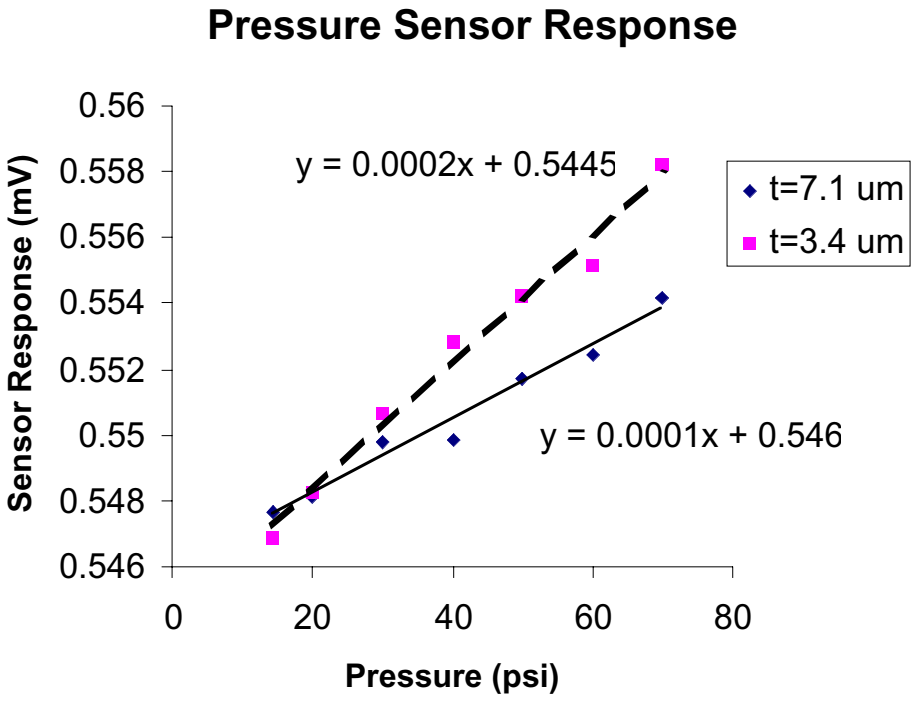

Figure 4.10 Plot of sensor output in volts versus pressure in psi for two sensors with thicknesses t=3.4 μm, and t=7.1 μm. Each pressure point is an average of 100 readings. The best fit to the data is also shown.

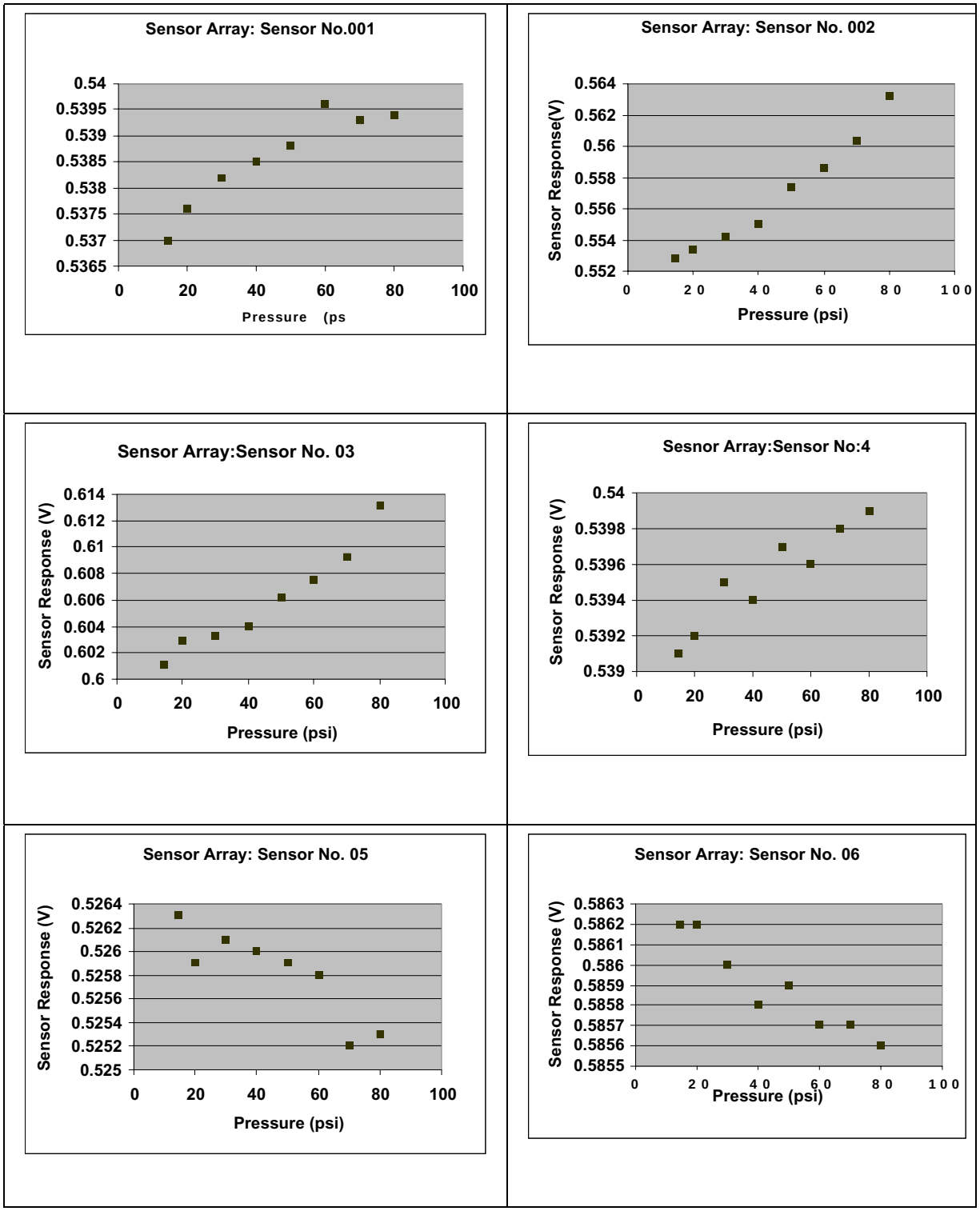

Figure 4.11 The response of individual pressure sensors in the array

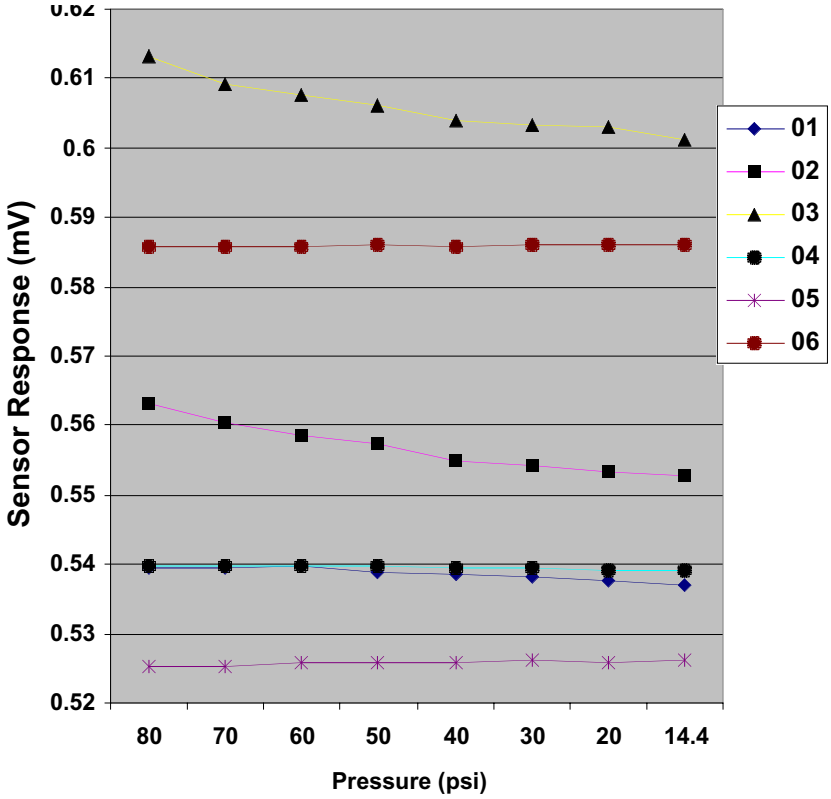

Figure 4.12 The response of individual pressure sensors in the array.

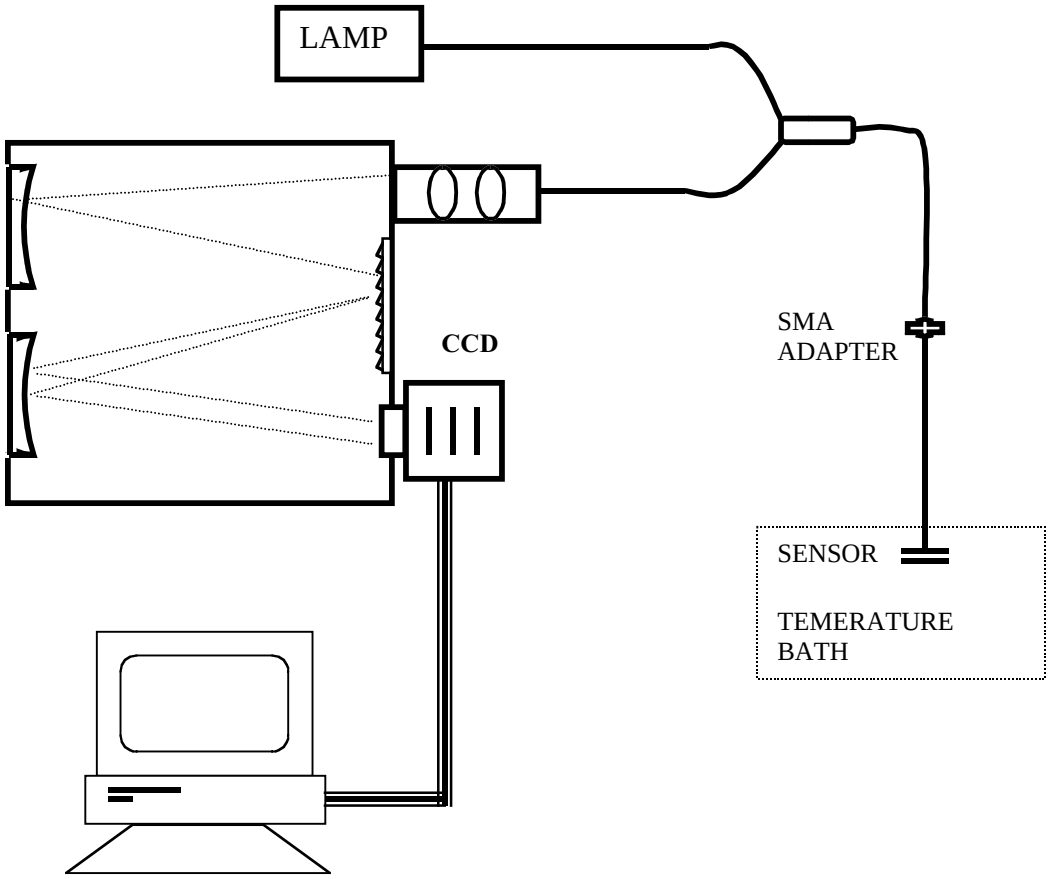

Figure 4.13 Measurement system for the temperature sensor.

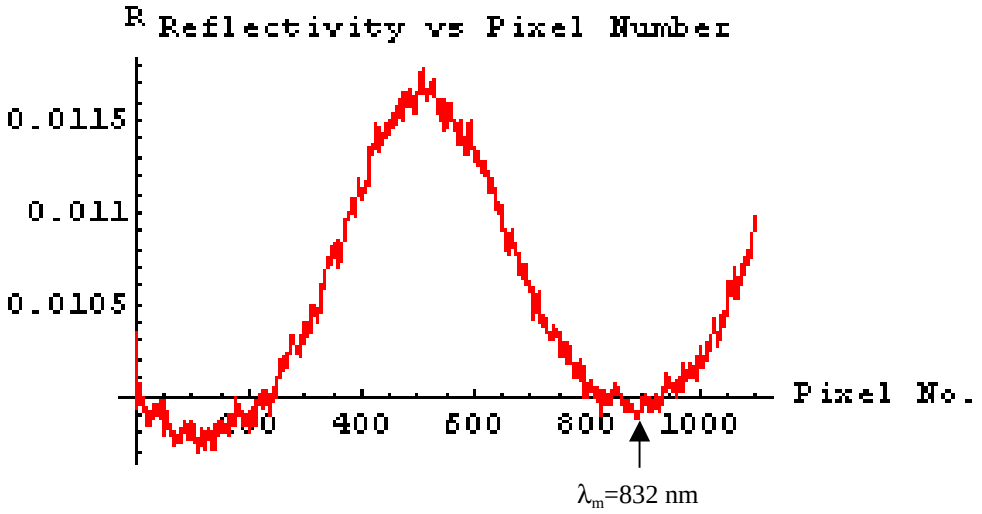

Figure 4.14 Experimental $R_S(\lambda)$ for a thin-film temperature sensor whose silicon thickness is 3.1 μm. Increasing pixel number corresponds to decreasing wavelength.

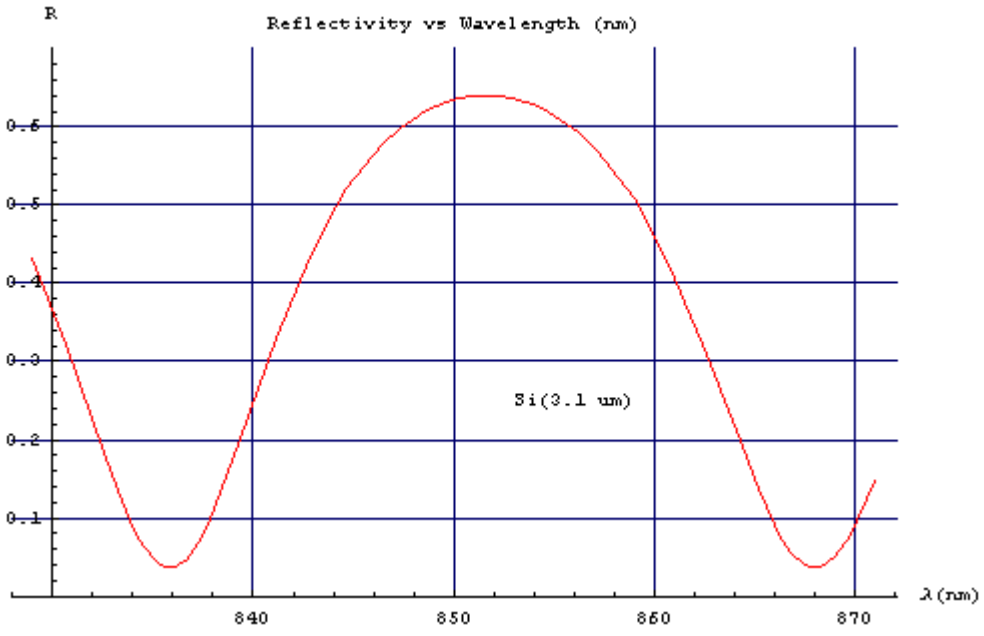

Figure 4.15 Calculated $R_S(\lambda)$ spectrum in the vicinity of 850 nm for a lossless silicon Fabry-Perot whose thickness is 3.1 μm.

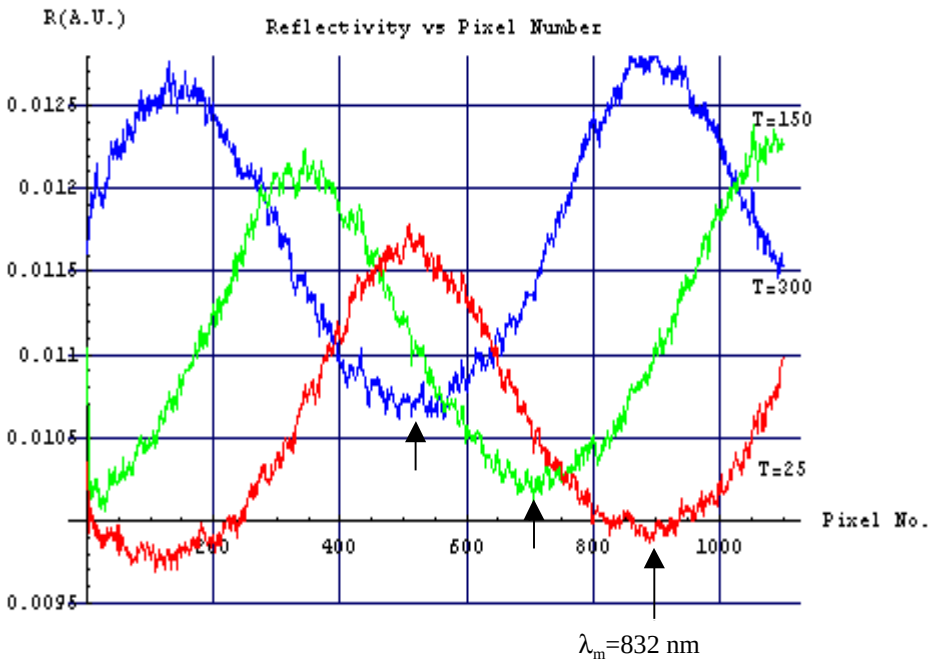

Figure 4.16 Experimental $R_S(\lambda)$ obtained at different temperatures, the shift in minima at λ_m=832 nm was recorded.

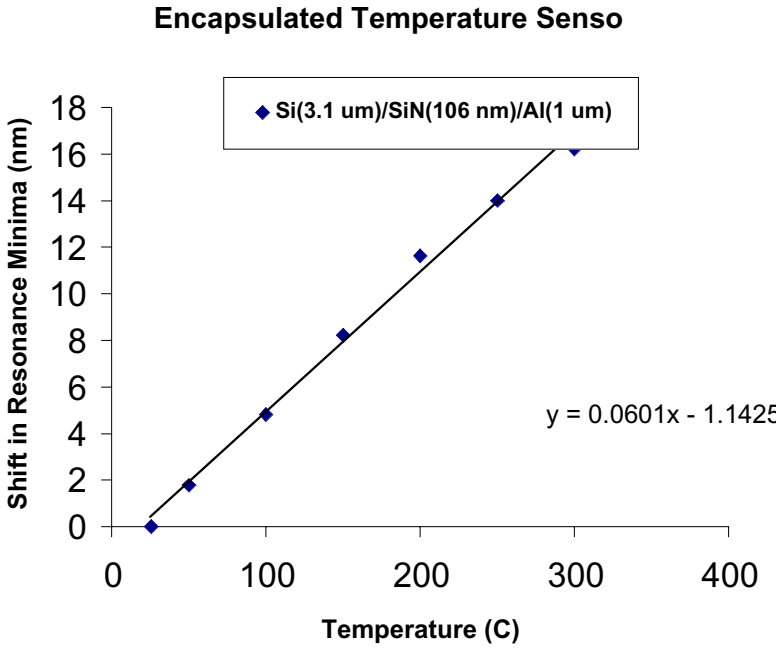

Figure 4.17 Measured λ_m versus temperature data for the encapsulated temperature sensor fitted to a linear function.

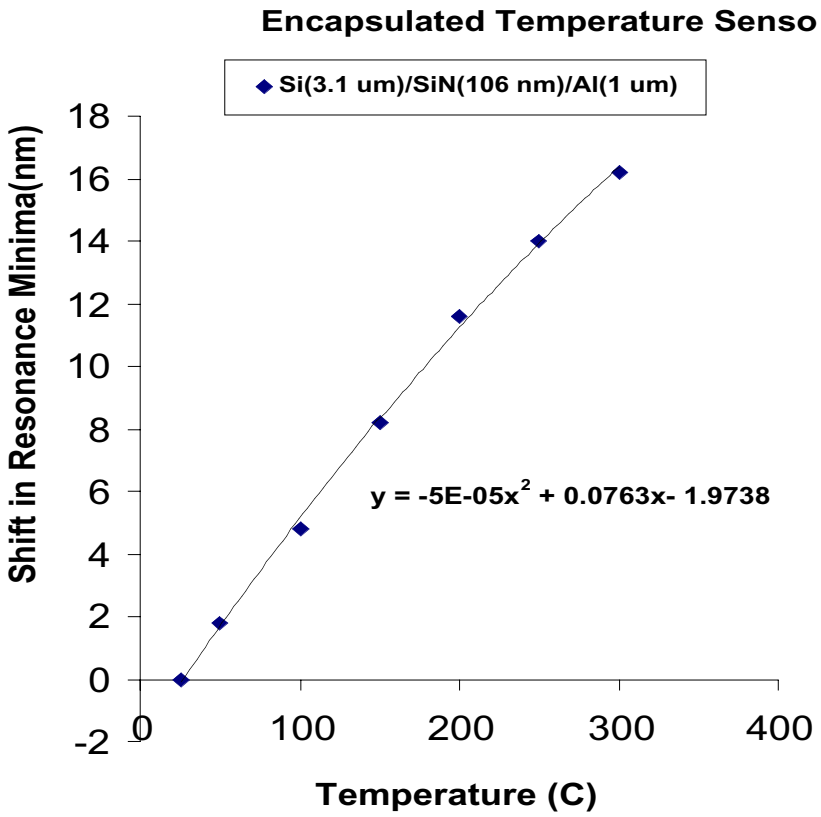

Figure 4.18 Measured λ_m versus temperature data for the encapsulated temperature sensor more accurately fits to a quadratic function than a linear function.

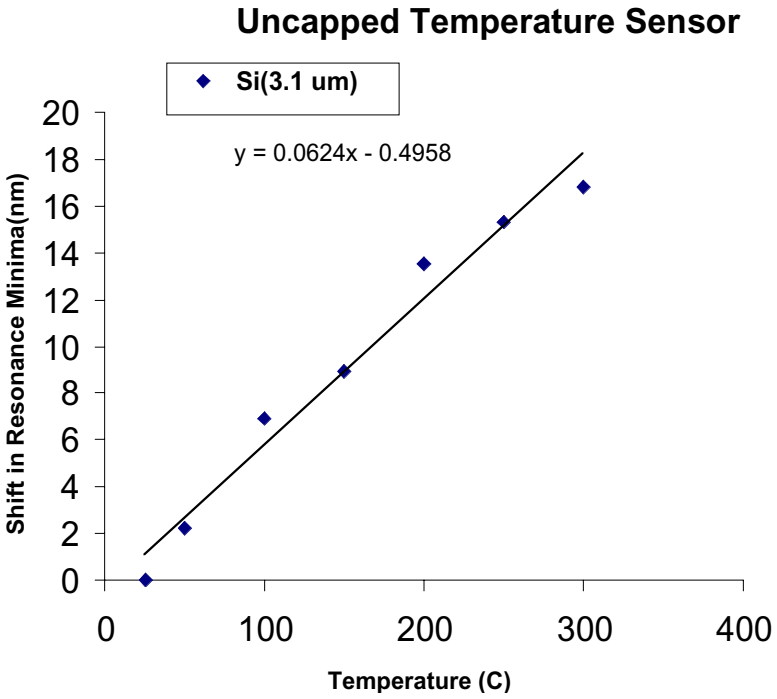

Figure 4.19 Measured λ_m versus temperature data for the uncapped temperature sensor fitted to a linear function.

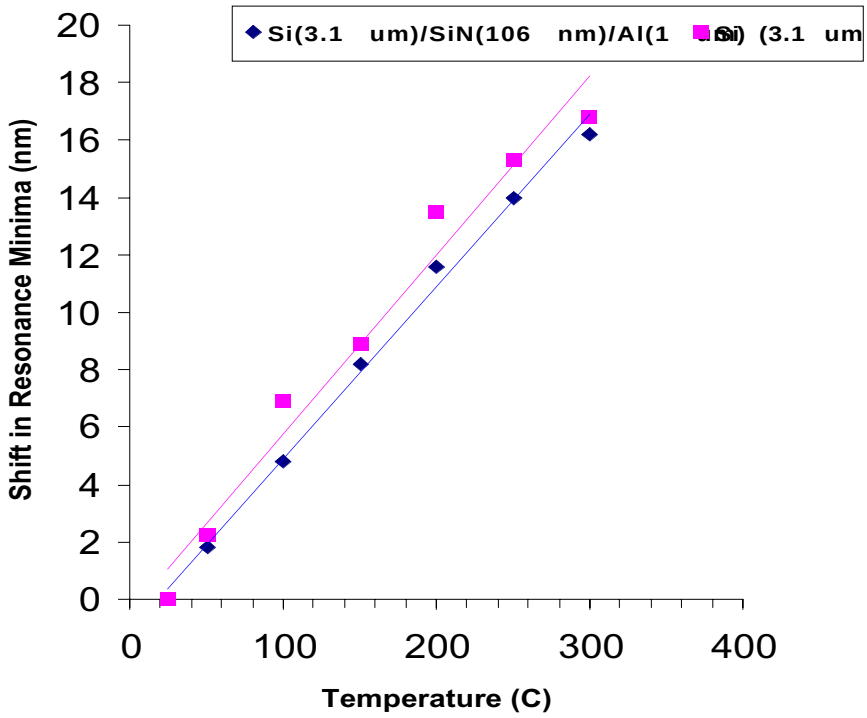

Figure 4.20 Measured λ_m versus temperature data for the uncapped and capped temperature sensors fitted to a linear function.

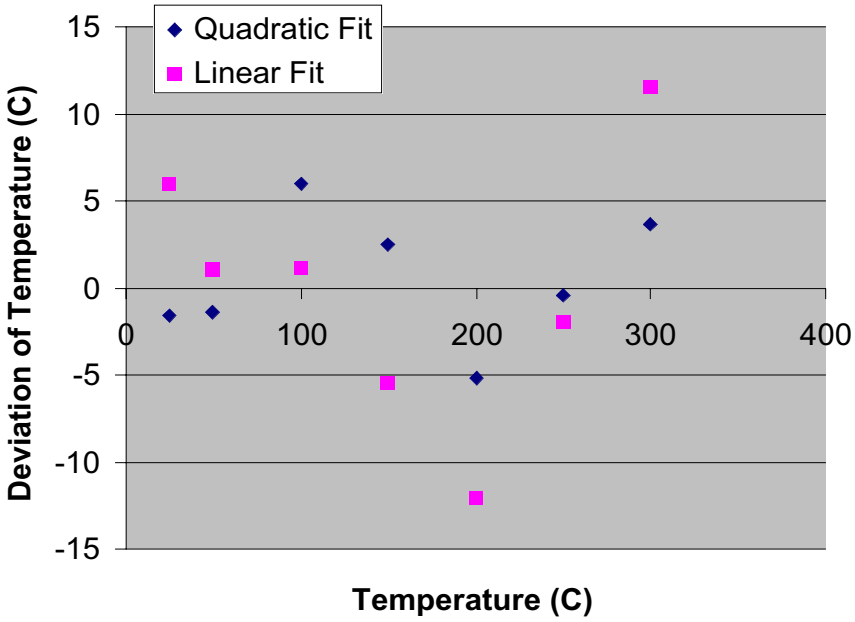

Figure 4.21 The deviation of temperature for the capped sensor from quadratic and linear fits

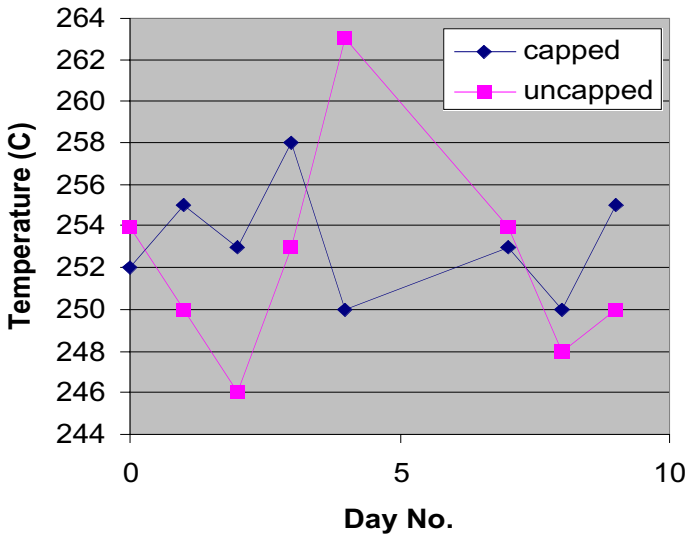

Figure 4.22 Short-term Stability test results for capped and uncapped sensors. Both sensors were maintained at a temperature bath of 250 ^{0}C.

5 Conclusions

Novel MEMS pressure and temperature sensors were fabricated on fiber end faces so that their sizes were the same as the diameter of the optical fiber. Pressure sensors were fabricated on 400 μm diameter fibers while temperature sensors were fabricated on both 200 and 400 μm diameter fibers. Two single pressure sensors, and two temperature sensors were fabricated and tested by reflectometry (λ_0=850 nm). An array of six identical linearly spaced pressure sensors were also fabricated and tested. Pressure measurements were made over the 14 to 80 psi range while temperature measurements were made over the 23 to 300 ^{0}C range. Temperature sensors were tested both with and without encapsulation.

A simple micromachining process compatible with MEMS was developed in fabricating a novel pressure sensor on an optical fiber. The light-guiding capability of optical fibers and the photoresist-exposing capability of a low-wavelength Argon ion laser (λ=457.9) were utilized in this process. Bonding of silicon to the fiber end face was done successfully by employing the anodic bonding method.

Two pressure sensors were tested in the pressure range 1-80 psi. Sensor sensitivities of 0.1 mV/psi and 0.2 mV/psi were obtained and a nearly a linear response over this range was observed. The sensors were fabricated with the design values of cavity diameter d=150 μm, and cavity depth h=0.64 μm. Diaphragm thickness for the two sensors were t=7.1, and t=3.4 μm. Higher sensitivity was achieved by design of a sensor with thinner diaphragm.

Following successful fabrication of a single pressure sensor, an array of six identical sensors was fabricated. This effort demonstrated that our micromachining process could be extended to simultaneous fabrication of an array of sensors.

The success of bonding silicon to fiber end faces was employed to fabricate the thin film temperature sensor. The temperature sensor was fabricated by bonding 3.1 μm thick silicon onto the fiber end face. An oxidant-resistant encapsulation scheme for the temperature sensor was proposed, namely aluminum coated silicon nitride (Al/Si_3N_4). The uncoated side of silicon was bonded to the fiber end face using the anodic bonding method. An idealized model was used which neglects absorption and assumes equal reflectivites at both surfaces of the film. The measured values of $\kappa_\phi=\lambda_m^{-1}d\lambda_m/dT$ for capped and uncapped sensors were $\kappa_\phi=(7.5\pm0.6)\times10^{-5}/^0C$, and $\kappa_\phi=(7.2\pm0.1)\times10^{-5}/^0C$ respectively. The measured κ_ϕ value for the uncapped sensor is equal to that that was determined using the published material properties for crystalline silicon (κ_ϕ $7.9\times10^{-5}/^0C$) within the measurement uncertainty.

The micromachining process developed for micromachining fiber end faces along with the bonding of silicon to fiber end face can be extended to fabrication of other MEMS based micro-optic devices where fiber optic interrogation is advantageous.

6 Bibliography

Andrews, M., I. Harris, and G. Turner, A Comparison of Squeeze-Film Theory With Measurements on a Microstructure, *Sensors and Actuators A*, vol. 36, pp. 79-87, 1993.

Anthony, T. Anodic bonding of imperfect surfaces , Journal of Applied Physics, 54, pp 2419-2428, 1983.

Ballard,S.S., K.A. McCarthy, W.L. Wolfe, Optical Materials for Instrumentation , University of Michigan Report No. 2389-11-S, 1959.

Barth, P., "Silicon fusion bonding for fabrication of sensors, actuators and microstructures," Transducers 89, Proceedings of the 5th International Conference on Solid-State Sensors and Actuators and Eurosensors III, 2, pp. 919-926, June 1990.

Belsley, K. L., D. R. Huber, and J. Goodman, "All-Passive Fiber-Optic Pressure Sensor," *InTech,* vol. 33, pp. 39-42, 1986.

Beheim, G., Fiber-Optic Temperature Sensor Using a Thin-film Fabry-Perot Interferometer , Ph.D. thesis, Case Western Reserve University, Cleveland, Ohio, May 1996.

Beheim, G., K. Fritsch, and R. N. Poorman, "Fiber-Linked Interferometric Pressure Sensor," *Rev. Sci. Instr.,* vol. 58, pp. 1655-1659, 1987.

Beheim, G., K. Fritsch, and D.J. Anthan, Fiber-Optic Temperature Sensor Using a Spectrum-Modulating Semiconductor Etalon , NASA TM-100153, 1987.

Brabander, G., Ph.D. Thesis, University of Cincinnati, Cincinnati, Ohio, 1997.

Campbell, S.A., The Science and Engineering of Microelectronic Fabrication , Oxford University Press, New York, 1996.

Carlson, D., K. Hang, and G. Stockdale, Ion depletion, of glass at a blocking anode II , J. Am. Ceram. Soc., 57(7), pp. 295-300, 1974.

Carriere, T., B. Agius, I. Vickridge, J. Siejka, and P. Alnot, Characterization of silicon nitride films deposited on GaAs by RF Magnetron Cathodic Sputtering , J. Electrochem. Soc. 137, pp. 1582, 1990.

Cocorullo, G., and I. Rendina, Thermo-Optical Modulation at 1.5 μm in Silicon Etalon , Electronic Letters, 28, pp. 83, 1992.

Corman, T., P. Enoksson, and G. Stemme, Low-pressure-encapsulated resonant structures with integrated electrodes for electrostatic excitation and capacitive sensors , Sensors and Actuators, A(66), pp. 160-166, 1998.

Dakin, J. P., C. A. Wade, and P. B. Withers, An Optical Fiber Pressure Sensor, presented at Fiber Optics 87, London, England, and published in proceedings of SPIE, vol. 734, pp. 194-201, 1987.

Driscoll, W.G., ed., Handbook of Optics, (McGraw-Hill, New York, 1978).

Engelke, H., and M. Harz, Curvature changing or flattening of anodically bonded silicon and borosilicate glass , Sensors and Actuators, A 55, pp. 201-209, 1996.

Esashi M., Low-temperature silicon-to-silicon anodic bonding with intermediate low melting point glass , Sensors & Actuators, A21-A23,pp 31-934, 1990.

Farmer, K. R., D. V. Ivanov, W. Peng, M. Beggans Optical pressure sensor head fabrication using ultra-thin silicon wafer bonding, Proc. 1999 SPIE International Symposium on Design, Test and Microfabrication of MEMS/MOEMS .

Ghandi, S.K., VLSI Fabrication Principles, New York: Wiley, Chapter 9,1983.

Giles, I. P., S. McNeill, and B. Culshaw, "A Stable Remote Intensity Based Optical Fibre Sensor," *J. Phys. E: Sci. Instr.*, vol. 18, pp. 502-504, 1985.

Keiser, Gerd, Optical Fiber Communications, third edition, McGraw-Hill International Editions, International editions 2000.

Giovanni, Mario Di, Flat and Corrugated Diaphragm Design Handbook (Mercel Dekker, NewYork), 1992.

Go, J., Y. Cho, Experimental evaluation of anodic bonding process based on the Taguchi analysis of interfacial ftracture toughness, Sensors & Actuators, 73, pp.52-57, 1999.

Gozma, A., Characterization of the electrostatic bonding of silicon and Pyrex glass , J. Electromech. Microeng., 5, pp. 98-102, 1995.

Gozma, A., Characterization and optimization of electrostatic bonding of wafers , Ph.D. thesis, Department of Electrotechnie, Katholieke Universiteit, Leuven:Leuven, 1993/1994.

Halg, B., A Silicon Pressure Sensor With an Interferometric Optical Readout, presented at International Conference on Solid State Sensors and Actuators, pp. 682-684, 1991.

Harris, R.J., G.T. Jonston, G.A. Kepple, P.C. Krok, and H. Mukai, "Infrared Therooptic Coefficient Measurement of Polycrystalline ZnSe, ZnS, CdTe, CaF_2, and BaF_2, Single Crystal KCl, and Ti-20 Glass", Appl. Optics, 16, pp.436, 1977.

Icenogle, H.W., B.C. Patt, W.L. Wolfe, Refractive Indices and Temperature Coedfficients of Germanium and Silicon , Appl. Opt. 15, 2348, 1976.

Jellison Jr.,G.E., and F.A. Modine, Optical Functions of Silicon at Elevated Temperatures , J. Appl. Phys., 76, pp. 3758, 1994.

Johnson, L. A., S. C. Jensen, Problems and Approaches for Remote Fiber Optic Absolute Sensors, presented at Fiber Optic and Laser Sensors III, San Diego, CA, and published in Proceedings of SPIE, vol. 566, pp. 45-53, 1985.

Judge, J. S., " A study of the dissolution of SiO_2 in Acidic Fluoride Solutions", J. Electrochemical Soc., Vol. 118, no. 11, pp. 1772-1775, November 1971.

Kanda, Y., K. Matsuda, C. Murayama, and J. Sugaya, The Mechanism of Field Assisted Silicon-Glass Bonding , Sensors & Actuators, Vol. A21, pp. 939-943, 1990.

Kikyuma, H., N. Miki, K. Saka, J. Takano, I. Kawanabe, M. Miyashita, and T. Ohmi, Principles of Wet chemical Processing in ULSI microfabrication , IEEE Trans. Semicon. Manufact., vol. 4, no. 1, pp. 26-35, February 1991.

Lasky, J., "Bonding of silicon to silicon", Applied Physics Letters, 48(1), pp 78, 1986.

Li, H.H., Refractive Index of Silicon and Germanium and its Wavelength and Temperature Derivatives , J. Phys. Chem. Ref. Data 9, pp. 561, 1980.

Lehmann, V., Ong,. I.W.K., and G sele, U., "Semiconductor Wafer Bonding" Advanced Materials, 8, pp. 372-374,1990.

Lieberman, R. A., G. E. Blonder, An Improved Interferometric Pressure Optrode, presented at Fiber Optic and Laser Sensors V, San Diego, CA, and published in proceedings of SPIE, vol. 838, pp. 49-59, 1987.

Ljungberg, K., Phenomenon of silicon wafer bonding Solid State Electronics, Uppsala:Uppsala, pp. 59, 1995.

Lu, W.J., A.J. Steckle, T.P. Chow, and W. Katz, Thermal Oxidation of Sputtered Silicon Carbide Thin Films , J. Electrochem. Soc., 131, pp. 1907, 1984.

Marple, D.T.E., "Refractive Index of GaAs", J. Appl. Phys., 35, pp.1241, 1964.

Masterson, B., J. Webb, "Better Diode Lasers Will Expand Applications in Many Areas," *Photonics Spectra*, pp. 119-124, May 1992.

Molarius, J.M., E. Kolawa, K. Morishita, M.A. Nicolet, J.L. Tandon,J.A. Leavitt, and L.C. McIntyre,Jr., Tantalum-Based Encapsulants for Thermal Annealing of GasAs , J. Electrochem. Soc, 138, pp. 834, 1991.

Nitzsche, P. et al, Ion drift process in Pyrex-type alkali-borosilicate glass during anodic bonding , J. Electrochem. Soc., 145(5), pp 1755-1761, 1998.

Palik, E.D., ed., Handbook of Optical Constants of Solids, Academic Press, Orlando, 1985.

Paul, C. R., S. R. Nasaar," Introduction to Electromagnetic Fields", McGraw-Hill, New York, 2 nd ed., 1987.

Petersen, K.E., "Silicon as a Mechanical Material", Proc. IEEE 70, pp.420, 1982.

Plaza, J., J. Esteve, and E. Lora-Tamayo, Nandestructive anodic bonding test , J. Electrochem. Soc. 144(5), pp. 108-110, 1997.

Richard, A., K. Sundin, and Y. Backlund, Low temperature anodic bonding of a sub-micrometer fabry-perot cavity , Fifth Int. Symp. On Semiconductor Wafer Bonding, Honolulu, Hawai, 1999.

Rogers, T., J. Kowal, Selection of glass, anodic bonding conditions and material compatibility for silicon glass capacitive sensors , Sensors and Actuators, A 46-47, pp. 113-120, 1995.

Runyan, W. R., K.E. Bean, Semiconductor Integrated Circuit Processing Technology , Reading, MA: Addison-Wesley, 1990.

Saaski, E. W., J. C. Hartl, G. L. Mitchell, R. A. Wolthuis, and M. A. Afromowitz, Multimode Fiber Optic Pressure Sensor with Extended Range, presented at Fiber Optic and Laser Sensors V, San Diego, CA, and published in proceedings of SPIE, vol. 838, pp. 46-48, 1987.

Sundin, K. et al, Fabry-Perot cavity sensor system with compensation for fiber attenuation and sensor temperature variation , accepted for presentation at North. Opt. 2000, Uppsala, Sweden, 2000.

Sze, S.M., Physics of Semiconductor Devices, 2nd Edition, pp. 851, John Wiley & Sons, New York, 1981.

Sze, S.M., Physics of Semiconductor Devices, 2nd Edition, pp. 15-16, John Wiley & Sons, New York, 1981.

Tanaka, K., E Takata, K Ohwada, Anodic bonding of lead zirconate titanate ceramics to silicon with intermediate glass layer , Sensors and Actuators A - Physical 69: 2 Instrumentation & Measurement, 29, pp199-203, August 1998.

Tatic, S. et al, Bonding quality characterization of silicon-glass anodic bonding , Sensors & Actuators, pp.223-227, 1997.

Velluet, M. T., P. H. Graindorge, and H. J. Arditty, Fiber Optic Pressure Sensor Using White Light Interferometry, presented at Fiber Optic and Laser Sensors V, San Diego, CA, and published in proceedings of SPIE, vol. 838, pp. 78-83, 1987.

Yariv, A., "Quantum Electronics", Wiley, New York, 4th ed., 1998.

Wallis, G., D. Poerrantz, Field assisted glass-metal sealing , J. Appl. Phys., 40(10), pp. 3946,1969.

Xiao, Zhi-Xiong, Silicon--glass wafer bonding with silicon hydrophilic fusion bonding technology , Sensors and Actuators A: Physical, ISSN: 0924-4247 Vol./Iss. : 72 / 1, pp. 46-48, 1999.